August 2020

Spectroscopy versus turbidity: non-invasive in vivo monitoring of living systems

Seth Fillioe
Syracuse University

Abstract

The overall aim is to advance the use of light for noninvasive monitoring of living systems generally defined**.** We first describe work used to test a methodology for real-time probing of chemical and physical changes in spinal cords in the immediate aftermath of a localized contusive injury by way of calculating pH to monitor physiological changes in the system. Utilizing a previously developed unique algorithm, line scans of injured cords as well as optical profilimetry and scanning NIR autofluorescence images were obtained simultaneously in vivo, on exposed rat spinal cords. For line scans, the laser spatially scanned across the cord or, to collect Raman spectra, held at a specified location relative to the injury. Line scans reveal photobleaching effects and surface and shallow subsurface profiles, possibly locating cord vasculature. Analysis of the in vivo Raman spectra reveals phosphate features allowing calculation of cerebrospinal fluid pH. We developed additional technology to allow *in vivo* measurement of cell culture viability as e.g. glucose uptake rate, in real time. Proof of principal was demonstrated by physically sampling medium of viable cultures over time. That success motivated an attempt to repeat the measurement on the medium inside the culture flask *without* physical sampling. The final part of my research focused on observing the effects of x-ray irradiation on bone. Differences between control bones, irradiated bones, and the contra-lateral limb of the irradiated bones were assessed using depolarization ratios and other Raman spectral markers to assess internal effects of the radiation on protein and fat metabolism in bone.

Spectroscopy versus turbidity: non-invasive *in vivo* monitoring of living systems

By:
Seth Fillioe

B.A Hofstra University 2012
M.S Syracuse University 2017
M.PHIL Syracuse University 2017

Dissertation
Submitted in partial fulfillment of the requirements for the degree of
Doctor of Philosophy in Chemistry

Syracuse University
August 2020

Acknowledgments: First and foremost, thank you to Dr. Chaiken for taking me into his lab and giving me the opportunity to work with him. Dr. Chaiken has an amazing advisor and has greatly aided in making me a better scientist, a more confident, skilled researcher, and a stronger writer. His guidance in both our work as well as my career has helped to prepare me for a strong scientific career going forward.

I am also thankful for the guidance and assistance of the entire Chaiken lab, both past and present. Most specifically I would like to thank Dr. Paul Dent. Dr. Dent oriented me to the Chaiken lab and was not only there during his time in lab to assist me with any and all issues but continues to this day to be a great source of support and help if I need to reach out to him.

I am very thankful for the assistance and knowledge as well as the collaboration that Dr. Charles Peterson has given to me during my time here. Chuck is never more than a phone call away and his extensive knowledge of all things scientific have greatly aided us in the experimental process.

Thank you also to Dr. Jerry Goodisman who greatly aided us in processing a multitude of PCA calculations and other computer simulations. Dr. Goodisman's expertise in complex calculations and simulations greatly sped up the process of collecting and analyzing data and helped to give us a much more complete data set for a lot of our research.

I would like to thank Dr. Julie Hasenwinkel and her lab for their collaboration on all of our spinal cord studies. Most specifically I would like to thank Kyle Bishop who was my primary contact in the Hasenwinkel lab and performed the necessary surgical procedures involved in data collection of spinal cord data. Kyle also was an important part of discussion of how to present the spinal cord data.

Katherine Bakeev and Jun Zhao of BWTek were also imperative to finishing some of the work we did in this thesis. They provided a Raman device as well as the knowledge of said device to aid in finishing off a chapter and possibly extending a future relationship in the industry.

Work in this thesis would not be possible with the help of the Hougland lab, specifically Dr. Hougland and Michelle Sieburg, for providing us with mammalian cell cultures as well as the proper environment to conduct our experiments and also with knowledge of the cultures that aided in explaining the data collected in our mammalian cell chapter.

Collaboration with the Damron group at Upstate medical university is also greatly appreciated. With the teamwork of Megan Oest and Christopher Bartlow we were able to acquire a sample set of mouse bones and collect a large data set that was crucial to developing the bone chapter of this thesis.

I also need to extend a large thank you to the collective staff and resources of the Syracuse University Chemistry department. Firstly, my committee who has been with along this journey and has given very helpful feedback with all of my work. But also to the administrative workers in the department who are always there to answer questions and help in any way possible.

Syracuse University has also provided me the opportunity to meet an amazing group of friends who have helped in this process as well. Whether it be up late studying for exams together, stressing over orals, or celebrating each other's great achievements, I could not have asked to meet and have a truly great group of friends that I will have forever going forward.

Lastly, I would like to thank my personal support system. This group of people have been my rock for my time working on this thesis. This list starts with my family. My mother

and father, Anne Fillioe and Gary Fillioe have supported me every step of my career and their love has helped me get to where I am today. My sisters, Dr. Sarah Fillioe and Maggie Adams as well as my brother in law Brian Adams have also stood by and supported me and I cannot thank them enough for their love and support.

Most important of all though I must thank my beautiful wife Caitlin Fillioe. Caitlin has seen me during my easiest and most successful of times and at my worst of times and has never left my side since we met four years ago. She has been the strongest rock and support system I could ask for while working to achieve this degree and I cannot begin to thank her enough for all the love and support she has offered to me.

Table of Contents:

List of Illustrated Figures:

List of Tables:

1. Introduction

1.1 Motivation for Research

The main goal of this research is to extend existing spectroscopic methods to create clinical assessment tools for living subjects. To do this we first note that most living matter is turbid by nature. This causes difficulty in interpreting spectroscopic measurements quantitatively as the turbidity is the result of scattering and any collected signal i.e. remitted light may have endured multiple scattering events, having traveled an unknown path with an unknowable length.

Turbidity is the cloudiness or haziness of a sample that is visible to the naked eye. Caused by the presence of individual particles and/or other index of refraction boundaries inside the sample, "scattering centers" vary in size and composition. Indeed, some scattering centers settle in bulk liquids because they have greater density. There are also scattering centers that float in aqueous solution. Still others are associated with structures e.g. organelles like nuclei and mitochondria.[1]

Chemical analysis of turbid samples without the need for sample preparation such as pre-filtration, centrifugation and/or physical sampling has always been desirable but problematic.[2] Several groups, some prior to the Chaiken lab, have approached the spectroscopic problems caused by turbidity[3-6]. They found ways to calculate the effect of turbidity on certain spectral properties, e.g. spectral distortion of remitted emission where the emission can be either Raman or fluorescence based. At this point, the state of our capabilities depends on what kind of information one seeks.

The Chaiken group first approached this problem as it pertained to noninvasive in vivo blood and tissue analysis[7]. The goal was to monitor the intravascular space of the peripheral vasculature to quantify the relative volumes of formed components i.e. red blood cells (RBCs)

and liquid i.e. plasma or serum. This would allow use of spatiotemporal modulation of perfused tissue such that spectroscopic signals present in remitted emission could be quantitatively associated with a plasma volume to enable concentration calculations. They developed a method of noninvasive in vivo probing of tissue[8,9] i.e. “tissue modulation” using a single near infrared laser, intended to isolate signals associated with blood from those of the surrounding static tissues. In this context Chaiken created an algorithm (PV[O]H) that could partition the remitted light from a sample into two components, one reflecting turbidity and another on chemical composition. Once the algorithm[10] was developed the group began applying it to other types of turbid samples including in vitro samples. To distinguish from in vivo applications, they call it binary spectronephelometry (BSN) when applying it to in vitro samples. In 2014, the Chaiken group published work validating the algorithm generally, using a model in vitro system in which they could independently vary the turbidity and fluorescence yield of a sample.[11]

Almost all samples of interest to the Chaiken lab are turbid. When I began, the group had become interested in noninvasive characterization of cell cultures, the glucose uptake rates of certain cells, and the ability to measure this *in situ* but non-invasively using spectroscopy. Over the next four years, we tested a multitude of different biomedically important samples that had varying turbidity, from slightly turbid mammalian cell cultures to mouse bone, a dense and very turbid substance.

Eventually, our work characterizing spinal cord injury (SCI) suggested a very different use for the then well-developed algorithm. Because the SCI model we employ is highly localized, the idea of using a series of PV[O]H measurements at a grid of locations at and around the SCI would allow comparison of the most badly injured tissue with other less affected regions. That is, we realized that each of the measurement could be used as pixels to produce a two-dimensional

image. This image could be used like all images, but it would also reveal information concerning the physical and chemical states of affairs below the surface to some extent. We hypothesized that with repeated scanning we could utilize this algorithm not only for its original purpose i.e. to compare the turbidity and chemical composition of injured tissue to that of healthy control tissue, but potentially as a real time imaging modality for clinical assessment that would have fidelity with other imaging modalities that might be employed e.g. MRI. Although not in chronological order, below we list three separate sample types from among those we have surveyed, all of which are living. This thesis will focus on the non-contact, non-invasive spectroscopic characterization of these three sets of turbid samples.

1.2 Previous work on non-invasive studies

1.2.1 Spinal cord studies: Understanding inflammation and a possible new modality for mapping cords

In our first living system, we observe the chemical and physiological response of a spinal cord to trauma in the immediate term post injury. The Chaiken Group previously described the chemistry and the subsequent chemical and physical events of spinal cord injury (SCI) by studying ex vivo spinal cords in a rat model over a 4 day, 2 week and 8 week post injury timescale. This study spanned spatial and temporal scales associated with the chemical and biological domains that constitute SCI.

In that previous work Raman spectroscopy proved capable to discerning the accumulation of materials associated with the ultimate phase of the injury progression as confirmed by gold-standard immunohistological technique and subsequent work by our group and others. In addition, near infrared (NIR) probing to obtain Raman spectra also revealed enhanced fluorescence that was associated with the injury. Thus, we might imagine that *in vivo* probing of the time course of fluorescence might prove revealing to the progression of the injury. Moreover, my research

involves immediate phase to secondary phase timescale processes which have not been observed before. This is a much slower timescale than blood flow, i.e. seconds for blood to traverse a healthy cord, but much faster, being 30 minutes to 5 hours, than all previous non-contact, spectroscopic probing of spinal cords *in or ex vivo* i.e. days to weeks or longer.

Diagnosis and treatment of SCI will undoubtedly involve many existing tools and techniques.[12] The major issue with most if not all of these techniques is that the cord must be exposed, potentially placed in physical contact with a transducer, and physically/spatially stabilized in order to avoid motion defects. As for any technique *in vivo*, we have inevitable blood flow and respiration induced movement. We imagine that identifying structural tissue damage, and perfusion, or lack of perfusion, would be useful. And the other techniques do not contain chemical information that might identify the current status of the cord and hail the progression of subsequent events. A major difficulty in attempting to obtain chemical information spectroscopically in vivo stems from the turbidity of even healthy spinal cord tissue.

Analysis of the spectra collected in the immediate aftermath of SCI and in controls led to a definitive spectral assignment of strong phosphate Raman features[13] allowing calculation of pH. If this assignment is accurate, and the features are sufficiently strong, such pH calculations could reveal physiology occurring in CSF following an SCI. To our knowledge there has never been a non-contact *in vivo* measurement of pH taken from a spinal cord and observing pH variation could lead to a better understanding of SCI and the immediate processes following the injury.

Separately, in an attempt to deal with such turbidity, we can utilize the same algorithm designed and mentioned earlier and described in detail below.[9] It is important to note that this algorithm was designed with blood in mind and so it will be described in terms of "*apparent* vascular volume and *apparent* hematocrit". It allows quantifying changes in turbidity

as changes in *apparent* hematocrit (Hct) and manifestations of inflammation e.g. edema as changes in *apparent* total vascular volume. And this information can be obtained in parallel with obtaining Raman spectra which contain even more detailed information.

The algorithm itself is very simple and rests on assumptions that coincidentally are also met by the problem at hand i.e. probing spinal cords *in vivo*. Although the interpretation of the results of applying this algorithm need not be the same as if it were being applied to e.g. capillary blood in skin, it is extremely sensitive to 1) changes in perfusion or blood composition or 2) changes in elastic scattering or fluorescence yield *for any reason*. Our goal is to create a much more immediate analysis of SCI as noninvasively as possible. The tools the algorithm gives could be used to produce images based on inflammation, perfusion, Hct, fluorescence or Raman spectra thereby potentially providing a new noncontact capability not currently met by any other modality. We also show how the apparent Hct and VV reflect changes in surface topography systematically in order to produce interpretable images in terms of other modalities.

1.2.2 Cell viability current struggles

The next set of samples is a line of mammalian cells that are cultured in a polystyrene culture flask. The goal of this study being to monitor the viability of a certain culture at any given time. The term **"**Viability" refers to whether a tissue, organ or cell is alive or capable of living.[14] "Alive" and "dead" are considered to be an "all or nothing" approach to life whereas *viability* is distinguished from that by using an index to quantify certain "vital signs" i.e. measureable physiological or metabolic quantities that are constant at homeostasis of the cells of interest.[14]

For example, when unused cells are stored in cryopreservation, ice crystals that form on the cells can damage the extracellular structure and cause cell death.[15] The only existing test for

cell viability is “dye exclusion” in which a dye is added to an aliquot of culture and the percentage of cells capable of excluding the dye from their interior is a measure of the viability of the culture.[16]

We aim to develop quantitative indices that have direct metabolic meaning and that can be used in real-time without disruption of the cells’ activities. There are many advantages to having this capability e.g. the FDA has ruled that once collected into special dedicated containers, stem cells cannot be removed, nor materials introduced into/out of the bags or the entire culture must be discarded. Thus, our research is very important given the emerging central role of stem cells in medicine and the difficulty in obtaining them in sufficient quantities.[17,18]

There are many pros and cons that accompany the dye exclusion technique. Dye exclusion is a rapid measurement that can be made in high throughput to determine the number of dead cells in the culture. This is advantageous as it can help determine when processes such as apoptosis occur and that can aid in making decisions concerning culturing. The disadvantages, besides being invasive and consuming some of the cells themselves, also involve such things as being unable to discriminate between apoptosis and cell necrosis i.e. the cause of non-viability. Thus, in this context for example, the trypsinization of the adherent cells must be closely monitored in performing the dye exclusion test. Too much Trypsin can cause loss in viability and not enough can lead to less effective recovery of adherent cells.[19]

Another large issue involved in cell viability testing is the time taken to ensure the cells will grow when the culture is first created. Most cell cultures take roughly a week to go through the process of growth to determine that a previously frozen culture is still viable. This extra growth cycle and waste of resources can be costly and time consuming.[20] Clearly, if one could monitor e.g. glucose uptake from the outset one could save that time and all the resources needed.

1.2.3 Previous cell studies: Our new non-invasive approach

Some of this monitoring has already been done. Other studies in the Chaiken lab have looked at bacterial cultures non-invasively. Utilizing the same principles as the early *in vitro* experiments done to mimic turbidity[11], these cultures were created by varying both the amount of organism and the concentration of the medium. The Chaiken group was able to effectively "train" the system, which means to calibrate the remitted light to 1) the number of organisms present in a given culture and to 2) the chemical state of the culture medium as it changes in the course of a culture lifetime.

Once this information is attained, the same algorithm used in the turbidity experiment can be applied to the data to monitor both the growth rate of the bacteria as well as the nutrient depletion of the medium. This information can greatly advance our knowledge of the behavior of potentially dangerous bacteria and potentially find ways of monitoring its presence and eradicating it from places that could cause harm to humans. It also can be used to non-invasively probe large bioreactors, ridding the need to physically sample said reactors. What is even more important is that this can all be done without actively contacting said bacteria, making it safer to monitor.[21]

1.2.4 Bone studies and examination using depolarization ratios

The final set of samples studied is the composition and characteristic of bones that have been exposed to radiation for cancer treatments. A seemingly unavoidable side effect of radiation therapy for soft and hard tissue cancer patients, post-radiation induced bone fragility and fractures still remain a "significant public health issue that deserves attention".[22,23,24] Both in frequency and type, many fractures have been reported when radiotherapy has been used as treatment. Two of the more predominant injuries that occur are in the pelvis following radiation for anorectal and gynecologic malignancies, and rib fractures following radiotherapy for breast cancer.[22,25,26] These

injuries not only occur but also take longer, roughly six months or greater, than average fractures to heal.[27,28]

Early studies to investigate the reasoning for this medical mystery used full body irradiation and thus are less applicable to the current problem.[29,30] Newer but still limited studies were conducted using a more focused radiation field, but the study seems inconsistent and inconclusive with its aim to explain the weakened bones.[31] An independent clinical study showed that irradiation did not routinely decrease bone density and further suggested a material abnormality internally in irradiated bones.[32]

Raman spectroscopy offers clinicians and scientists a new tool for obtaining compositional information in bones such as carbonate or phosphate content, collagen content, the extent of collagen crosslinking[33-36] and other quantitative parameters relating to both composition and morphology, while spanning a range of spatial scales unavailable to other established imaging techniques. It is a hypothesis at this point that information about both the bone mineral (phosphates and carbonates) and matrix compositions (the proteins like collagen) as well as structural information e.g. degree of crystallinity aids in determining the quality and strength and integrity of the bone tissue.

The Morris Lab at the University of Michigan Ann Arbor, have investigated, using non-invasive spectroscopic techniques as assessment tools, the osteoradionecrosis of the jaw,[37,38] a potential preface to moving the technique to irradiated bones. The Morris Group, in a more recent paper[39] hypothesized that there are certain intrinsic factors and changes that include chemical composition and degree of molecular orientation, determined by the depolarization ratio, within bones that have had radiation treatments, that may contribute to the fragility in bone.[40] Time course

studies after irradiation have also been done to detect the effect of the biological response on the strength of bones by Raman spectroscopy.

Gong et. al[39] used Raman to probe the biological response of irradiated bones via time course dependent studies. They found that there was a significant increase in collagen cross-link ratio as well as a decrease in the depolarization ratio of matrix over the course of the 26-week study. Mineral depolarization ratios also decreased with two small exceptions over that time frame. The combination of many composition factors, mineral crystallinity, mineral/matrix ratio, collagen morphology, and carbonate/phosphate ratios were examined. Gong suggests that collagen, containing pathological cross-links that form after radiation damage, is poorly re-absorbed during an altered remodeling process. They hypothesize that this causes new bone generated post treatment to occur on a defected scaffold and that leads to increased brittleness. Our interest in these samples was to provide an insight into possible faster and more effective investigation of these bones.

1.3 Spectroscopy Background

Most photon scattering interactions with atoms or molecules are *elastic*, i.e. a photon has the same energy before and after the scattering interaction, but a different direction. In soft biological materials elastic scattering is preferentially in the forward direction. This is called "Rayleigh" or "Mie" or simply elastic scattering, depending on whether the scattering object is smaller or larger than the wavelength of light respectively. **"**Raman" or in-elastic scattering occurs when an incident photon interacts with a molecule such that energy is transferred to/from the chemical bonds within the molecule, leaving the scattered photon with less/more energy. *Fluorescence* is light that is emitted because initially an incident photon was *absorbed* by a molecule, raising it an excited electronic state. A wavelength-shifted photon is subsequently

emitted when the molecule returns to the electronic ground state and the propagation direction of the fluorescent photon is generally different from that of the incident photon.

For practical purposes we can summarize by saying that light incident on matter produces scattered photons of either the same wavelength that was sent in i.e. elastic emission (EE), or shifted to a different i.e. usually longer wavelength, the inelastic emission (IE), as shown in Figure 1.1.[41] The Raman signal can be seen *on top* of the fluorescence within the IE and baseline subtraction is needed to "isolate" the Raman features. The baseline correction procedures used in biomedical spectroscopy are arbitrary, vaguely based on the general characteristics of EE and IE but inadequate to actually separate the overlapping fluorescence and Raman features. Both the IE and EE are affected by the spectroscopy of different physical and chemical species present in the volume probed by the incident light.

Nevertheless, applied consistently across a data set obtained from a related series of samples, the baseline subtraction has the effect of increasing the apparent dynamic range of the detection system without affecting the raw signal to noise at any given wavelength (pixel). The actual signal to noise ratio at a specified wavelength i.e. wavelength shift *in the shot noise limit*, is simply calculated from the number of raw counts in the non-baseline corrected data. This is the relevant signal to noise for the comparisons across the homologous series e.g. variation of the chemical composition and physical state.

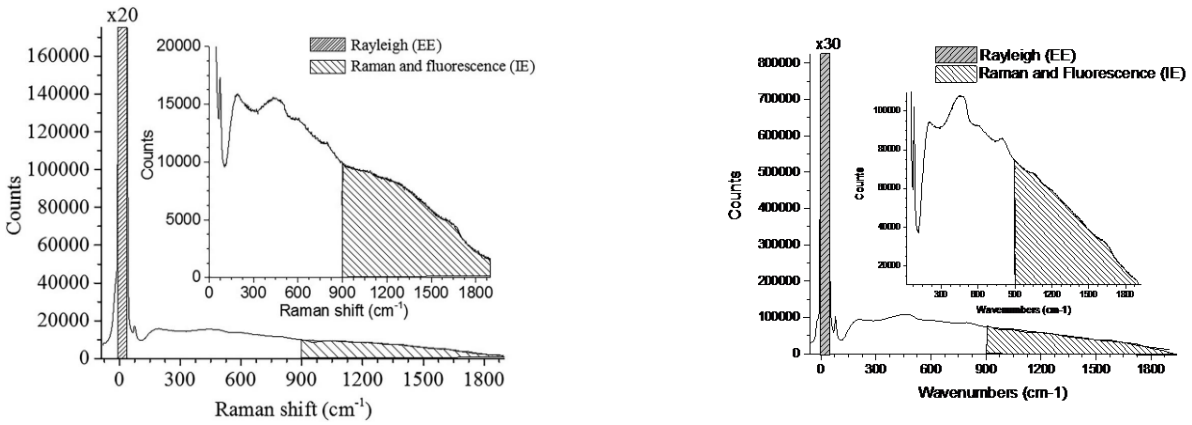

Figure 1.1. Intensity vs. frequency from a 200 msec frame of Andor (CCD) for a quartz sphere suspension in aqueous porphyrin (left)[11] and a native culture suspended in Lysogeny Broth (right)[21]. The Rayleigh line i.e. 0 cm^{-1} Raman shift contains the elastic emissions and the fluorescence and Raman are roughly 900 cm^{-1} to 1900 cm^{-1} contains the inelastic emission.

1.4 The PV[O]H and BSN Algorithm

By their nature biological media i.e. tissue or cells generally defined contain both fluids and formed components. The formed components may be soft or hard, but they always produce more elastic scattering (EE) of incident light than clear liquids or other *homogeneous* condensed media. By contrast, production of light that is wavelength shifted from incident probing light by a range of possible inelastic processes (IE) is roughly equally associated with both the fluid and formed volumes. Note that under constant laser probing both the fluids and formed components may initially remit fluorescence but either can be bleached so that less or no fluorescence is eventually produced after a period of continuous probing. This “photobleaching” behavior is an essential aspect of laser probing biological media and we will return to it later.

Presently we note that although we present PV[O]H in the context of capillary blood in perfused skin, the algorithm pertains to many systems that have fluid and formed components that can be grouped together and thought of as two separate phases. For example, in the context of a probed volume within perfused skin, the volume fractions for red blood cells (RBCs), plasma and

"static tissue", which we take for everything else in the skin, sum to unity implying that there are no voids. Another such instance, explained below the RBC/plasma example, is in bacterial culture.

When applied to in vitro systems, the algorithm can be applied differently and is referred to as Binary Spectronephelometry (BSN). The principle of a two-phase system is the same, the components of said phases just change. Back to the RBC/plasma example, the idea of a finger being composed of three parts (RBC, plasma, static tissue) is summarized in equations 1 and 2 using ϕ for each of the volume fractions, i.e. RBCs, plasma and static tissue in the probed volume. Equation 2 refers to the fact that when/if these volume fractions change either due to internal homeostatic physiology or external factors e.g. normal cardiac function, applied pressure or temperature induced vasodilation/constriction, they do so in manner that does not produce voids in the tissues. In a spinal cord, injured or not, we might associate plasma with cerebrospinal fluid or actual plasma and RBCs if the probed volume contains vasculature and actual blood.

$$1 = \phi_r + \phi_p + \phi_s \qquad (1)$$

$$0 = d\phi_r + d\phi_p + d\phi_s \qquad (2)$$

As a general model we used the Radiation Transfer Equation (RTE) to propagate the incident light from air into a three phase, three-layer medium in the single scattering limit and with the phases, i.e. the RBCs, plasma and static tissue distributed homogeneously in the probed volume[11]. We implicitly assume that RBCs and plasma inside the cord volume have the same optical properties as those freely circulating elsewhere. This same approach can be taken for the bacteria, as expressed in previous work[21] where instead of ϕ_r, ϕ_p, and ϕ_s we simply use a two phase approach of ϕ_{LB} and ϕ_{NC} .

Since in skin we were able to obtain agreement with experiment and RTT by summing contributions to IE and EE *linearly*. The scattering coefficients for skin are within a factor of 2 for those of cord tissue, and still at least one order of magnitude less than that for RBCs, so we are in the single scattering limit and we can still write two independent linear equations:

$$\mathrm{EE} = \vartheta_1 + \vartheta_2\phi_p + \vartheta_3\phi_r \qquad (3)$$

$$\mathrm{IE} = \vartheta_4 + \vartheta_5\phi_p + \vartheta_6\phi_r \qquad (4)$$

From the definition of hematocrit (Hct) we have equation 5.

$$\mathrm{Hct} = \phi_r/(\phi_r+\phi_p) \qquad (5)$$

The 6 parameters in (3) and (4) can be determined using the RTE and published scattering and absorption coefficients but presently our interest is better served by noting that since we have 2 linearly independent equations linking 2 measured quantities, EE and IE, to the 2 volume fractions, ϕ_r and ϕ_p, for each simultaneous measurement of EE and IE, it is possible to invert equations (3) and (4) to obtain (6) and (7). The same approach can be taken for calculation of ϕ_{LB} and ϕ_{NC} however these latter two equations shown below (6 and 7) reflect the clinical significance of monitoring *changes* in vital signs to diagnose and treat. This is a slightly different formulation of the algorithm from what we used for bacterial cultures and quartz spheres. It also has the effect of increasing the dynamic range of PV[O]H based images. The use of EE_0 and IE_0 are not included in the BSN algorithm.

$$\phi_r = \mathrm{a} + \mathrm{b}\left(\frac{\mathrm{EE}}{\mathrm{EE}_0}\right) + \mathrm{c}\left(\frac{\mathrm{IE}}{\mathrm{IE}_0}\right) \qquad (6)$$

$$\phi_p = \mathrm{d} + \mathrm{e}\left(\frac{\mathrm{EE}}{\mathrm{EE}_0}\right) + \mathrm{f}\left(\frac{\mathrm{IE}}{\mathrm{IE}_0}\right) \qquad (7)$$

There are 6 parameters (a, b, c, d, e and f) for which we must obtain numerical values. This can be done using constraints based on empirical data or assumptions. EE_0 and IE_0 are values obtained at the start of probing and all subsequent variation of EE and IE are calculated with respect to these values. Thus, the apparent values of "ϕ_r" and "ϕ_p" so obtained are with respect to some arbitrary choice of starting values. In the present case, based on how the device was calibrated, the starting reference point is Hct=28.65 and all figures and graphs presented herein will reflect that choice. Since we are interested in *changes* in the cords over time or with respect to a location in the case of imaging, this choice is arbitrary at this point.

The experimental apparatus we used for this work was previously calibrated for use on capillary blood in skin using dialysis induced blood composition changes independently monitored using an FDA approved gold standard device called the CritLine[10]. The CritLine analyzes blood inside the dialysis machine to obtain a value for Hct that can be extended to give ϕ_r and ϕ_p.[10]

1.5 Systems studied, and Hypotheses investigated

1. Mapping Spinal Cord Injury: This study will introduce the idea of using PV[O]H as a tool for performing optical profilometry of cords, monitoring spectroscopic and thereby chemical changes following injury, and suggest what that can tell us about spinal cord physiology and about injuries.
2. Spinal Cord Injury inflammation in the immediate stage: To complement previous long time point *ex vivo* examination of cords we will be looking at immediate (30 mins-roughly 5 hours) time points of a cord *in vivo*, still intact in a living rat. It will also use new calculations and assignment of peaks to observe pH changes and differences as a way of explaining physiological response.

3. Mammalian cell cultures: We aim to measure metabolic activity, nutrient consumption and production of waste, non-invasively. This multi-step approach will first include medium studies and conclude with a study of a culture, through the sides of a closed culture flask.
4. Irradiated vs. control bone composition and physiology: We explore the biomedical spectroscopy of more turbid samples by investigating the physiological response of bones after radiation while also looking at their contra-lateral counterparts to see any of the same behavior.

Chapter 2: *In vivo*, noncontact, real-time, PV[O]H imaging of the immediate local physiological response to spinal cord injury in a rat model

Published: ***J. Biomed. Opt. 25(3) 032007 (2019) doi: 10.1117/1.JBO.25.3.032007***

Seth Fillioe[1], Kyle Kelly Bishop[2], Alexander Vincent Struck Jannini[2], John Jong In Kim[2], Ricky McDonough[1], Steve Ortiz[1], Jerry Goodisman[1], Julie Hasenwinkel[2], Charles M. Peterson[1], J. Chaiken[1]

[1]Department of Chemistry, Syracuse University, Syracuse New York, 13244; [2]Syracuse Biomaterials Institute, Department of Chemical and Biomedical Engineering, Syracuse University, Syracuse New York, 13244

Abstract

We report a small exploratory study of a new methodology for real-time imaging of chemical and physical changes in spinal cords in the immediate aftermath of a localized contusive injury. 100 separate experiments involving scanning NIR images, 1-dimensional, 2-dimensional and point measurements, obtained in vivo, within a 3 x 7 mm field, on spinal cords surgically exposed between T9 and T10 revealed differences between injured and healthy cords. The collected raw data i.e. elastic and inelastic emission from the laser probed tissues, combined via the PV[O]H algorithm, allow construction of 5 images over the first 5 hours post injury. Within the larger study, a total of 13 rats were studied using 2-dimensional images i.e. Injured and Control. A single 830 nm laser (100 μm diameter round spot) was spatially line-scanned across the cord to reveal photobleaching effects and surface profiles possibly locating a near surface longitudinal artery/vein. In separate experiments the laser was scanned in 2 dimensions across the exposed cord surface relative to the injury in a specific pattern to avoid uneven photobleaching of the imaged tissue. The 2-dimensional scanning produced elastic and inelastic emission that allowed construction of PV[O]H images that had good fidelity with the visually observed surfaces and separate line scans and suggested differences between the volume fractions of fluid and turbidity of injured and healthy cord tissue.

2.1 Introduction

On every level, the costs of spinal cord injury (SCI) are staggering.[42] We devote tens of billions of dollars each year in addressing the societal costs, and that is small compared to human suffering on the individual level. In this paper we very briefly present a new algorithm i.e. the PV[O]H algorithm, our procedures for collecting in vivo data from rats, and the results of an exploratory study to introduce PV[O]H as an imaging modality for rat spinal cord. We performed line scans to explore this possibility and observe the effect of the probing light on the tissue. Finally, we will present spinal cord images constructed from 2-dimensional scanning of an 830 nm laser across the region of interest. At each position in the scan the PV[O]H algorithm is applied to remitted collected light, calculating 1) the apparent volume fraction of the probed tissue filled by fluid and/or fluorescent materials and 2) the apparent turbidity of that fluid.

The depth of the probed volume is roughly 300 microns when the tissue is fingertip skin with a 3-5% volume fraction of blood perfusion and the blood has a hematocrit (Hct) of roughly 15. The depth is greater than that for spinal cord probing with 830 nm light. Raman spectra show that we sample at least some space containing cerebrospinal fluid (CSF) but we cannot be sure how deeply we penetrate the actual neural tissues i.e. cord below the arachnoid space. Because of elastic scattering light propagation is less when red blood cells (RBCs) and protein are present in the fluid. We suggest the tissue depth sampled is greater for spinal cord probing than for perfused fingertip skin because 1) healthy CSF has nearly no protein in sharp contrast to plasma and 2) the perfused neural tissue i.e. grey matter is anatomically deeper than the less perfused white matter.

Although only a small study, we are encouraged that successive images of the same region can be obtained with our current methodology and that improvements are certainly possible. Whether or not the cord is injured, such images may vary systematically immediately after an injury. This study suggests that PV[O]H may be a valuable new imaging modality for diagnosing and treating SCI. In this Introduction, we first present relevant issues within the specific context of SCI and then we introduce the current technology for SCI imaging and the goals we would like to address with PV[O]H imaging that are not met by other modalities.

2.1.1 Spinal Cord Injury

Although there are different kinds of spinal cord injuries, in a generic sense, all spinal cord injuries begin with an unintentional physical event that disrupts cell membranes and tissue structures and causes materials that are foreign in uninjured tissue to contact and mix with healthy tissue and fluids.[43] Immediate cell death of neurons, glial cells, and endothelial cells, occurs due to the mechanical trauma locally, defining the site of injury. This research investigates the chemical and physical state of injured spinal cord beginning within the 1st half hour of injury and extending to the subsequent 5 hours. During this primary or immediate phase of SCI a cascade of chemical and biological processes within the region of the injury is initiated and regardless of the injury, the situation increases in complexity.

The secondary phase involves movement/migration of materials/cells in and out of the injured region and can last for hours to days. Note that the spatial distribution of the materials/cells during this phase may reflect the spatial distribution of the initial unintentional physical event and change over time. Observing the chemistry of injured cord tissue at the very beginning of the cascade might provide the best opportunity to contrast injured tissue with healthy tissue because heathy CSF is relatively low in protein relative to plasma. Protein

produces significant background elastic and inelastically scattered light that may obscure scattering from SCI associated materials/cells. Thus one main motivation for this research was to determine what spectroscopic information may be accessible during the immediate or primary phase. Any chance of success diagnosing and possibly treating SCI without physical contact depends on our capacity to detect and characterize chemical processes in turbid and delicate materials.

In addition to blood flow, which also distributes materials to/from the injured region from/to other parts of the body, our choice of timescale is comparable to that of the passive transport of molecules in the fluid media i.e. cerebrospinal fluid (CSF) that fill the interstitial spaces within a healthy spinal cord. We hope that observing and possibly enumerating and identifying primary processes might suggest tactics and strategies to arrest a sequence that if left unattended will eventually form a glial scar. Alleviating scarring in turn could permit attempts at rehabilitating an injured spinal cord and promote healthier outcomes. Being able to predict that a glial scar will or will not form given the condition of a contused cord would itself be very useful in helping to decide, as soon as possible after SCI, whether desperate measures can or should be taken that entail no greater risk to the patient than doing nothing.

2.1.2 Imaging and SCI

If the initial effects of the injury reduce blood flow into and out of the injured region, the resulting hypoxia will cause additional damage to the affected tissues.[44] PV[O]H[45] is simultaneously sensitive to 1) the presence/absence of blood and 2) the oxygenation state of the hemoglobin and so would seem to be advantageous. Other techniques will almost certainly be applicable to addressing related issues such as blood flow e.g. Doppler based optical techniques or optical coherence techniques (OCT).[46] Flow based measurements have been made in other

parts of the body e.g. femoral artery in the context of SCI but not in the cord itself. We address some of the practicalities of trying to apply optical techniques directly to the cord in the immediate aftermath of injury. Note that the possible utility of Low Level Laser therapy (LLLT), also known as photobiomodulation (PBM) at the earliest times might also be coupled with and benefit from this exploratory study.[47]

Previously[43] we described the chemistry and the subsequent chemical and physical events of SCI by studying ex vivo spinal cords in a rat model over a 4 day, 2 week, and 8 week post injury timescale. Near infrared (NIR) probing revealed enhanced fluorescence that was associated with the injury. Thus we might hypothesize that in vivo excitation of fluorescence during laser scanning might reveal the progression of the injury because PV[O]H has a well-defined response when fluorescence increases and decreases.

We suspect that diagnosis and treatment of SCI will probably involve many existing tools and techniques.[12] Magnetic resonance imaging (MRI), computerized tomography (CT) and X-rays are noncontact imaging modalities that give a 3 dimensional, relatively high resolution view of the injured tissue without the need to surgically expose the cord, but none of these provide chemical information. Very high-resolution ultrasound (VHRUS) also produces clear images in vivo that are particularly rich in information regarding blood, but the cord must be exposed, in physical contact with a transducer, and physically/spatially stabilized in order to avoid motion defects. As for any technique in vivo, we have the inevitable blood flow and respiration induced movement, and while it still provides valuable information concerning structural tissue damage, and perfusion, or lack of perfusion, VHRUS does not contain chemical information. Even more invasive techniques in use today for research[48] that may someday form the basis for an approach for treatment might benefit from real time measures of physiological chemical signaling i.e. real

time fluorescence changes. A major difficulty in attempting to obtain chemical information spectroscopically in vivo stems from the turbidity of even healthy spinal cord tissue.

In attempting to perform noninvasive in vivo spectroscopic probing for blood and tissues analysis[9] in skin we needed to deal with the turbidity of biological materials in general. To this end, we developed "PV[O]H" to quantify intravascular blood volume and composition changes. To obtain such information one needs to deal simultaneously with both the spectroscopy and the propagation of light in the system i.e. the turbidity. To date we have validated PV[O]H in human and rat model studies involving skin, bacterial cultures in various media, and in unambiguous inanimate model systems.[10,11,21] The meaning/nature of the quantities calculated using PV[O]H depend critically on context. When applied to skin which has a capillary vascularization, PV[O]H calculates changes in the hematocrit (Hct) and total vascular volume of the capillary network.

It is essential to emphasize that in the context of imaging spinal cords with PV[O]H we are not suggesting that we are measuring blood when we calculate "apparent Hct". We shall label the spinal cord images produced using values calculated by PV[O]H with the word "turbidity" which is to be understood to be caused by the movement/migration of materials/cells in and out of the CSF in/near the injured region. The cells can be e.g. T-cells or other lymphocytes and the materials can be e.g. proteins such as immunoglobulins and other large molecules that scatter light elastically appreciably or perhaps fluorescence. Other types of molecules/materials i.e. cellular debris would have the same effect so more information may be required to identify these cells/materials. To this end we note that NIR probing can be done simultaneously to implement PV[O]H while obtaining Raman spectra.

The algorithm itself is very simple and rests on assumptions that are met by the problem at hand i.e. probing spinal cords in vivo. But the interpretation of the results of applying this algorithm is not as if it were being applied to capillary blood in skin. PV[O]H is extremely sensitive to 1) changes in elastic scattering and/or 2) changes in fluorescence/Raman yield for any reason in any tissues. Chemical information can often be inferred from fluorescence measurements utilizing endogenous or exogenous fluorophores.[49,50] PV[O]H can be used to produce images based on perfusion, Hct, fluorescence or Raman spectra thereby potentially providing a new noncontact imaging modality not currently met by any other modality.

2.1.3 The PV[O]H Algorithm

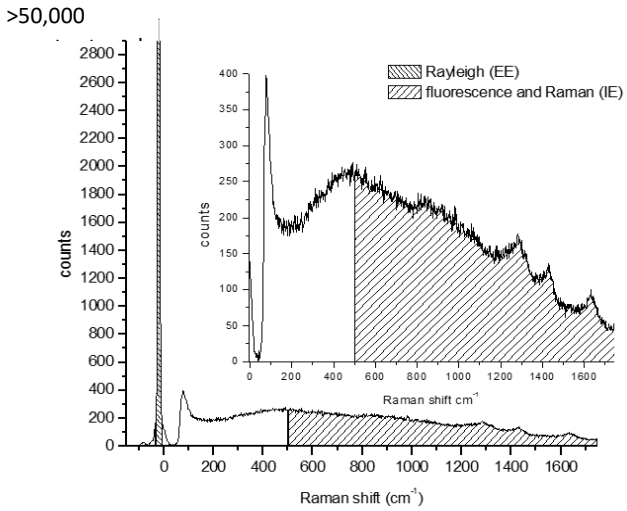

Figure 2.1. inset: raw typical single 20 msec frame of CCD output using 200 mW of 830 nm excitation on a human fingertip, bottom: same frame showing sections of emission integrated to estimate inelastic emission (IE, ≈ 500-1750 cm-1) and elastic emission (EE, -30 - +10 cm-1).

Probing nearly any biological material with NIR laser light produces a remitted spectrum roughly as shown in Figure 2.1. All the light that is collected caused by probing with incident near infrared (NIR) light has been either elastically scattered (EE) or is remitted with a wavelength shift and so we call it inelastically scattered (IE). IE contains both Raman scattered light, phosphorescence and fluorescence and we use both together as shown in Figure 2.1. EE and IE are

produced by two fundamentally different processes and so equations that describe their observation are independent.

The volume fractions for red blood cells (RBCs), plasma and "static tissue", which we take for everything else in the cord, sum to unity implying that there are no voids. This is summarized in equations 1 and 2 using ϕ for each of the volume fractions, i.e. RBCs, plasma and static tissue in the probed volume.

$$1 = \phi_r + \phi_p + \phi_s \qquad (1)$$

$$0 = d\phi_r + d\phi_p + d\phi_s \qquad (2)$$

We used the Radiation Transfer Equation (RTE)[12] to propagate the incident light from air into a three phase, three layer medium in the single scattering limit and with the phases, i.e. the RBCs, plasma and static tissue distributed homogeneously in the probed volume. We implicitly assume that RBCs and plasma inside the cord volume have the same optical properties as those freely circulating elsewhere. Since in skin we were able to obtain agreement with experiment by summing contributions to IE and EE *linearly,* and the scattering coefficients for skin are within a factor of 2 for those of cord tissue, and still at least one order of magnitude less than that for RBCs, we expect that we can write two independent equations:

$$\mathrm{EE} = \vartheta_1 + \vartheta_2\phi_p + \vartheta_3\phi_r \qquad (3)$$

$$\mathrm{IE} = \vartheta_4 + \vartheta_5\phi_p + \vartheta_6\phi_r \qquad (4)$$

From the definition of hematocrit (Hct) we have equation 5.

$$\mathrm{Hct} = \phi_r/(\phi_r + \phi_p) \qquad (5)$$

The 6 parameters in (3) and (4) can be determined using the RTE and published scattering and absorption coefficients. Presently our interest is better served by noting that since we have 2 linearly independent equations linking 2 measured quantities, EE and IE, to the 2 volume fractions, ϕ_r and ϕ_p, for each simultaneous measurement of EE and IE, it is possible to invert equations (3) and (4) to obtain (6) and (7).

$$\phi_r = a + b\left(\frac{EE}{EE_0}\right) + c\left(\frac{IE}{IE_0}\right) \quad (6)$$

$$\phi_p = d + e\left(\frac{EE}{EE_0}\right) + f\left(\frac{IE}{IE_0}\right) \quad (7)$$

There are 6 parameters (a, b, c, d, e and f) for which we must obtain numerical values. We can do this using constraints based on empirical data or assumptions. EE_0 and IE_0 are values obtained at the start of probing and all subsequent variation of EE and IE are with respect to these values. Thus, the apparent values of "ϕ_r" and "ϕ_p" so obtained are with respect to some arbitrary choice of starting values. In the present case, the device was calibrated is such a manner that the starting reference point is Hct=28.65 and all figures and graphs presented herein will reflect that choice. Since we are interested in *changes* in the cords over time, the choice of starting point in this methodology exploratory study is arbitrary at this point.

The experimental apparatus we used for this work was previously calibrated empirically by monitoring capillary blood in human fingertip skin in vivo using dialysis induced blood composition changes independently monitored by an FDA approved gold standard device called the CritLine. The CritLine analyzes blood inside the dialysis machine to obtain a value for Hct and thereby ϕ_r and ϕ_p.

2.2 Experimental

The Institutional Animal Care and Use Committee (IACUC) of Syracuse University approved our protocol in compliance with National Institute of Health (NIH) guidelines. We performed all surgical procedures in a sterilized surgical suite located in the Laboratory Animal Research (LAR) facility at Syracuse University. We purchased 13 female Sprague Dawley rats, at weight range 250g to 330g, from Charles River laboratories and housed in LAR at least two weeks prior to surgery to acclimate to their environment. Unless specified, we obtained all materials from Thermo Fisher.

We anesthetized animals using a procedure standardized in LAR for rat surgery with approval by a certified veterinarian. After placing the animal into a sealed chamber, 5% isoflurane (Shopmetvet, Mettawa, IL) is allowed to flow for 2 minutes until animal responses are minimal. After initial anesthetization, the animal is removed from the chamber and a nosecone is used to continually flow 2% or 2.5% isoflurane throughout the procedure depending on the weight of the animal. The surgical area is shaved and sterilized using alcohol and betadine soaked pads. A hot water therapy pump (Braintree Scientific, Braintree, MA) was used to regulate the temperature of the animal throughout the procedure and was placed at 37°C. The device was turned on prior to anesthetization to allow adequate time to reach temperature. We sterilized all surgical tools using a micro glass bead tabletop autoclave for 2 minutes per manufacturer instructions to ensure sterility before, during and for cleaning after surgery.

Location of T8, T9, T10 and T11 are verified through touch along the animal spine as both T8 and T11 spinal processes are more pronounced than surrounding vertebrata. A final check ensures deep anesthetization by tail pinch and blink reflex tests as detailed in IACUC requirements with additional tests performed to ensure continued anesthesia throughout the

procedure. An approximately 1-inch long incision using a #10 scalpel blade (Fine Science Tools, Foster City, CA) is made along the spinal column from T8 to T11. Using surgical scissors (Fine Science Tools, Foster City, CA), a hole is cut into the fat layer beneath the skin and blunt dissection is used to separate the muscle and fat layers; the fat layer is then cut and moved away from the surgical area. In parallel, incisions are made through each of the three muscle layers on either side of the spine. Once more, the position of the spinal processes is used to verify the location of T9 and T10 by moving the back of the scalpel along the vertebral column; incisions are made perpendicular to the spine between T8 and T9, T9 and T10, and finally T10 and T11.

At this point muscle is removed in a piecemeal method using both surgical shears and scalpel to expose bone. The dorsal layer of bone for T9 and T10 is removed to expose the spinal cord to a full length of at least 1 cm using Friedman-Pearson Rongeurs. (Fine Science Tools, Foster City, CA) The area was cleaned using a saline spray and sterile cotton balls prior to scanning. After completion of the experiment, all animals were humanely euthanized under anesthesia through an overdose of 0.5 ml pentobarbital (Sigma-Aldrich) by intraperitoneal injection. Verification of euthanasia was determined by cessation of respiratory functions and a blue tint to the skin. Subjects were then stored in a 20°C biohazard storage chest until offsite removal.

Directly after surgery, excess fluids in the region adjacent to the exposed spinal cord were absorbed/drawn into sterile tissue paper. We observed very light redness on the spinal cord that we attributed to irritation caused during removal of dorsal section of the vertebral column. We noted that over the succeeding 10-20 minutes, the redness faded in both controls and injury samples after initial Raman scans. During surgery, we observed no significant changes in spinal cord morphology due to Raman laser exposure or exposure to environmental conditions. A small

number of small body spasms occurred, resembling simple autonomic reactions due to the anesthesia that we considered inconsequential. Fluid buildup was sometimes apparent in both control and injury samples possibly from an unknown source, although at least some was pooled saline used to hydrate the tissue that we were unable to drain away. Direct tests showed that the fluid i.e. saline did not affect the Raman signals or show any signs of detrimental effects on the surrounding tissues.

The injury model for a rat and all techniques for creating a contusion injury were developed by Rutgers University's W.M. Keck Center for Collaborative Neuroscience division. The contusion injury for all injured animals was produced using the Multicenter Animal Spinal Cord Injury Study (MASCIS) Impactor model III using the standard 3mm size impaction tip at 12.5 mm above the spinal cord. Previous work with the impactor has demonstrated that the drop distance used for this study is capable of replicating a moderate injury that was believed to be sufficient for modeling a contusion injury for scanning purposes.[43]

We employed a modified commercial Raman spectrometer (Lambda Solutions, Waltham, MA) to perform all spectroscopic measurements. The optics and filtering were standard for Lambda Solutions probes with the addition of an additional Raman notch filter (Semrock, Rochester, NY) placed between the collimating lens and the grating to allow adjustment of the EE and IE for optimum dynamic range in the PV[O]H calculation. Unlike our previous published in vivo experiments on rats[10], which utilized paws, these experiments employed a standard Raman normal incidence probe having a focal length of 1 cm and an effective NA of ≈0.13 and the smallest spot size was ≈100 μm. The entire surgical field and in particular the point where light contacts the tissue was kept moist in order to prevent burning during extended exposures. The surface was contacted directly with 80 mW of CW light at 830 nm and the raw CCD data

(Critical Link, LLC, Syracuse, NY) comprised 20 msec frames sampled at 50 Hz. A black tarp placed over the animal, stage and impactor ensured as little exterior light as possible reached the Raman detector.

In order to scan across the spinal cord of the animal, a programmable x-y stage was developed in the Hasenwinkel lab shown in Figure 2.2. An Arduino microcontroller, using custom-built MATLAB script, was capable of controlling two separate stepper motors independently with steps as small as 10 microns. An additional immobile arm held the Raman laser probe stationery while allowing the animal to be moved beneath the laser probe. Two vertebral clamps were attached to the top of the stage minimized animal movement during scanning. Both the stage and the MASCIS impactor were on an immobile cart with black drapes placed on struts to prevent external light from contaminating the data.

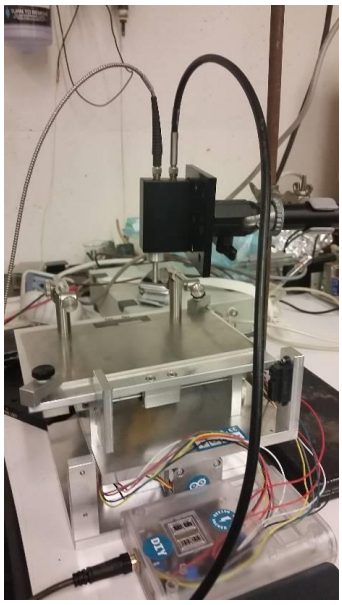

Figure 2.2. Diagram showing the X-Y stage with Raman laser above the animal clamps. The black box represents the Raman laser housing, with the silver cable supplying the laser and the black cable connecting to the detector.

To verify weight-drop location on the cord, the top of the stage was modified to include a rail that extended out underneath the MASCIS impactor. The laser probe was placed to minimize the diameter of the laser spot on the cord surface by visual inspection at the beginning of the experiment, before the animal is moved along the rails to underneath the weight drop. Three positions were chosen at this time along the spinal cord with reference to where the impact of the weight would occur. The first position on the cord, denoted as position A, was located towards the rostral end of the animal relative to position B, which was located at the position where injury would be induced i.e. on the center of the weight drop. Position C was located towards the caudal end of the animal relative to position B, the position of injury. In addition, both positions A and C were chosen 1-millimeter off center of the spinal cord to avoid potential overlap with underlying bone while also maintaining a roughly 1 mm distance away from the pre-determined position B. The animal was returned along the rail to the stage and secured once the positions were determined. We verified the laser spot size and location by observation before beginning each scanning process i.e. when placed at position A. Since the spot size is a function of the distance between cord surface and the laser probe aperture, this check insured that the animal height did not change through the experiment.

We performed >95 separate experiments with many of the early experiments intended to explore the phenomenology and technique of probing spinal cord tissue with laser light so that practical protocols could be developed for producing scanned images. In addition to heating and possible burning when dehydrated, all biological materials remit autofluorescence that bleaches i.e. decreases over time with continuous probing.[10,11] In order to produce meaningful images it is required that all tissues be probed with the same net fluence so that they are all equally bleached.

Based on these observations we designed protocols to reveal and ultimately minimize these effects on the images, both 2-dimensional and line scans.

To compare injured tissue to healthy tissue using line scanning, one must maintain equal scanning times for each of the three positions along the spinal cord depicted in Figure 2.3. Also, to avoid potential burning from prolonged exposure, a set maximum scan time of <25 minutes was determined for one complete linear scan and 37 minutes for a 2-dimensional scan. Within this total exposure timeframe, we initially placed the laser spot on position A, and collected EE and IE for 5 minutes. The stage would then move continuously for 5 additional minutes while we collect EE and IE along a straight line between positions A and B. Upon reaching position B the stage would stop while we collected EE and IE for 5 minutes. Afterwards, scanning followed a straight-line path from position B to C. At position C, 5 minutes of stationery data collection ended the line scan. Thus, data at A, B and C are the average of 15,000 CCD frames while 150 frames are averaged for each point in between corresponding to 3 seconds per point. This scanning process from A to B to C required 25 minutes to complete with the laser on continuously during the protocol. Afterwards we blocked the laser to avoid extra bleaching while the stage returned to the initial position. We monitored the animal to ensure adequate hydration of the injury site as respiration and anesthesia were maintained throughout the procedure. This procedure was completed a total of 10 times for all control animals and for two of the injury animals with one injury animal having to be removed early due to a lack of oxygen remaining in the supply for the anesthesia device.

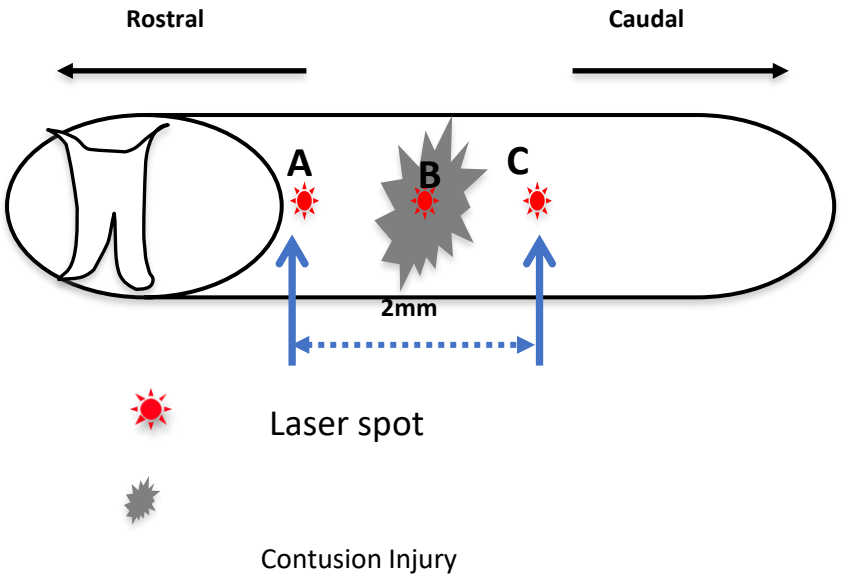

Figure 2.3. Schematic diagram depicting positioning of reference locations used to compare injured cord to healthy cord.

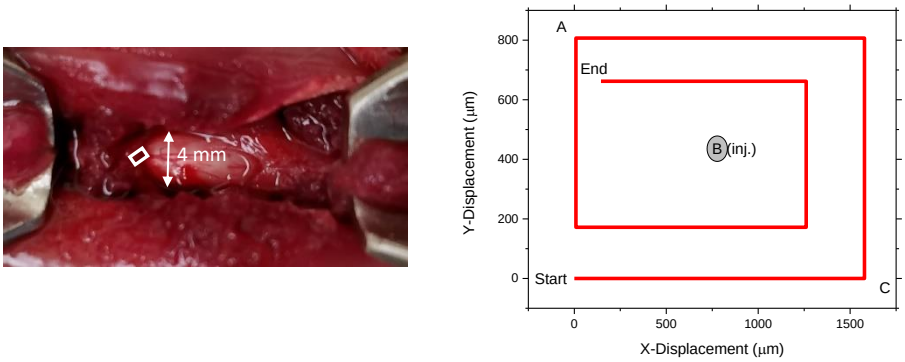

Figure 2.4. Left: Surgical field showing location of laser 2-dimensional scanning i.e. white box. Right: Mapping of Raman probe scanning pattern to collect data that produced the 2-dimensional PV[O]H images of the spinal cord. Reference positions A, B and C defined in Figure 2.3 with respect to line scanning are shown in the white box and the photograph.

Two-dimensional scanning required special care to avoid fluorescence bleaching induced by the probing laser from defining the nature of the image. Once a scan was started the animal was translated continuously as EE and IE were collected so the laser time a one location was minimized. Each data point i.e. pixel was the average of 1800 20 msec CCD frames corresponding to a spatial resolution of ≈250 μm. Thus, we produced images based on the Hct values calculated at 64 points centered on different x, y locations and a scan required 37 minutes.

The scanning pattern ensured a small overlap of adjacent pixels in both directions. Because of the fluorescence bleaching, to obtain these points we designed the scanning pattern shown Figure 2.4 (right) that did not expose any one location on the cord surface to more than one probing per image. Images can be based on the EE, IE, plasma volume, RBC, or Hct and since the scanning can be repeated, time lapsed monitoring is possible. Using the same scanning pattern for successive images results in each of the 64 positions used to produce an image having endured the same total laser fluence. When based on the EE alone the images are essentially optical profilometry but when combined with the IE via PV[O]H, we have images based on 1) the spectroscopic properties of the materials within a depth of 300-500 μm of the cord surface and 2) the topography of the surface being scanned.

The origin of topographical contrast is the interplay of reflection and transmission at the scanned surface. Whether line scanned or 2 dimensionally scanned, PV[O]H images have fidelity with the physical appearance of the cord surface for the following reasons. When the probing light is initially brought into contact with a cord surface, a direction is defined as normal to the surface at that location. Then, when the animal is moved under the probing light to probe the surface at different positions e.g. as in Figure 2.4, the angle of incidence may change if the surface topography changes as depicted below in Figure 2.5.

As can be seen in the standard reflectance curve for light traversing a water air interface, also in Figure 2.5, the amount of light traversing the surface i.e. not being reflected, varies with angle of incidence. To generate IE the light must traverse the surface and when it does, IE is produced/detected along with EE and the apparent Hct calculated by PV[O]H manifests that transmission. This leads to contrast that reveals the surface topography. We note that the 2-

dimensional images all show a gradation of apparent Hct variation at the edges where visual inspection shows that all cord surfaces have a greater curvature near the edges.

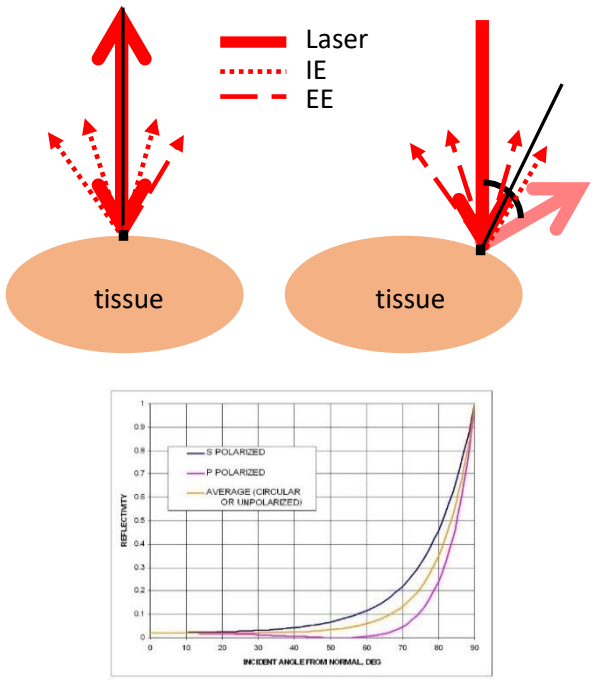

Figure 2.5. Top - schematic (transverse view) diagram of spinal cord and probing geometry showing variation of angle of incidence with surface topography. Bottom - Reflectance of smooth water at 20°C (refractive index 1.333).[51] Reflected light contributes to EE collected and light that transmits through the spinal cord dura produces both EE and IE as indicated. The mutual variation of the EE and IE between spatial locations leads to PV[O]H contrast in the image relating to surface topography.

2.3 Results

2.3.1 Line Scans

The variation of the raw EE and IE and the calculated associated "apparent" Hct using the PV[O]H algorithm as the laser is scanned back and forth across the same trajectory on a healthy spinal cord are shown in Figure 2.6-Left and Right. For Figure 2.6-Left we display the raw IE and EE i.e. contained in successive 20 msec frames, after having applied a 25 point adjacent average smoothing procedure.

We observe the average IE to decrease monotonically with some fluctuations either increasing or decreasing. In contrast, the EE is relatively constant on average but does fluctuate in a manner different from, but clearly correlated with, the IE fluctuations. This is analogous to observing the IE and EE at a single location but as a function of time, with fluctuations caused by e.g. variations in perfusion. Here we observe fluctuations due to variations in surface topography and composition of the cord is it is translated under the probe laser.

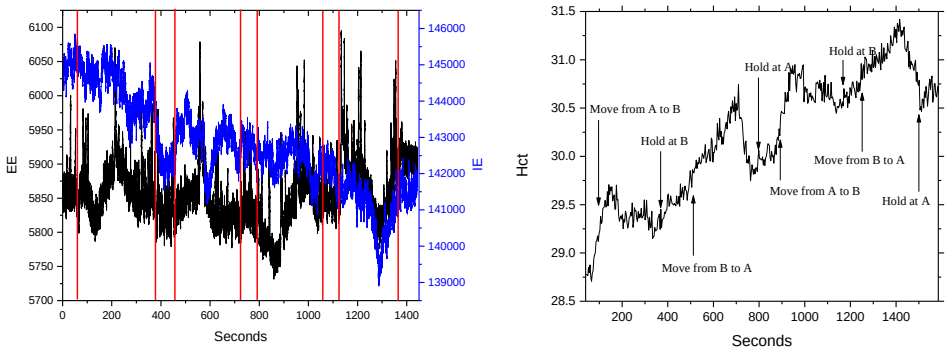

Figure 2.6. Left-The EE and IE obtained while scanning a cord for the purpose of showing how this imaging works. This scan did not follow the protocol described in the Experimental section. In this case the scan started at A with the rat motionless for 80 seconds, then scanned to B in 200 seconds, stayed at B for 80 seconds, scanned back to A in 200 seconds, stayed at A for 80 seconds, rescanned from A to B in 200 seconds, stayed at B for 80 seconds, rescanned back to A in 200 seconds, collected last 80 seconds at A. The laser probing was at the location indicated in the right image 1) at beginning and end of experiment and 2) between the red lines in Left Figure.

The bleaching can be inferred by the rise in "apparent Hct" at the hold locations.[10] By the end of the experiment, the bleaching at position A i.e. the amount of Hct increase while holding at A is much less than at the beginning of the experiment also while holding at A for the same time interval. This behavior is exactly what we observe in skin with the bleaching being complete at a single location in about 5-10 minutes of continuous probing at these power levels.[10] Once fully bleached, the tissue remains bleached for at least 5 hours in actual live tissue, without additional exposure to the laser.[49,50] This qualitative behavior of the probing/algorithm applied to spinal cord is essentially identical to that when applied to skin and

despite the fact that we calibrated the algorithm in use against capillary blood Hct variation in skin, the same set of parameters a-f for equation 5 produces acceptable variation for image formation.[10] That is, we do not expect the actual apparent Hct values to be meaningful, but the relative variation of "apparent" Hct as employed for imaging should be systematic, reproducible and in fidelity with the actual physical appearance of the cord.

For comparing injured vs. healthy spinal cords, we performed line scanning as described in the Experimental Section according to Figure 2.3. These line scans of apparent Hct over time allow a methodical recording of fluorescence changes, increases in apparent turbidity e.g. as might occur with bacterial infection of the CSF or the occurrence of excess protein in the CSF. The height of the surface of the animal changes less than the angle of incidence varies with the surface topography of the cord. Variation in distance between the laser aperture and the cord surface affects the spatial resolution of the image by changing the laser spot size. Visual observation suggests that in this study that variation is very small, probably less than 10% i.e. the spot diameter might vary by between about 100-110 μm diameter. Inflammation, edema possibly other effects could induce similar changes over the course of time.

At each Hold location, we observe the Hct to increase, regardless of location or whether the cord was injured or not, until the tissue is completely bleached. While in motion between locations, the Hct initially always decreases and then a variety of Hct responses are observed, including very sharp and deep dips such as near 1200 seconds in either the pre-injured or 1st post injury scans in Figure 2.7. The Hct tends to decrease in between the reference locations because the tissue along the scan route bleaches more slowly than the tissue that receives continuous probing i.e. the Hold locations.

The IE (total counts at Raman shift 1078 cm-1 including underlying fluorescence) collected for all 33 measurements were plotted semi-logarithmically in Figure 2.8. Despite the fact that the measurements combined results from 3 different hold locations i.e. A, B and C, the linearity of the result indicates that there is an exponential decay in IE during the data collection in the Hold at each location, while the EE does not change appreciably. This reinforces our inference that autofluorescence photobleaching occurs and indicates that the spatial registration of the scanning system is reproducible and precise to within plus or minus the diameter of the laser spot ≈100 μm.

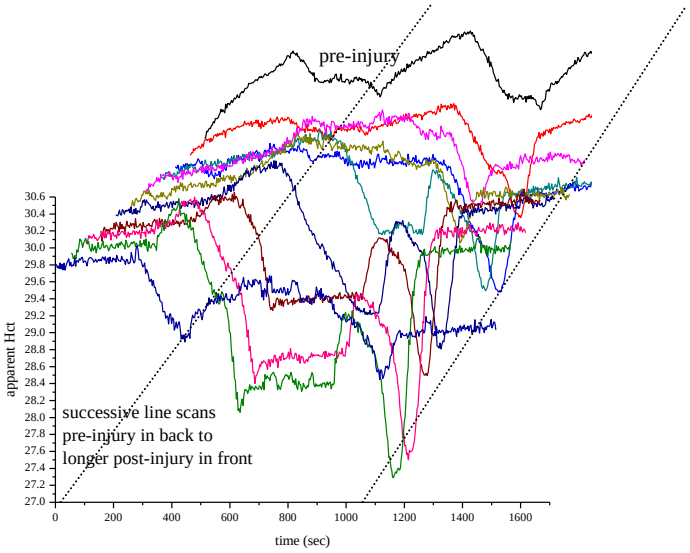

Figure 2.7. All 11 line scans from pre to post injury in a single SCI experiment. The time scale for scanning indicates the progression of the SCI, the bleaching process and the position of the scan. because of the simultaneous bleaching that is occurring. Note that this is an “injury” experiment and “control” experiments were performed in exactly the same manner, including total time intervals, except no impaction/injury was performed. The pre-injury scan is in the back with the successive scans in front. This is plotted so that the earliest scan is displayed translated slightly to the right and the later scans extend slightly to the left. Semi-log plots of IE for all scans at any particular Raman shift are essentially linear over the initial 5 hours post-SCI including the pre-injury scan.

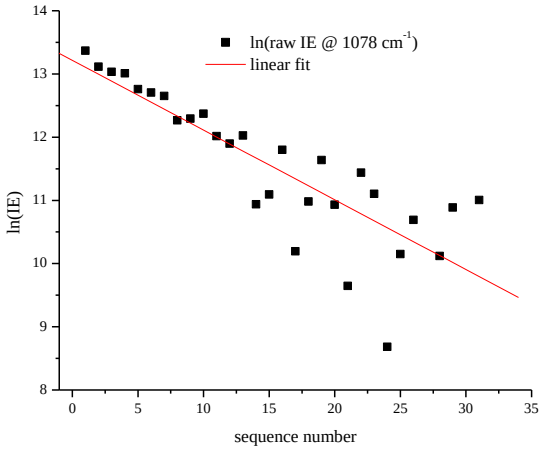

Figure 2.8. Semi-log plot of average IE for each of the 11 scans over the initial 5 hours post-SCI including the pre-injury scan.

The same data was collected over the progression of the SCI initiated event; all 11 scans for this particular experiment are shown in Figure 2.8. Note that as the number of successive scans increases the increase in Hct at each Hold position diminishes indicating that whatever material is being bleached, it is not replaced in the time interval between successive scans. Thus, while there is almost certainly some emission from blood i.e. from both RBCs and plasma, the bleached material is not blood since as long as the heart is beating, the blood is totally and continuously replaced in seconds from the probed volume.

The precipitous dip near 1200 seconds is unusual in that an equally precipitous rise quickly follows. The strong localization of the apparent Hct variation forces us to consider the possibility that we scanned over the blood vessel that can be seen in Figure 2.4-Left. We observed this type of structure in the PV[O]H line-scan image repeatedly, suggesting that PV[O]H images might have good fidelity with the actual appearance of the cord in each case. While we observe that the conditions for straightforward application of PV[O]H are usually met, as a localized event, scanning over a superficial vessel with relatively large vascular volume and Hct might not meet the requirements. Compared to other tissues, this probing would provide a

unique mutual variation in EE and IE that is inconsistent with the PV[O]H assumptions for applicability i.e. Equations 1 and 2 are obeyed and elastic scatterer density beyond the single scattering/linear propagation range.[9] This could result in an uncharacteristic calculated value for turbidity/apparent Hct at those locations. Related to that consideration, we should also be cognizant that direct laser irradiation of blood in the intravascular space could result in excessive localized heating and ultimately, tissue damage.

Figure 2.9 shows the “average turbidity" line scans calculated by PV[O]H as a function of position(time) averaged over three separate injured rats and 3 separate control i.e. uninjured rats and averaged over all scans in an experiment i.e. sequence number. The sharper quality of the “dips” observed for the Control animals as compared with the broader dips observed for the Injured animals may result from registration errors in the scanning procedure. All animals were initially scanned before injury regardless of whether the animal was ultimately part of the Injured or Control cohort. The process of inducing injury did not involve additional movement to use the impactor specifically to avoid the opportunity for spatial registration error. So despite the small number of animals in each cohort, it is also possible that the difference in the average images results from cardiovascular changes induced by the injury itself.

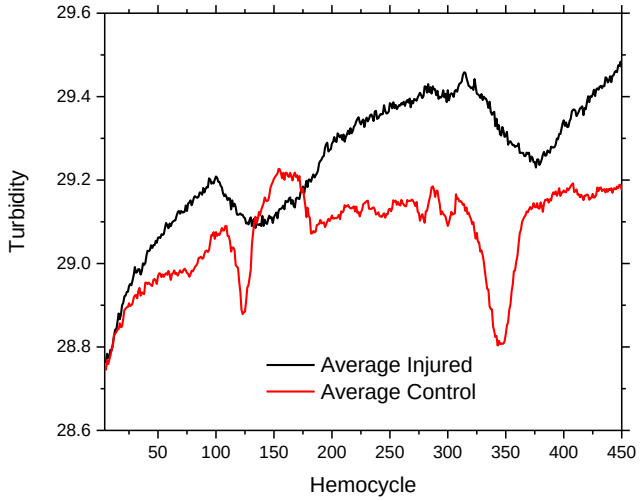

Figure 2.9. Line scans for averaged over 3 Injured and 3 Control animals. "Turbidity" is apparent Hct calculated from EE and IE using PV[O]H calibration. The Injured animal scans display more bleaching effects while the Control animals displayed more narrow and well defined "dips". Note: 1 Hemocycle corresponds to 3 seconds.

2.3.2 Two-Dimensional Imaging

In order to explore the feasibility and possibly justify the conducting a larger study, we performed a series of 2-dimensional imaging experiments using one Control and one Injury model rat. The orientation and position of the surgical field and exposed spinal cord are shown in Figure 2.10 along with an actual 2-dimensional image. The orientation of all line scans e.g. in Figure 2.7 are shown in the black line and dots. The appearance in the images with rising and falling apparent Hct are independent of the position of scanning a specific location in the whole scan indicate that the choice of scan direction and total laser exposure per scan avoids photobleaching artifacts.

Successive images are shown in Figure 2.11 for an Injured and a Control rat. There are notable differences, but a definitive comparison must await additional data to possibly show statistical significance. Presently we observe that the images of the probed regions of both animals may reflect the effect of injury. A larger apparent Hct usually involves increases IE and decreased EE. A topographical origin of such an observation could occur if there is greater

curvature in the Injured cord than in the Control cord. Note that if incident probing i.e. laser light was maintained at a location of high apparent Hct for too long, bleaching would be observed if such was the case. As another possible cause, if there was swelling in the Injured cord this would be observed.

Simulations based on the optical properties of cord tissue might reveal quantitatively how much change in apparent Hct could be associated with either effect. At this point we cannot be settle this question but we are encouraged that the images may in fact be classified based on the difference between internal physical and chemical status and topographical variation. It seems quite likely at this point that with more experience such difference could then be interpreted in terms of inflammation, edema and/or swelling as one group of possibilities and bacterial infection or protein increase in the CSF as another. We note in passing that Raman spectra can be obtained at any location simultaneously with obtaining EE and IE and that would provide additional information to help classify and differentiate the possible causes and effects manifested in these images.

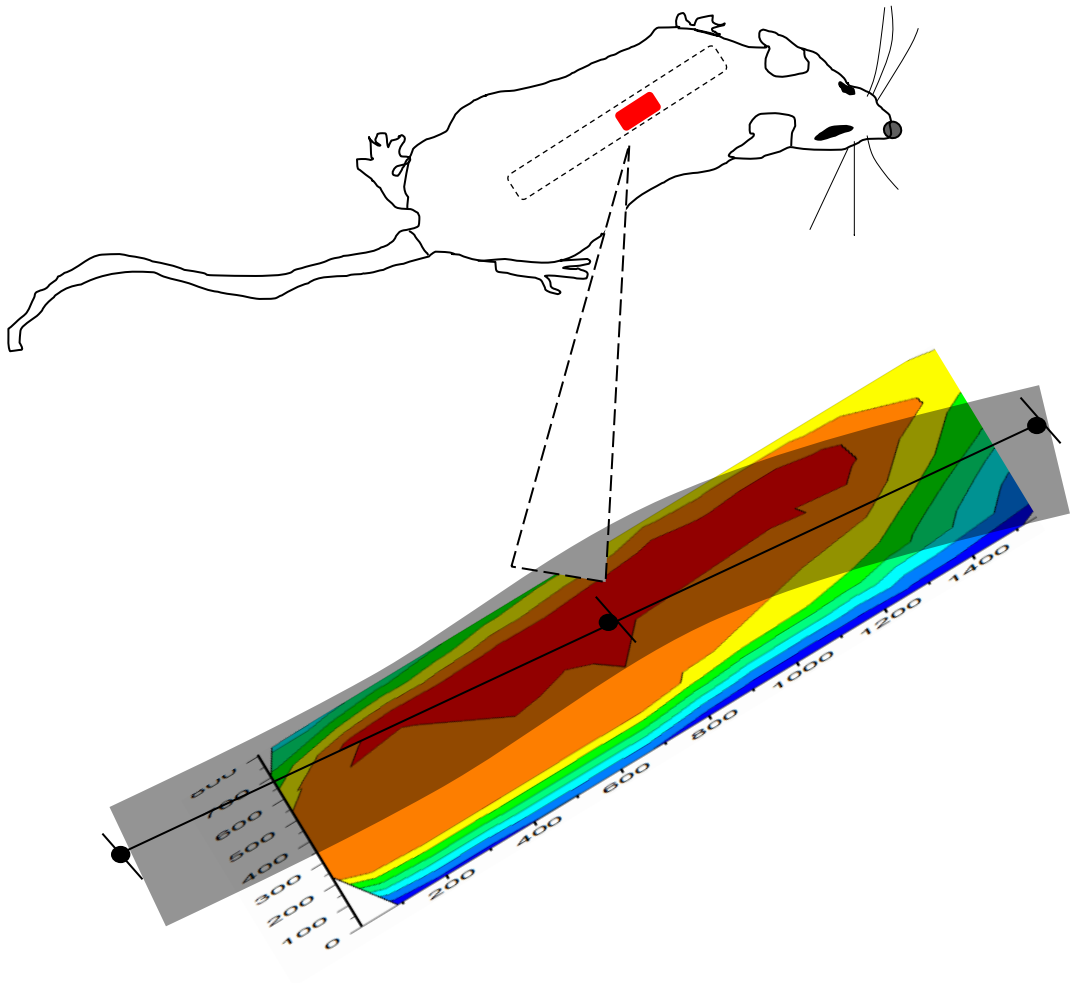

Figure 2.10. Image of surgical field including spinal cord based on Hct values obtained in a scan trajectory (Figure 2.4 right) designed so that no point is probed twice so as to avoid photobleaching effects from an early test scan causing systematic artifacts in later images. Note the systematic fall off of the apparent Hct on the edges of the image due at least in part because of topographic variation i.e. curvature. The spatial scale is indicated on both axes using the time from the beginning of the first scan in seconds since the actual distances are as shown in Figure 2.4 Left and Right and the possibility of photobleaching artifacts is determined by the time duration of the laser exposure.

We note that the pre-injury images of the two animals are essentially identical. And regardless of the above ambiguity, the successive images suggest that injury initiates processes that evolve over a period of >2 hours from the time of injury. The images for the Control animal are essentially constant over the entire experiment arguing that hydration is adequate and that the spatial scanning is also executed consistently.

Analogous to the line scans Figure 2.12 shows the average 2-dimensional image from the sequence shown in Figure 2.11 as well as the standard deviation of each pixel. The standard deviation of a pixel in the center of the images is smaller by about a factor of 3 than the difference of the apparent Hct between Control and Injury in the same location.

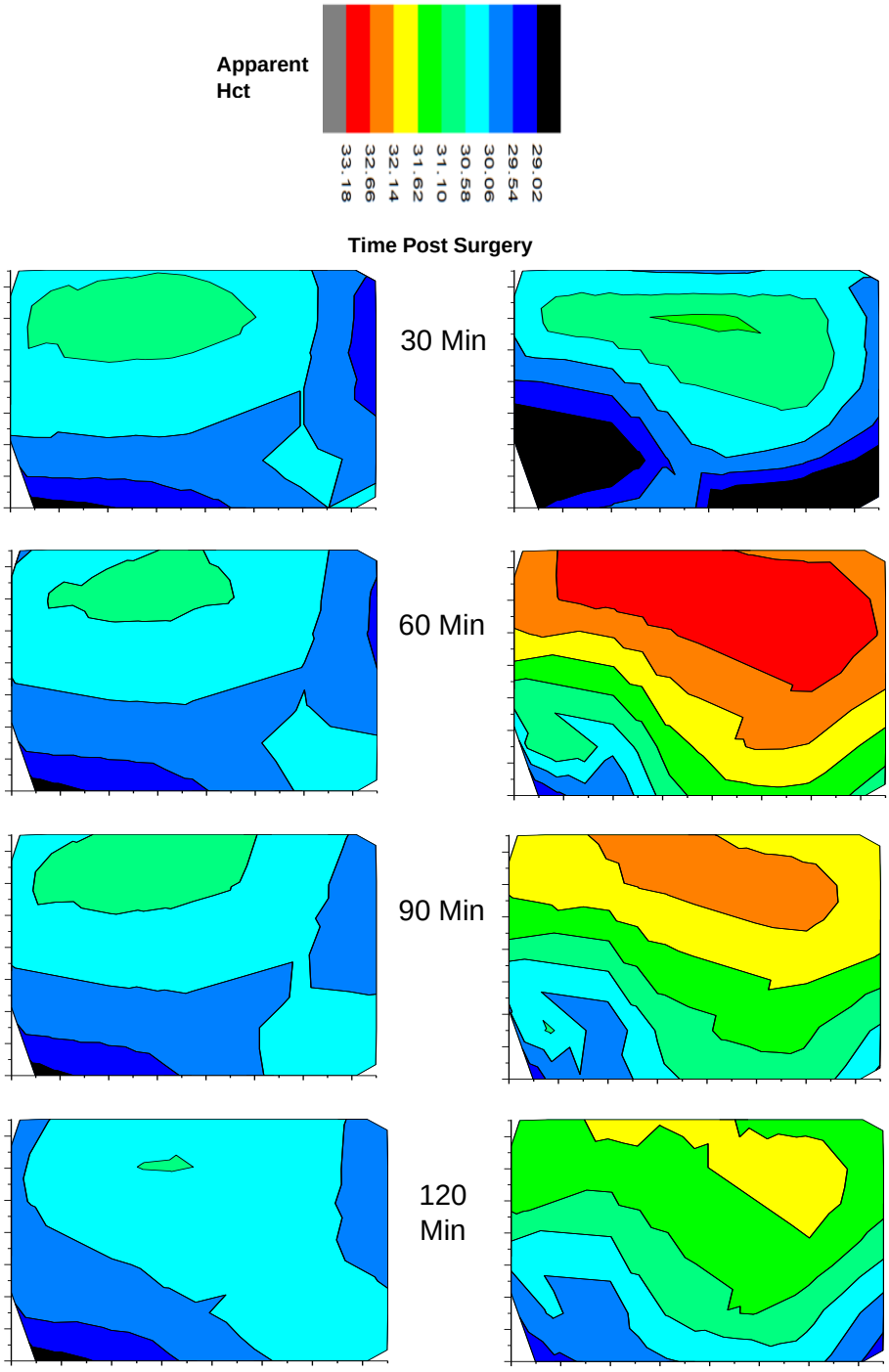

Figure 2.11. Successive images of an injured cord (right) and an uninjured cord (left) at various times after surgery to exposed cord. The apparent Hct scale is the same for each image and the orientation and size of each image is as indicated in Figure 2.10. Note that injury is not induced until after the first 30 minutes scan.

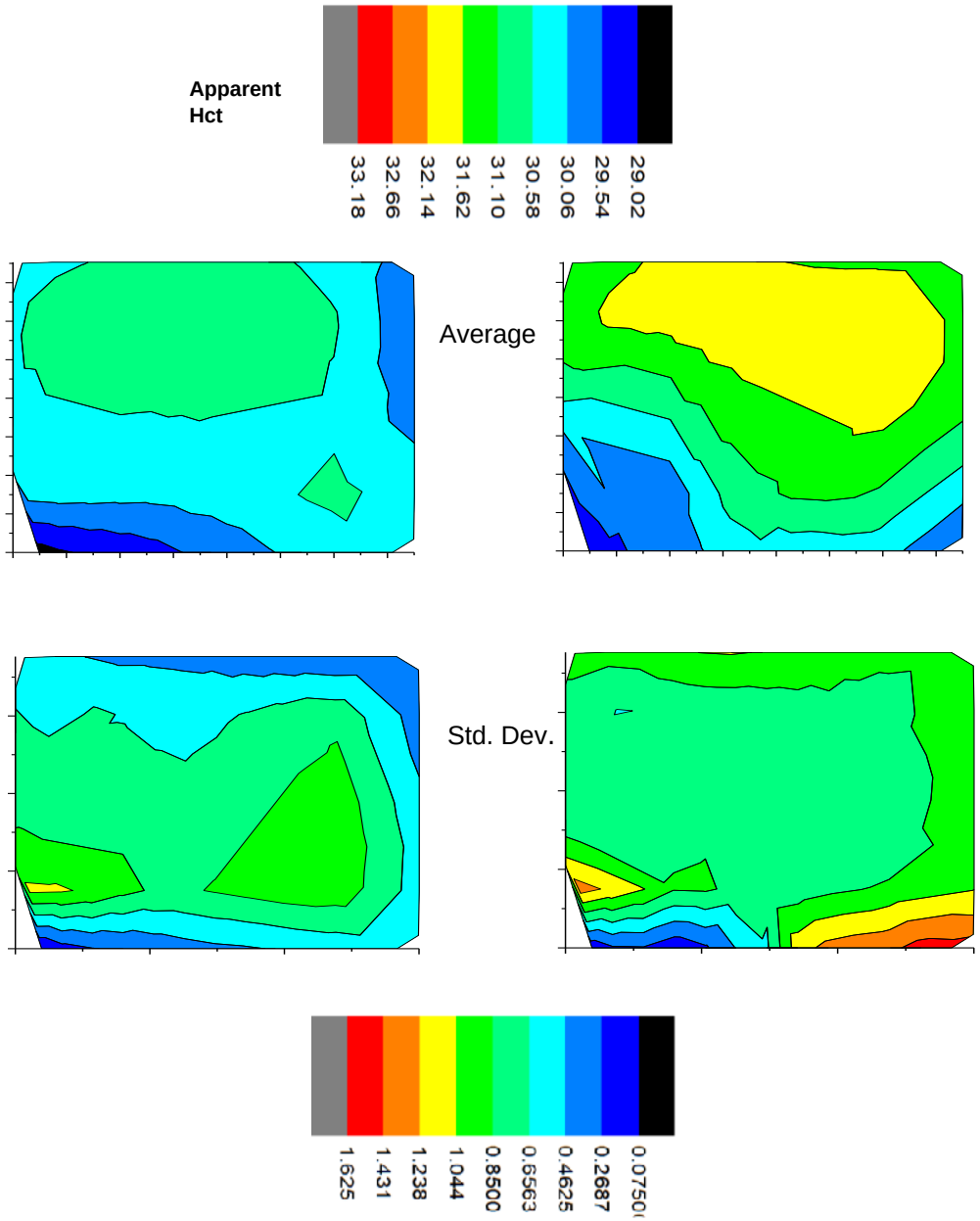

Figure 2.12. (top) Average of spinal cord images from Figure 2.11 above of both injured (right) and uninjured cord (left) over scanning time. (bottom) Standard deviation of spinal cord images of both injured (right) and uninjured cord (left) over scanning time.

We find the 2-dimensional images to be remarkably consistent with the line scans. The average pre-injury line scans start at a higher turbidity than the first 2-dimensional image regardless of whether the rats are Control or Injured group. However, this is to be expected since care was taken throughout the 2-dimensional scanning process to limit the exposure of the tissue

to laser induced bleaching. On the other hand, the line scans started at point A with a full 5 minutes exposure to laser probing, which caused photobleaching and the expected increase in measured turbidity. Furthermore, we note that the average 2-dimensional images in Figure 2.12 clearly show slightly greater apparent Hct i.e. turbidity for the Injured animal over the Control animal averaged over all locations and timeframe. We also note that later 2-dimensional images show turbidity increases near the edges at the later times, possibly because there was some drying out of the tissues. Uneven drying might also make the standard deviations of the calculated turbidity larger at longer times.

2.4 Discussion

Once accessed surgically, NIR probing of spinal cord in vivo is very much like probing other tissues. Given the profound insult required to surgically access the spinal cord, we were encouraged that surface blood and debris in the surgical field could be washed away significantly well to allow probing of the spinal cord itself. Experience shows that very little blood or any other absorbing chromophore is required to initiate burning which was not observed in any of the experiments and results presented in this study.

As expected, the decay of the raw IE with increasing laser exposure to any one spot indicates that there is photobleaching of the cord. The behavior and timescale for the autofluorescence coming to equilibrium with the probing laser is similar to fingers i.e. several minutes exposure at the power levels and spot size reported herein nearly completely bleaches a location. Also, pooled water or saline on the probed surface does not seem to alter the apparent Hct values. Since water does not fluoresce or have an appreciable Raman spectrum this is not surprising. The internal consistency of multiple scanning experiments show that it is easily possible to maintain spatial registration to at least ±100 μm during multi-hour experiments while maintaining hydration.

The line scans themselves suggest that such scanning produces images can be interpretable in terms of increasing/decreasing fluorescence, changing angle of incidence (surface topography) or combinations thereof. Assessing the behavior of autofluorescence or emission from exogenous fluorophores in the presence of turbidity, in a sensitive and reproducible manner, in response to procedures involving SCI or cords in general, is certainly a possibility using the PV[O]H algorithm. The actual capacity to assess such changes using PV[O]H images might be much better than we know from this study because in this study the calibration for the algorithm was based on capillaries in skin. Nevertheless, it produced variation in apparent Hct i.e. turbidity that produced an image with good fidelity with the observed physical image. This suggesting that the basic spectroscopic and transport assumptions/requirements for the PV[O]H algorithm are met by spinal cord as well as by skin. We also wonder if a different calibration of PV[O]H specifically for SCI would produce even better performance.

Although much more data is needed, the actual results obtained in this study suggest that in the immediate aftermath of contusive injury, the most immediate consequence is an increase whatever causes increased apparent Hct. The first region i.e. the subarachnoid space encountered by probing photons after penetrating the dura contains fluid i.e. CSF and there are many possible interpretations of increased turbidity. Blood could actually leak into that space from damaged fine vessels or perhaps, some other fluorescent or more highly elastic scattering material leaks into the same space.

We will not settle this issue in this study, but it seems probable that we could make progress using PV[O]H in a larger study. In our one paired observation involving 2-dimensional imaging, the increased apparent Hct dissipated over the succeeding 3 hours after injury whereas the control animal was constant to ±1% over the same period. This corresponds to the movement of materials from the 100 μm diameter initial point of impact to about 1 mm in all directions over the succeeding 3 hours. The observation demonstrates that it is possible to conduct the surgery to access the spinal cord in a manner that does not itself cause significant local physiological effect.

The issues of fluorescence and turbidity are particularly salient because as mentioned in the Introduction, SCI and independent spinal cord infection could manifest by protein, viruses or bacteria in the CSF. In this case the turbidity and/or fluorescence yield of the CSF would change and this could be expected to affect the PV[O]H images. Given that CSF normally contains very little protein, PV[O]H might be ideal for differentiating bacterial infection from physical injury effects of spinal cords in vivo. To this point, future work might address the question of whether the spinal cord could be accessed for optical probing by placing a fiber optic inside a hypodermic needle that could be used to bring the probe next to but not touching the cord, as in an epidural anesthesia procedure. This seems like a viable approach at this time because the point data from line scans was in agreement with the 2-dimensional images.

The abrupt dips observed in line scans were probably associated with near surface blood vessels. This hypothesis is supported by the orientation of the dips relative to the scanning, their reproducibility and comparison of the PV[O]H images with visual inspection. Since biomedical imaging can be very helpful if not essential to guide surgery or other interventions, being able to locate vessels and other points of reference is encouraging. Being able to locate such vessels also

presents the possibility of testing the relative effect(s) of Low Level Laser therapy (LLLT), or photobiomodulation (PBM) involving direct probing of the vessels or the surrounding tissues.[47] Finally, there are variations on the PV[O]H algorithm e.g. involving simultaneous Raman spectra as the IE, to produce images that could relate blood presence, fluid presence, localized inflammation or hypoxic conditions.[45] We will present Raman spectroscopic results from this study separately but presently we believe that unique internal chemical/physical analysis from spectroscopic/physical probing can be obtained without contact. We suggest that such imaging can be integrated with information or images from other devices e.g. robotic surgical suites to guide treatment.

2.5 Conclusions

PV[O]H images of exposed spinal cord in vivo obtained during the immediate locale/aftermath of moderate contusive injury reveal apparent changes in turbidity and/or fluorescence in the CSF that are different from Control. These differences dissipate in the succeeding 3 hours. We have employed the PV[O]H algorithm to 1) create 1 and 2 dimensional images, 2) locate near surface blood vessels and 3) show that spinal cord tissue photobleaches in a manner similar to skin.

2.6 Acknowledgements

This paper is based on a work originally published as a Proceedings SPIE paper: Seth Fillioe, Kyle Kelly Bishop, Alexander Vincent Struck Jannini, Jon Kim, Ricky McDonough, Steve Ortiz, Jerry Goodisman, Julie Hasenwinkel, J. Chaiken, "In vivo, noncontact, real-time, optical and spectroscopic assessment of the immediate local physiological response to spinal cord injury in a rat model," Proc. SPIE 10489, Optical Biopsy XVI: Toward Real- Time Spectroscopic Imaging and Diagnosis, 104890B (19 February 2018); doi: 10.1117/12.2290500

The PV[O]H device was engineered and fabricated by Critical Link LLC of Syracuse New York with Dave Rice, John Fayos and Jeff Bebernes being particularly involved. Funding from Syracuse University is gratefully acknowledged as is the able assistance of Sai Han Tun.

2.7 Financial Disclosure

Joseph Chaiken is the inventor for the relevant intellectual property and so has a financial interest in this research. No other author has a financial interest.

Chapter 3: *In vivo*, noncontact, real-time, optical and spectroscopic assessment of the immediate local physiological response to spinal cord injury: A chemist's view on the inflammatory response

3.1 Introduction

3.1.1 Spinal Cord Injury

On every level, the costs of spinal cord injury (SCI) are staggering.[42] Billions of dollars are spent yearly in addressing the societal costs, but that is small, yet not insignificant compared to human suffering on the individual level. Thus, there is great interest in better understanding a condition about which we can presently do little to affect the eventual outcome for the injured person in terms of functionality and subsequent quality of life. Although there are different kinds of spinal cord injuries, in a generic sense, all spinal cord injuries begin with an unintentional physical incident that disrupts cell membranes and causes foreign material in uninjured tissue to come in contact and mix with healthy tissue.[43] Immediate cell death of neurons, glial cells, and endothelial cells, occurs due to the mechanical trauma locally, at the site of injury. The first part of this research investigates both the chemical and physical state of injured spinal cord from within the 1st half hour of injury and extending to the subsequent 5 hours. During this *primary* or *immediate* phase of SCI a cascade of chemical and biological processes within the region of the injury is initiated and regardless of the injury, the situation increases in complexity.

The *secondary* phase (previously examined)[43] involves movement/migration of materials/cells in and out of the injured region and can last for hours to days. Thus, one main motivation for this research is the question of whether observing the chemistry of injured cord tissue at the very beginning of the cascade might provide an opportunity to contrast injured tissue with healthy tissue. In effect, is there a single or dominant immediate process, or do multiple

parallel processes occur, from the outset? Any chance of success in this endeavor depends on our capacity to detect and characterize chemical processes in turbid and delicate materials.

In addition to blood flow, which may help distribute materials to/from the injured region from/to other parts of the body, our choice of timescale (30-300 mins) is comparable to that of the passive diffusive transport of molecules in the relatively viscous but fluid media that fill some interstitial spaces within a healthy spinal cord. When healthy and at homeostasis, the bulk movement of cerebrospinal fluid (CSF) in the subarachnoid space and in contact with the choroid plexus 1) occurs on the same time scale as diffusive chemical transport 2) has a net turnover time well under the post injury observation period and 3) is from rostral to caudal i.e. brain to spinal cord and below. We hope that observing and possibly enumerating and identifying primary processes might suggest tactics and strategies that could be employed to slow or stop the eventual formation of a glial scar. In doing so, perhaps the problem of rehabilitating an injured spinal cord would be completely different.

3.1.2 Inflammation

Inflammation is a general term for a medical condition first described roughly two millennia ago. Roman physicians Celsus and later Galen provided a guide for medical personnel that defines inflammation in an empirical manner and remains essentially correct today. Redness, swelling, heat, pain, and loss of function are empirical criteria used for centuries to assess a situation and choose a course of action. Today we have instruments to more precisely and quantitatively characterize these qualities and that provide additional information to guide medical personnel in choosing and executing a course of action. We note that inflammation itself accompanies the entire injury, reaction and healing processes and that we expect that the more information we can obtain over the course of a specific instance of inflammation, the greater are

our opportunities to be able to understand and influence the overall process with the probability of concomitantly improved medical outcomes. For example, in the specific case of spinal cord injury (SCI), is it possible to avoid permanent loss of function and/or the formation of the glial scar?

Inflammation contains both biological and chemical components. From the point of view of a chemist, the biological response to spinal cord injury (SCI) begins by chemical signaling of different kinds of cells and the chemicals initially involved are those formed/released by the injury itself. Healing is a part of inflammation, beginning at some point during the subsequent cascade of biological and chemical processes, running in serial and in parallel to each other and ultimately transcending the nature of the chemicals and materials originating from the injury itself. Thus, we launched this study to explore the earliest chemistry following impactor induced contusive SCI.

In the case of mechanical insult, the physically weakest tissues that most effectively absorb the mechanical energy of the insult would be the most vulnerable. We do not know the mechanical strengths of the various relevant physical structures of the spinal cord nor their mechanical moduli and we have not characterized the energy impulse delivered by the impactor under our experimental conditions. We used an impactor[43] and probe tip with operational settings expected to produce a mechanical insult that induces moderate injury about 25% of the time. This would seem to be a reasonable choice given that we want to have enough instances of SCI to produce reasonable statistics while using the smallest cohort of animals. Our previous work[43] employed the same mechanical insult and microscopic examination of the tissues using validated immunohistological staining methods reinforced our conclusions based on the Raman spectra.

Given our ignorance at this stage, another goal is to explore the question of whether observing loss of function at the cellular/tissue level is possible using Raman spectra?

3.1.3 Imaging

Despite observing the early effects of spinal cord injury on the tissue mentioned above, more understanding is needed at the early timepoint after injury. Most currently available techniques to image spinal cord tissue and its changes over time do so on a macro scale and are unable to differentiate between chemical or cellular changes. Microglia are known to phenotypically change to resemble macrophages at some point post injury, however this same mechanism makes their function after injury ambiguous due to difficulty in discerning between the two different cell types.[52] The earliest imaging changes are seen using magnetic resonance imaging (MRI) and computer tomography (CT) scan, however both scans require invasive surgical procedure assess damage to the area.[53]

In the case of a contusion style injury, such as we intend to mimic, blood flow into the site is often restricted, severely limiting the efficacy of these imaging modalities.[54,55,56] In addition, while these methods can help visualize blood pooling in acute injuries, they cannot aid in visualizing the full area of injury. This cell response timeline post injury is becoming increasingly important to create clinical practices for treatment. Patients who undergo surgical repair after 24 hours post injury tend to show a greatly decreased rate of recovery compared to those receiving early treatment.[57] If the initial effects of the injury reduce blood flow into and out of the injured region, the hypoxic conditions alone that result will themselves cause more damage to the affected tissues.[58] A technique that could be sensitive to the presence/absence of blood would seem to be appropriate to detect this.

To seriously consider the question, we need to be much more specific about the kind and extent of injury and the new kinds of information that are now available thanks to improvements in enabling technologies over the past ≈ 30 years. Near infrared light sources, specifically lasers, improved spectral filters and gratings and charge coupled device (CCD) based detectors have made noninvasive in vivo and ex vivo Raman spectroscopy in the physiological spectral window routine. Experience in performing spectroscopy in turbid media commonly presented by medically interesting samples has spawned new approaches for quantitative and qualitative analysis of such systems in general.

3.1.4 The PV[O]H Algorithm

One new approach is "PV[O]H" (described in detail below) which we developed to probe the peripheral microcirculation in order to more accurately perform quantitative Raman spectroscopy for blood and tissue analysis. A single near infrared (NIR) laser is directed onto the tissue and both the elastically scattered light (EE) and the in-elastically scattered light i.e. light of longer wavelength (IE) than was initially directed onto the tissue are collected. With these two types of remitted light measured, the PV[O]H algorithm allows a direct calculation of the hematocrit (Hct) and vascular volume (VV) in e.g. perfused tissue. To provide a frame of reference, the PV[O]H device is calibrated using Hct changes that occur in blood during dialysis as characterized by the CritLine device, an FDA approved device that measures the Hct of the blood inside a dialysis machine.

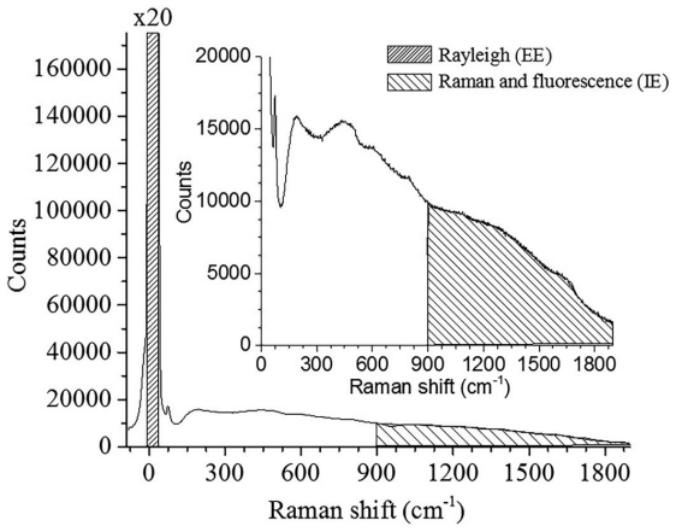

Figure 3.1. inset: raw typical single 20 msec frame of CCD output using 200 mW of 830 nm excitation on a human fingertip, bottom: same frame showing sections of emission integrated to estimate inelastic emission (IE, ≈ 500-1750 cm-1) and elastic emission (EE, -30 - +10 cm-1).

Probing nearly any biological material with NIR laser light produces a remitted spectrum roughly as shown in Figure 3.1. IE contains both Raman scattered light, phosphorescence and fluorescence and we use both together as shown in Figure 3.1.[11] The important point here is that EE and IE are produced by two fundamentally different processes and so equations that describe their observation are independent. In addition there are two fundamentally different processes that account for the observed EE and IE 1) absorption of incident light and 2) propagation of light into and out of the sample.

The volume fractions for red blood cells (RBCs), plasma and "static tissue", which we take for everything else in the cord, sum to unity implying that there are no voids. This is summarized in equations 1 and 2 using ϕ for each of the volume fractions, i.e. RBCs, plasma and static tissue in the probed volume.

$$1 = \phi_r + \phi_p + \phi_s \qquad (1)$$

$$0 = d\phi_r + d\phi_p + d\phi_s \qquad (2)$$

We used the Radiation Transfer Equation (RTE)[12] to propagate the incident light from air into a three phase, three-layer medium in the single scattering limit and with the phases, i.e. the RBCs, plasma and static tissue distributed homogeneously in the probed volume. We implicitly assume that RBCs and plasma inside the cord volume have the same optical properties as those freely circulating elsewhere. Since in skin we were able to obtain agreement with experiment by summing contributions to IE and EE *linearly*, and the scattering coefficients for skin are within a factor of 2 for those of cord tissue, and still at least one order of magnitude less than that for RBCs, we expect that we can write two independent linear equations:

$$\mathrm{EE} = \vartheta_1 + \vartheta_2\phi_p + \vartheta_3\phi_r \qquad (3)$$

$$\mathrm{IE} = \vartheta_4 + \vartheta_5\phi_p + \vartheta_6\phi_r \qquad (4)$$

From the definition of hematocrit (Hct) we have equation 5.

$$\mathrm{Hct} = \phi_r/(\phi_r + \phi_p) \qquad (5)$$

The 6 parameters in (3) and (4) can be determined using the RTE and published scattering and absorption coefficients. Presently our interest is better served by noting that since we have 2 linearly independent equations linking 2 measured quantities, EE and IE, to the 2 volume fractions, ϕ_r and ϕ_p, for each simultaneous measurement of EE and IE, it is possible to invert equations (3) and (4) to obtain (6) and (7).

$$\phi_r = \mathrm{a} + \mathrm{b}\left(\frac{\mathrm{EE}}{\mathrm{EE}_0}\right) + \mathrm{c}\left(\frac{\mathrm{IE}}{\mathrm{IE}_0}\right) \qquad (6)$$

$$\phi_p = \mathrm{d} + \mathrm{e}\left(\frac{\mathrm{EE}}{\mathrm{EE}_0}\right) + \mathrm{f}\left(\frac{\mathrm{IE}}{\mathrm{IE}_0}\right) \qquad (7)$$

There are 6 parameters (a, b, c, d, e and f) for which we must obtain numerical values. We can do this using constraints based on empirical data or assumptions.[10] EE_0 and IE_0 are values obtained at the start of probing and in this formulation of the algorithm, all subsequent variation of EE and IE are with respect to these values. This approach originated in the observation that the clinical utility of all vital signs and images resides I their evolution with the state of the patient. Thus, the apparent values of "ϕ_r" and "ϕ_p" so obtained are with respect to some arbitrary choice of starting values. In the present case, the device was calibrated is such a manner that the starting reference point is Hct=28.65 and all figures and graphs presented herein will reflect that choice. Since we are interested in *changes* in the cords over time, and do not want to recalibrate from test subject to test subject longitudinally or transversely, the choice of starting point in this methodology exploratory study is arbitrary at this point.

In the context of SCI, the interpretation of the PV[O]H response is less specific although the applicability to an existing state of inflammation seems promising. Restricting our attention to probing inflamed, near surface tissues with NIR light, for example skin, the heat, redness and swelling noted by the ancients would be in full view, being evidence in modern terms of edema, greater vascular volume of blood within the microcirculation and overall increased blood flow within the inflamed tissue. These are exactly indications for use of the PV[O]H response. The pain and loss of function may also be accessible optically because the flexing of muscle impeded by edema and extravasated blood results in modified blood movement with a recognizable time profile.

We imagine a clinical setting immediately after an SCI, and the cord has been accessed surgically in order to be probed optically without any need for further physical insult or sampling of any tissues, and that the access would be closed when "noninvasive" NIR probing is complete.

Surgical flaps may be possible to provide repeated access over limited periods of time or, depending on circumstances and the kind of information sought, the SCI might be as accessible for optical probing endoscopically using fiber optics. In the case of an exposed cord, scanning the laser across the tissue surface and performing PV[O]H at designated locations would allow "PV[O]H" images to be constructed as shown in Chapter 2.

The degree of redness and edema present would be directly accessible by PV[O]H as Hct and VV but also increased fluorescence for any reason may offer additional information. Since the probing light must penetrate the surface of any tissues in question to produce detectable IE, and the reflective loss at the surface follows the variation in the angle of incidence in accordance with the Fresnel equations, the physical topography and topology of the cord will also be manifest in the PV[O]H response. Using the EE by itself would be optical profilometry and would also allow mapping the surface topography of the cord.

The degree of swelling affects the topology of the cord and that may or may not change over the course of time after injury. The variation of any apparent edema, quantified as apparent Hct and VV, leads to a check for internally consistent imaging. Perhaps most importantly, if Raman spectroscopy is included in the capacity to perform PV[O]H imaging as was originally intended, then the chemistry of the injured cord can also be accessed simultaneously.

The goal of this paper is to utilize the principles of Raman spectroscopy as well as the PV[O]H algorithm to non-invasively examine the spinal cord of rats and extract both chemical and physiological information as a result of insult. This will be done by both examining the components of spectra separately, independently assigning Raman peaks to certain chemicals and utilizing calculation and extrapolation to determine the pH of the system and thus one physiological response to the insult. Because it was not possible to collect rat CSF to validate

the Raman based pH algorithm against conventional analysis, CSF was physically sampled from a pig model perimortem and the pig cord was subjected to the same spectroscopic probing. The physically sampled CSF was found to have a pH by conventional analysis essentially in agreement with the pH measured by Raman spectroscopy.

3.2 Experimental

3.2.1 Rat Surgery

The animal protocol used was approved by the Institutional Animal Care and Use Committee (IACUC) of Syracuse University in compliance with National Institute of Health (NIH) guidelines. All surgical procedures were performed in a sterilized surgical suite located in the Laboratory Animal Research (LAR) facility at Syracuse University. Six female Sprague Dawley rats, at weight range 250g to 330g, were purchased from Charles River Laboratories and housed in LAR at least two weeks prior to surgery to acclimate to the environment.

Animals were anesthetized using a procedure standardized in LAR for rat surgery with approval by a certified veterinarian. Each animal was placed into a sealed chamber and 5% isoflurane (Shopmetvet, Mettawa, IL) was allowed to flow for 2 minutes until animal responses were minimal. After initial anesthetization, the animal was removed from the chamber and a nosecone was attached to the animal to continually flow 2% or 2.5% (dependent on size) isoflurane throughout the procedure. The surgical area was shaved and sterilized using alcohol and betadine-soaked pads. A hot water therapy pump (Braintree Scientific, Braintree, MA) was used to regulate the temperature of the animal throughout the procedure and was placed at 37^{o}C prior to anesthetization. All surgical tools were sterilized using a micro glass bead tabletop autoclave for 2 minutes per manufacturer instructions to ensure sterility throughout the whole experimental process.

The locations of vertebrae T8 through T11 were verified through touch along the spine as both T8 and T11 spinal processes were more pronounced than surrounding vertebrae. A final check was made to ensure deep anesthetization by blink reflex and tail twitch tests detailed in IACUC requirements. An approximately 1-inch long incision was made along the spinal column from T8 to T11 using a #10 scalpel blade (Fine Science Tools, Foster City, CA). A hole was then cut into the fat layer beneath the skin using surgical scissors (Fine Science Tools, Foster City, CA) and blunt dissection was used to separate the muscle and fat layers. The fat layer was cut and moved away from the surgical area. In parallel, incisions were made through each of the three muscle layers on either side of the spine. The position of the spinal processes was used to verify the location of T9 and T10 by moving the back of the scalpel along the vertebral column; incisions were made perpendicular to the spine between T8 and T9, T9 and T10, and finally T10 and T11. Muscle was gradually dissected using both surgical shears and a scalpel to expose bone. The dorsal layer of bone for T9 and T10 was removed to expose the spinal cord to a full length of at least 1 cm using Friedman-Pearson Rongeurs (Fine Science Tools, Foster City, CA). The area was cleaned using a saline spray and sterile cotton balls. After completion of all experiments, all animals were euthanized under anesthesia by either an overdose of 0.5ml pentobarbital (Sigma-Aldrich) by intraperitoneal injection or asphyxiation via a CO_2 chamber.

3.2.2 Impactor Set-up

The injury model for a rat and all techniques for creating a contusion injury were developed by Rutgers University's W.M. Keck Center for Collaborative Neuroscience division[59]. The contusion injury was produced using the Multicenter Animal Spinal Cord Injury Study (MASCIS) Impactor model III using the standard 3mm size impaction tip at 12.5mm above the spinal cord. These parameters have been previously shown to induce a moderate level of spinal

cord injury. All animals were aligned beneath the impactor regardless of injury to ensure spectral consistency between all injured and control animals.

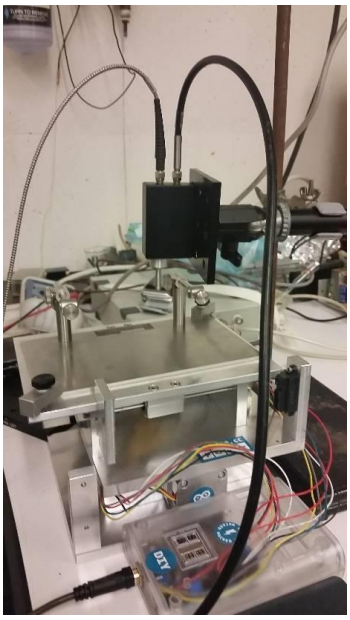

Figure 3.2. Early experimental set-up for rat surgery. The animal was placed on the X-Y stage and moved in predetermined patterns described below. Incident light hit the spinal cord at 90 degrees and was backscatter light was collected.

3.2.3 Line Scan Procedure

To scan across the spinal cord of the animal a programmable x-y stage was developed to move in a pre-determined path (figure 3.3). An Arduino microcontroller, using a custom-built MATLAB script, controlled two separate stepper motors independently with steps as small as 10 microns. The probe for the laser was fixed above the stage set 90 degree to the spinal cord position. The probe was also placed on the stationary portion of the stage, allowing the stage to move and keep the light path in a fixed position. After the surgical procedure, the animal was carefully moved to the stage to avoid agitating the surgical area. Two vertebral clamps on the stage platform were attached to T8 and T11 to minimize animal movement during scanning and straighten any curvature in the cord.

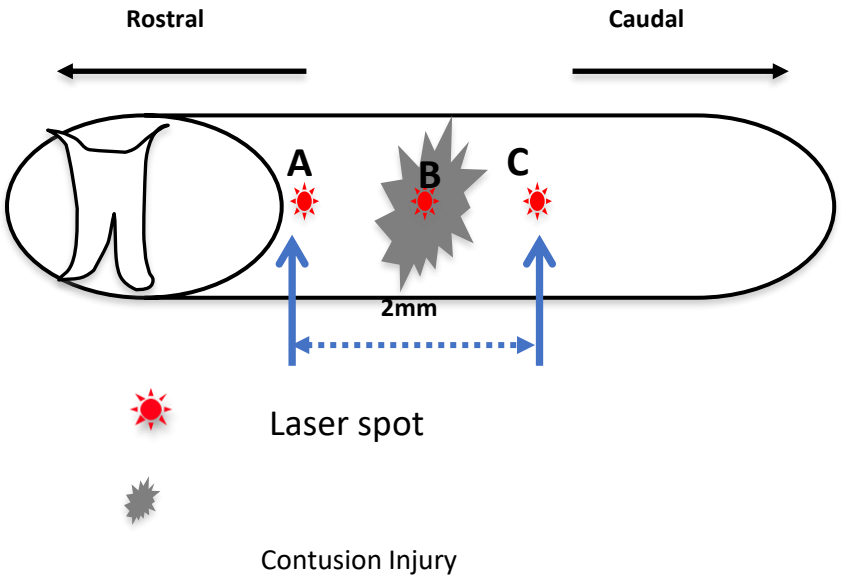

Figure 3.3. Schematic of experimental injury and path of light. A, B and C are nondescript areas where the laser light was staged for 5 minutes. A 5 minutes scan from one point to the next was also conducted. Contusion injury occurred at point B.

To ensure the injury location on the cord, the stage was modified to include a rail that extended out to the impactor. The probe and focal length were set manually before the animal was moved to the impactor. Three positions (A-C) were determined along the spinal cord based off the insult point of the impactor. Position B was determined as the spot of impact as Position A and C were spaced roughly 1 mM each way (toward the head and toward the hind respectively) on the cord. This allowed for no potential overlap between spots as the spot size of the laser is roughly 100 microns. This also ensured each spot would be on the cord and not surrounding bone/tissue.

Equal scanning times were achieved for each of the three positions along the spinal cord by placing the stage stationary with light on each point for 5 minutes and scanning from one point to the next for a duration of 5 minutes each, giving a total time of 25 minutes. Once the scanning process was complete, the laser was turned off and the stage returned to the initial position while the animal was monitored to ensure adequate hydration of the injury site as well

as continued respiration and anesthetization were maintained throughout the procedure. This procedure was completed a total of 11 times (1 before the impact occurred and 10 following impact) for all animals.

3.2.4 pH Calculation and calibration using PBS

PBS solution was made by dissolving 1 PBS tablet (ICN Biomedicals Inc.) in 100 mL of deionized water. Starting pH was measured at 7.29 using a Vernier LabQuest pH probe. pH was then varied by adding either 1 M hydrochloric acid to lower the pH or 1M sodium hydroxide to raise it, dropwise into stock solution while stirring. Sample was taken from the stock solution and placed into cuvette for analysis after pH stabilized. The final range of pH in the samples was from 3.30-10.20.

3.2.5 Pig Spinal Cord Surgery

All pig procedures were done perimortem as described below. after 1) completion of an unrelated initial procedure associated with lung research, 2) euthanasia and 3) after insuring there was no respiration or cardiac response. A section of spinal cord in a region similar to that used for the rat model was exposed, rinsed with saline and left intact. As for the rat model, the surface of the cord was misted with saline at regular time intervals to avoid burning or other obvious tissue damage while spectra were being measured. For the pig model, 2 separate animals were available within the available time interval. When initial procedural treatment was done the pigs were flipped on stomach and the cord of the pig was exposed, similar in location to the rat. The pig was then euthanized and while euthanasia was taking place, i.e. the “peri-mortem” phase, the first scan was taken.

For the scans, the probe of the laser is placed such that the focal point of the laser is placed “inside” the cord. Three consecutive measurements of five minutes are taken on one spot of the cord. After the third scan a sample of CSF is taken from the cord and the same three measurements are taken.

3.2.6 Spectroscopy

For the rat studies the spectroscopic measurements employed a modified commercial 830 nm Raman spectrometer (Lambda Solutions, Waltham, MA). The rest of the optics and filtering was standard for Lambda Solutions probes but there was an additional Raman notch filter (Semrock, Rochester, NY) placed between the collimating lens and the grating to allow adjustment of the elastic signal (EE) and inelastic signal (IE) for optimum range in the hematocrit calculation. A standard Raman normal incidence probe having a focal length of 1 cm was used with an effective numerical aperture of ≈0.13 and the smallest spot size was ≈100 μm. The exterior surface was contacted directly with 80 mW CW light. For the pig studies a BWTek i-Raman Pro HT785 785 nm laser was employed to test for portability in later studies. This laser had focal length of roughly 1 cm and a measured power or roughly 250 mW CW light. 300 1 second measurements were averaged together for data output on this device.

The Data output for the rat studies was collected in real time using the algorithm described in the introduction to this thesis. Upon completion of the experiment the raw files were compressed into excel documents using a MATLAB script previously created by the Chaiken lab. Each run created both an apparent hematocrit output file as well as Raman spectra for each run. These spectra were used for analysis in the line scan experiments. All spectra were then treated with a “101-7” baseline correction with a fingerprint region from 400 cm^{-1} to roughly 2400 cm^{-1}.

3.3 Results

3.3.1 Line Scan

Line scanning was performed as described above. The height of the surface of the animal changes as does the angle of incidence depending on the surface topography of the cord, which could change over the course of time due to fluid movement or swelling. As can be seen in Figure 3.4, the apparent Hematocrit (Hct) is calculated continuously, from the previously described algorithm as the cord is moved, as well as at a single location (hold) when the cord is stationary.

At each Hold location, the Hct is seen to increase, regardless of location or whether the cord was injured or not. While in motion between locations, the Hct initially always decreases and then a variety of Hct responses are observed, including very sharp and deep dips such as near 360 Hemocycles in either the pre-injured or 1st post injury scans in Figure 3.4.

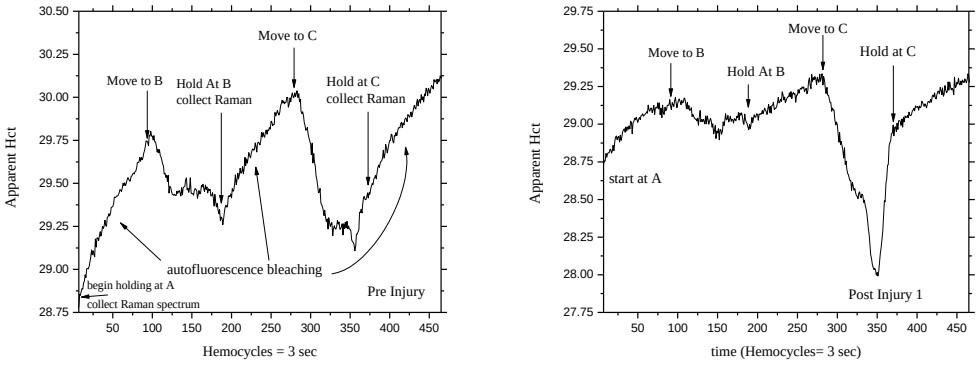

Figure 3.4. Line scans pre-injury and post-injury as described in experimental sections.

The total IE at 1078 cm^{-1} was collected for these 33 measurements were plotted semi-logarithmically in Figure 3.5. Despite there being 3 different locations, the linearity of the result indicates that there is an exponential decay in IE during the data collection in the “Hold” at each location, while the EE does not change in such a way. This indicates that autofluorescence photobleaching occurs and that the spatial registration of the scanning system is reproducible and precise to within plus or minus the diameter of the laser spot (100 microns).

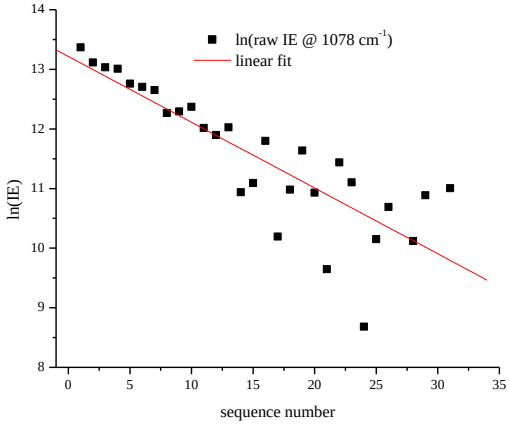

Figure 3.5. Semi-log plot of IE for all scans over the initial 5 hours post-SCI including the pre-injury scan.

The same data was collected over the progression of the SCI initiated event; 11 scans over 5 hours for this experiment are shown in Figure 3.6. Note that as the number of successive scans increases, the increase in Hct at each “Hold” position diminishes, indicating that whatever material is being bleached, it is not replaced in the time interval between successive scans. This means that while there is almost certainly some emission from RBC and plasma (blood), the bleached material is not blood, since it is totally and continuously replaced in seconds from the probed volume.

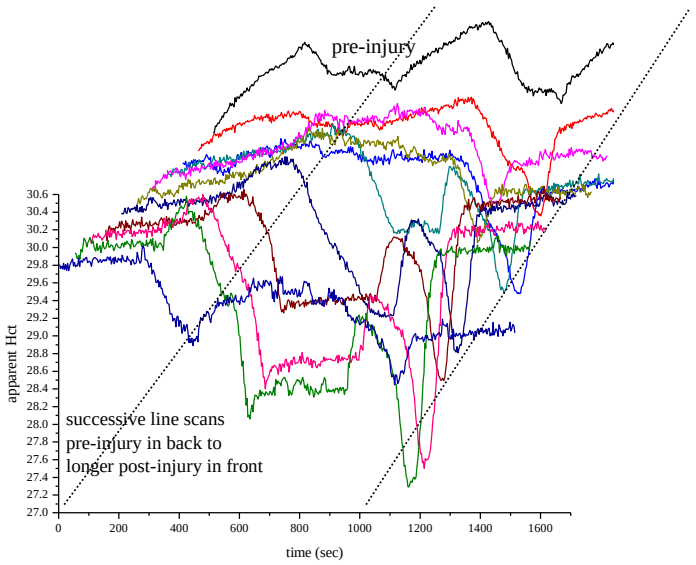

Figure 3.6. All 11-line scans pre and post injury in a single SCI experiment. Note that this is an "injury" experiment and control experiments were the same, including total time intervals, except no impaction/injury was performed.

To verify Raman acquisition was based on spinal cord tissue and not surrounding tissue, samples were acquired (figures 3.7-3.8) and compared to previous work performed in the lab as shown in Figure 3.9. Despite differences in preparation, similarities across all samples can be seen.[43,60] Particular peaks of interest include 1445cm^{-1}, 1300 cm^{-1}, 1070 cm^{-1}, 950 cm^{-1}, and 700 cm^{-1} that can be compared across all samples. Differences between groups could be explained by live imaging compared to *ex vivo* Raman acquisition.

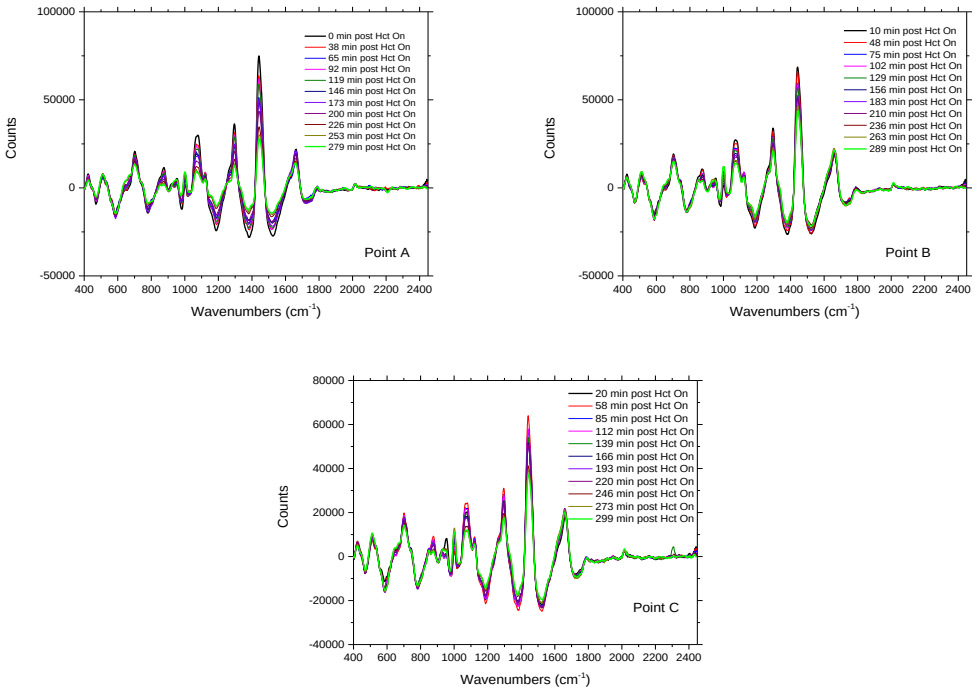

Figure 3.7. Depiction of spectra of points A, B, and C in an injured spinal cord. Note that the first time point in each scan (0, 10, 20 minutes) is taken before the contusive injury.

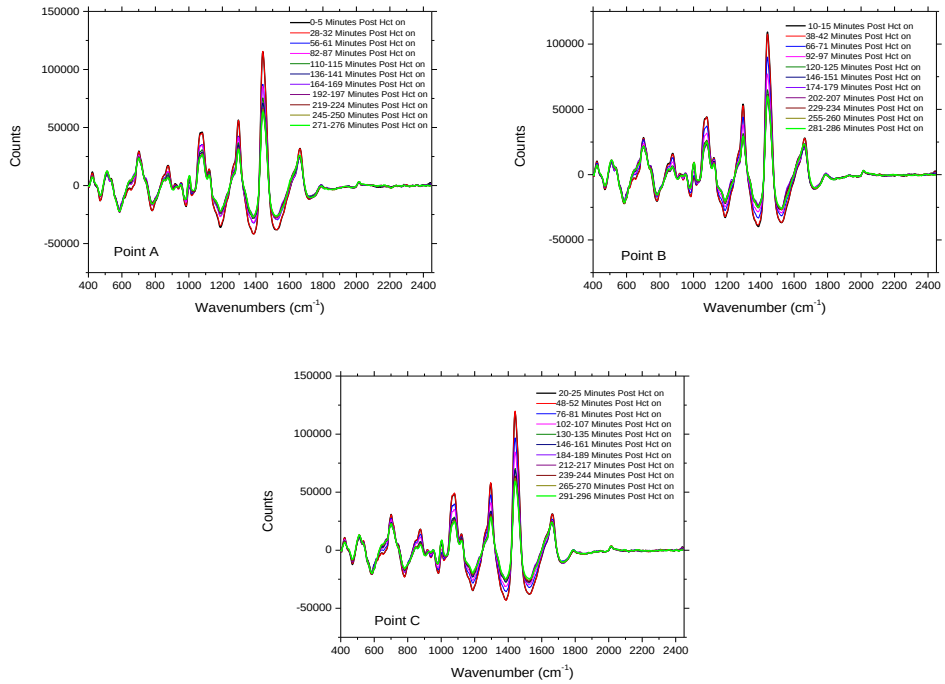

Figure 3.8. Depiction of spectra of points A, B, and C in a Control spinal cord.

Specific peak numbers were assigned to represent ranges as shown in Figure 3.9A. Peak selection was determined based on previous as well as areas in which there were apparent changes over the course of the experiment. Definition of a peak was determined by comparing inflection points in the data where peaks would change direction to allow machine based unbiased peak ranges. This enabled more focused definition of specific peak values and ability to obtain quantitative values for peak area both reliably and reproducibly. Tentative vibrational group assignments were based on Raman spectra of biochemical markers relevant to spinal cord tissue. Simple comparison of peak areas from the first Raman spectrum of the series to last showed statistically significant differences for many features.

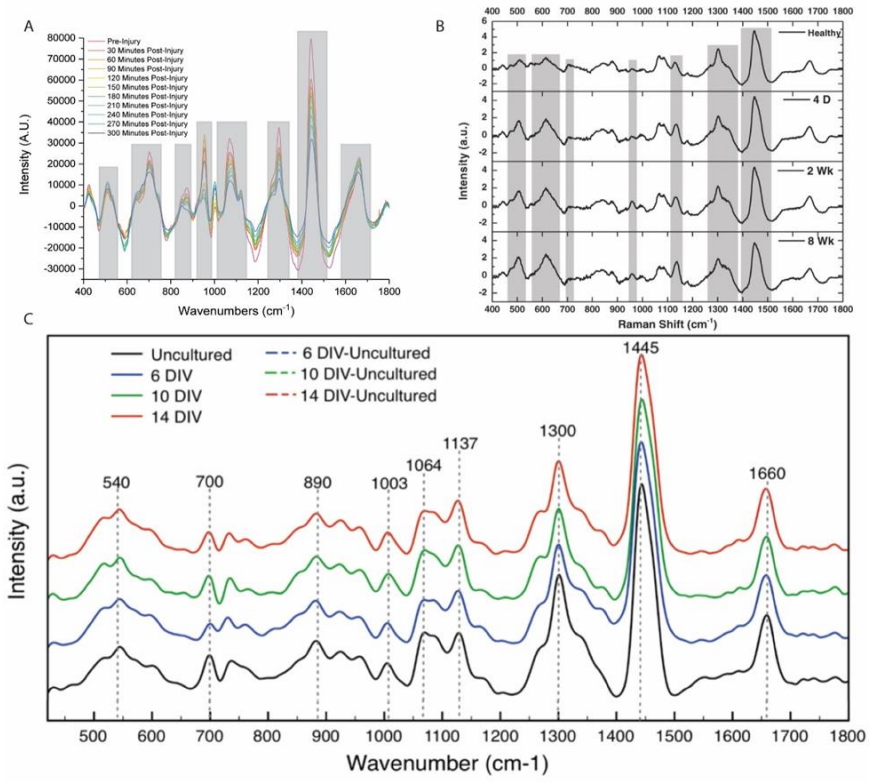

Figure 3.9. A). Representative sample taken from current work. Grey lines are indicative of peaks that either correlate with the other sources or peaks that are unique. Data truncated to 1800 cm-1to visualize entire spectrum compared to other graphs. B). Previous Raman lab data depicting perfused intact spinal cord at various time points after hemisection lesion injury. Note similar bands of peaks compared to graph A. C). Previous lab Raman data depicting peaks obtained from organotypic slices of artificial cerebrospinal fluid infused tissue. Images were taken perpendicular to dorsal section of spinal cord compared to other graphs. Like graph B, graph C also shows a comparable peak assignment to graph A[43]

Figure 3.10 contains the gross features of all spectra at all locations and for either injured or control animals. The usual features of CH_2 deformation, amide linkages I and III, as well as water at or near 1450 cm^{-1}, 1660 cm^{-1}, 1300 cm^{-1} and 1670 cm^{-1} respectively are visible and changing over time. This resembles work previously done. We noticed however that below 1200 cm^{-1} there is similar activity for both injury and control animals that we show in greater detail in Figure 3.11. The activity below both decreases and increases at specific wavenumbers as indicated by the arrow whereas above 1200 cm^{-1} Raman activity appears to decrease monotonically.

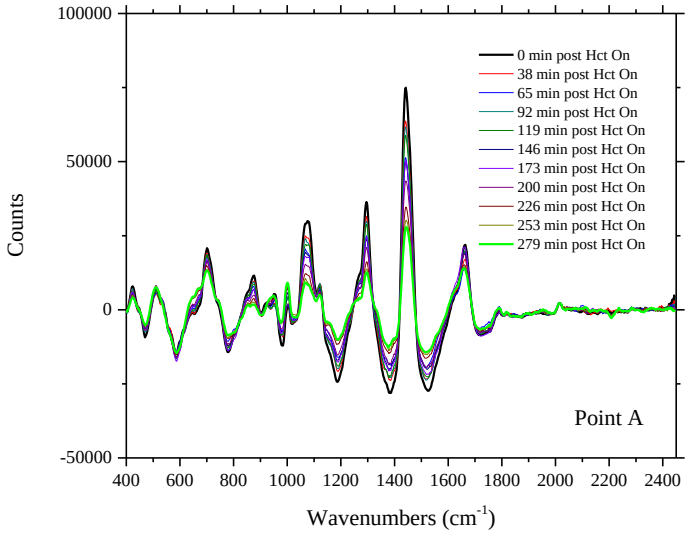

Figure 3.10. 101-7 baseline corrected Raman spectra collected at position A on a spinal cord over 334 minutes post first laser exposure and 314 minutes post SCI at position B.

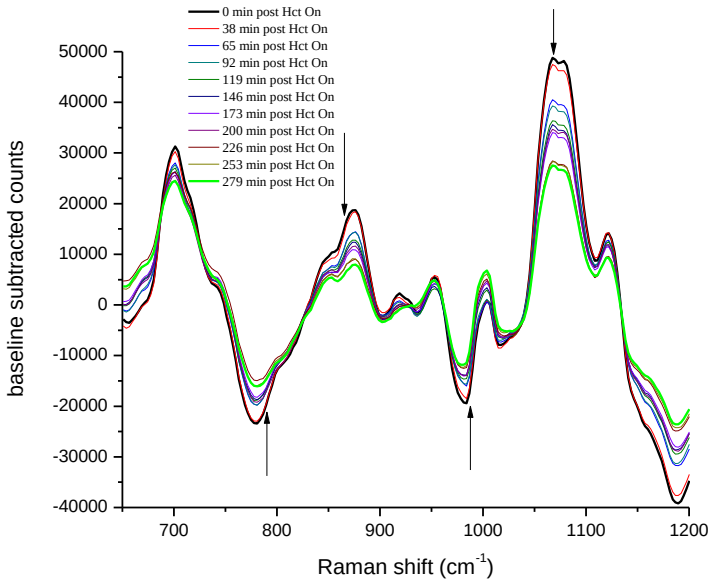

Figure 3.11. expanded scale of different 101-7 baseline corrected Raman spectra collected at position C on a spinal cord over 300 minutes post first laser exposure and 314 minutes post SCI at position B. Arrows show Raman features due to aqueous phosphate ions $H_2PO_4^{-2}$ and HPO_4^{-1}.

3.3.2 Line Scan PCA and Statistical Analysis

Principle Component Analysis (PCA) was performed to further examine the individual components that make up the full spectrum of the cord and to observe possible changes that may be occurring between injury and control animals. This was also done to determine if in fact inorganic phosphate was a strong contributing factor of the cord (determined from the area below 1200 wavenumbers in figure 3.11). Due to the number of variables and high similarity among the timepoint scans, data was compiled into two sets, injury and control (n=3 for each), to observe variance of each position across all timepoints.

Three components capture greater than 99% of the variance in the data. Representative graphs of the averaged PCA loadings for both groups are shown in Figures 3.12-3.14. Loading graphs show the prominence of a Raman feature on the original data, with greater magnitudes indicating greater influence.

The high similarity of the first component peaks to those of the original data suggests that the first component is likely the static tissue of the cord. The amount of variance accounted for, ~ 95%, also explains that most of the spinal cord being measured would be tissue. The second component is believed to contain a large contribution from cerebrospinal fluid. The presence of a peak in the at 662 cm^{-1} could be indicative of bicarbonate and is explained by the high concentration of bicarbonate in spinal fluid.[61,62] The third component is likely explained by plasma; however, a relatively low amount of variance, less than ~1%, shows a low signal to noise ratio as compared to the other two components, making the exact composition difficult to rationalize. Possibly, the sharp feature near 962 cm^{-1} originates with glutamate as it is the most abundant neurotransmitter in the synaptic cleft. Moreover, the release and reabsorption of glutamate is an essential function of normal neural homeostasis and this would be interrupted, at least locally, by physical disruption i.e. SCI.

We note that with the coefficients that emerge from PCA, these loadings represent variation of chemical species over time. Thus, it's natural to attempt to analyze the loadings in terms of the spectra of specific chemical species. Some sets of features e.g. Raman features below 1200 cm^{-1}, and others, appear to vary in concert, perhaps linearly related. The major point being taken away from the PCA being that this variance could be indicative of changing phosphate concentrations.[13] If we were able to somehow quantify the change, we could theoretically calculate the pH of the CSF over the course of the experiment. The hypothesize that there would be a myriad of physiological and biochemical mechanisms by which pH could reveal the course of chemical change after SCI.

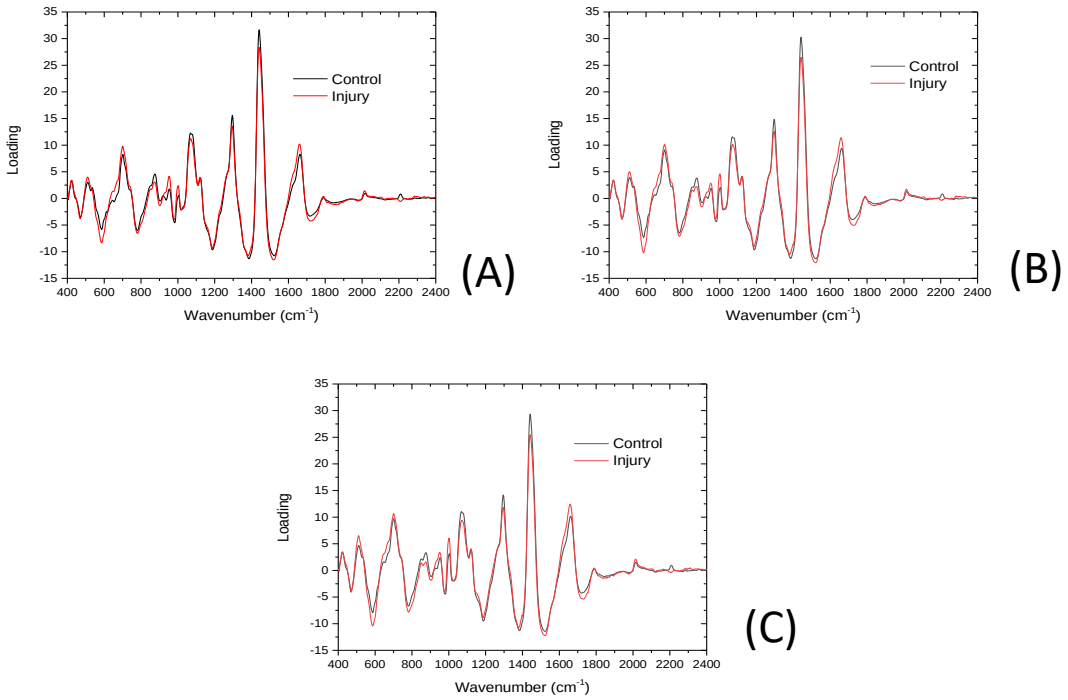

Figure 3.12. Graphs depicting the first principal component at each position for both injury and controls (A is point A, B is point B, C is Point C).

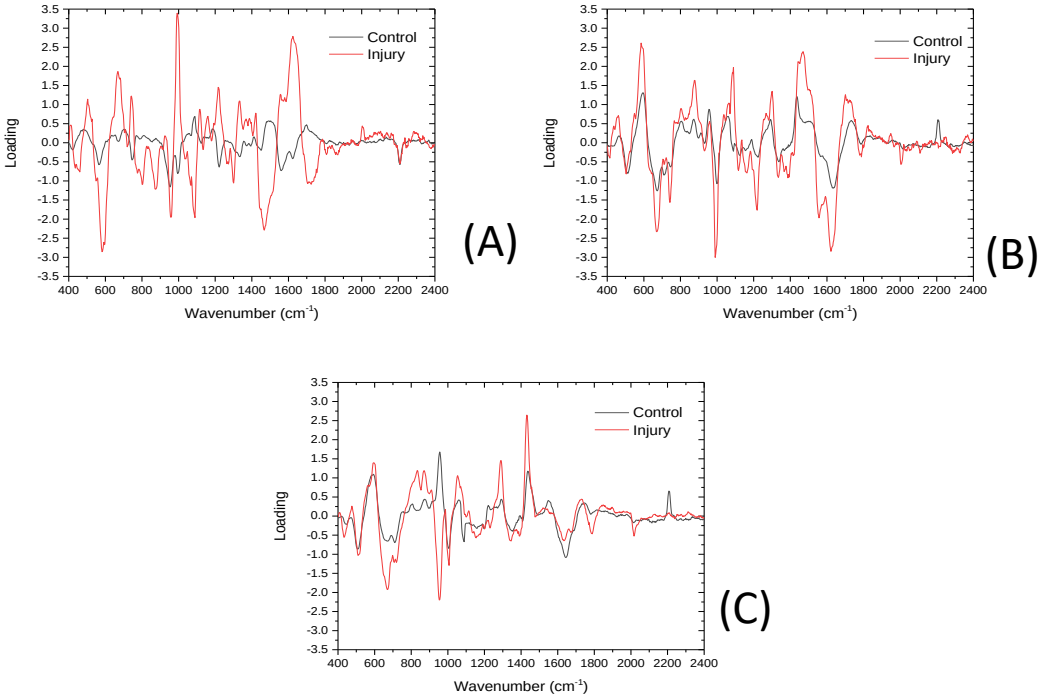

Figure 3.13. Graphs depicting the second principal component at each position for both injury and controls (A is point A, B is point B, C is Point C).

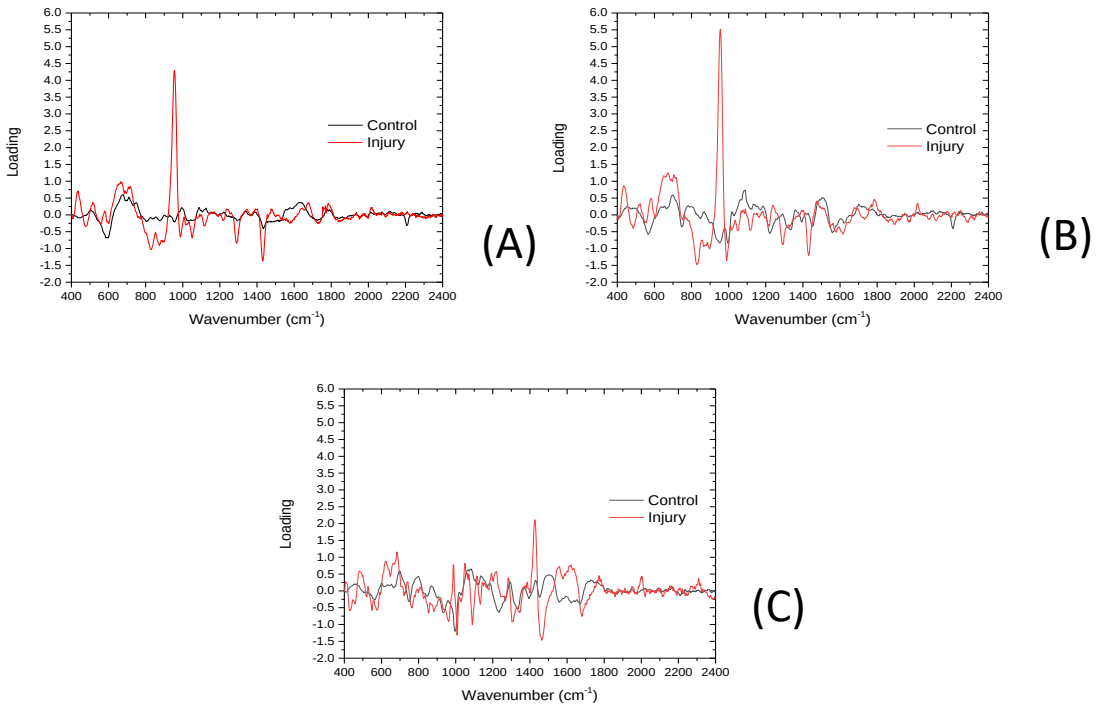

Figure 3.14. Graphs depicting the third principal component at each position for both injury and controls (A is point A, B is point B, C is Point C).

3.3.3 pH analysis of SCI

In this partial account of this study we focus on the Raman spectra and loadings below 1200 cm^{-1} as explained above. Given the composition of CSF, which contains much less protein than serum or cells[63] we hypothesized that Principal Component 1 is associated with the structural materials in the probed region of the spinal cord. This would include all solid/soft materials within a millimeter of the cord surface. If there were very large numbers of cells present in the inflammatory response to the injury, *perhaps* they might contribute. But considering the Raman shifts involved and the relatively small contributions of the 2nd and 3rd components to the overall variance, the electrolytes in CSF may be involved.

We initially consider bicarbonate which is present in CSF normally in about 20-24 mM concentration and would be expected to vary over time if the oxygenation of any animal changes over time, injured or control. Various attempts to assign observed Raman features in the loadings and spectra themselves to bicarbonate and/or carbonate fail to account for 1) all known features and 2) relative variation of different Raman features supposedly originating from the same species as will be discussed below. In considering phosphate even though the normal CSF concentration is only about 1.5 mM, all hydration and cleaning of the surgical field was carried out with normal saline i.e. no added phosphate as in PBS. We obtained the spectra in Figures 4.15 and 4.16 from phosphate buffered saline (PBS) at a range of pH values as indicated with minimum volumes of 1 M HCl and 1 M NaOH being used to adjust the pH.

We note that PBS has no 1450 cm^{-1} nor 1300 cm^{-1} nor any other indicator of protein, lipid or carbohydrate. In fact, all features present above 1200 cm^{-1} in the SCI spectra are missing from the PBS spectra except that of water. The arrows in Figure 3.15 are in the same wavenumbers as the arrows in Figure 3.16 and the exact wavenumbers used were obtained from Heighton[13] et. al. Below 1200 cm^{-1} the spectra closely resemble those of the rat cords in vivo. Figure 3.16 shows this more clearly and the arrows show Raman features due to aqueous phosphate ions $H_2PO_4^{-2}$ and HPO_4^{-1}. Note that essentially 1) all the features of phosphate are accounted for in the spinal cord spectra over time and 2) their mutual variation is exactly consistent with the variation of pH as shown in Figures 3.17- 3.20 below.

In fact, Oliver and Davis[64] performed similar experiments with bicarbonate as Heighton et. al did with phosphate showing that it is possible with Raman spectra to account for pH variations in aqueous solution. The data in figures 3.17-3.20 result from the titration of phosphate with the specific wavenumbers corresponding to the same ones shown by Heighton et. al.[13]

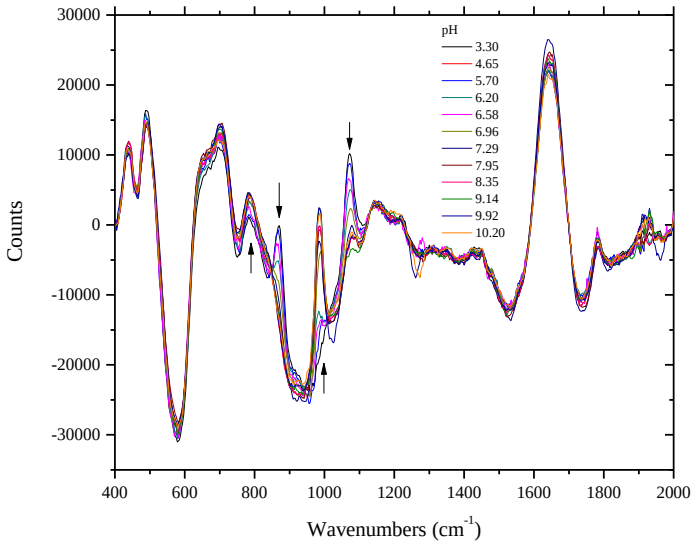

Figure 3.15. 101-7 baseline corrected Raman spectra collected at same laser power and collection time of PBS which is 10 mM in total phosphate.

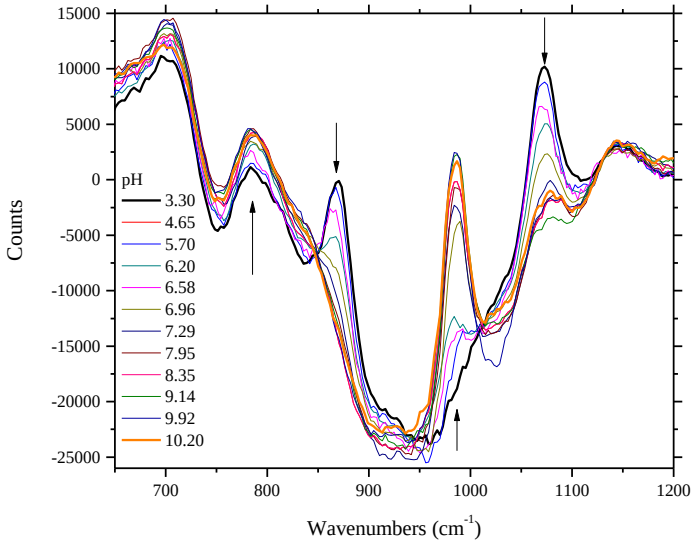

Figure 3.16. 101-7 baseline corrected Raman spectra collected at same laser power and collection time of PBS which is 10 mM in total phosphate.

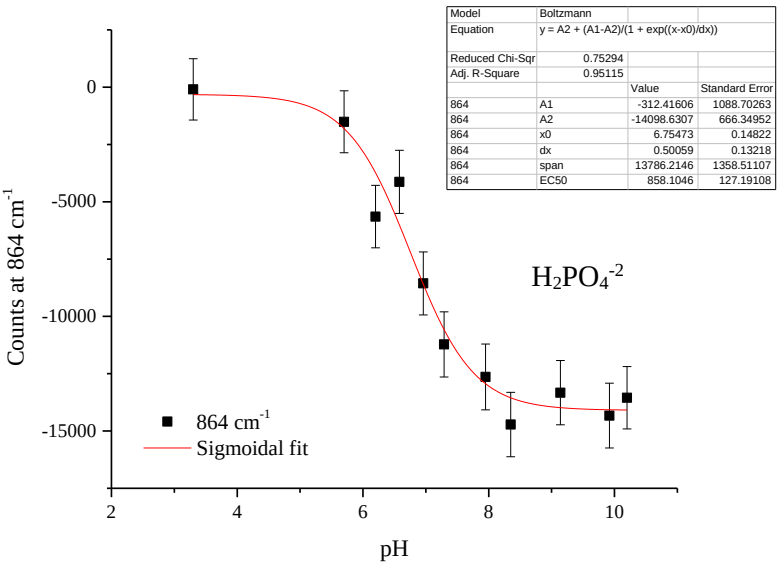

Figure 3.17. sigmoidal fit to data taken from raw Raman spectra of PBS as in Figures 3.15 and 3.16 for PBS. Error bars represent 2σ of raw data.

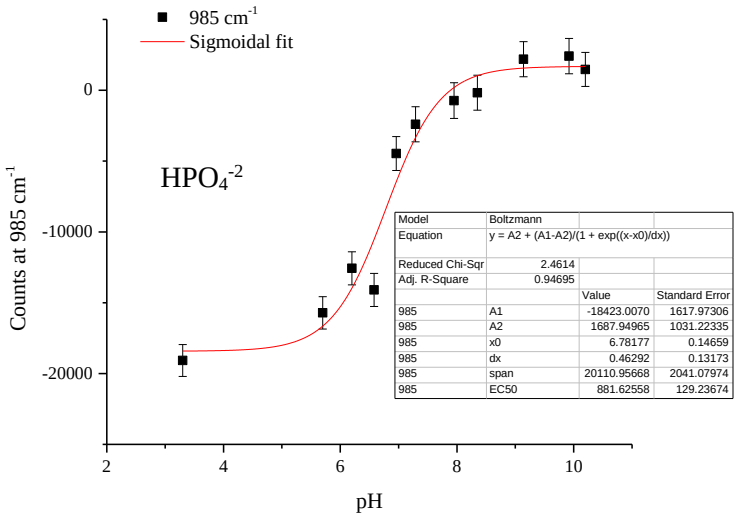

Figure 3.18. sigmoidal fit to data taken from raw Raman spectra of PBS as in Figures 3.15 and 3.16 for PBS. Error bars represent 2σ of raw data.

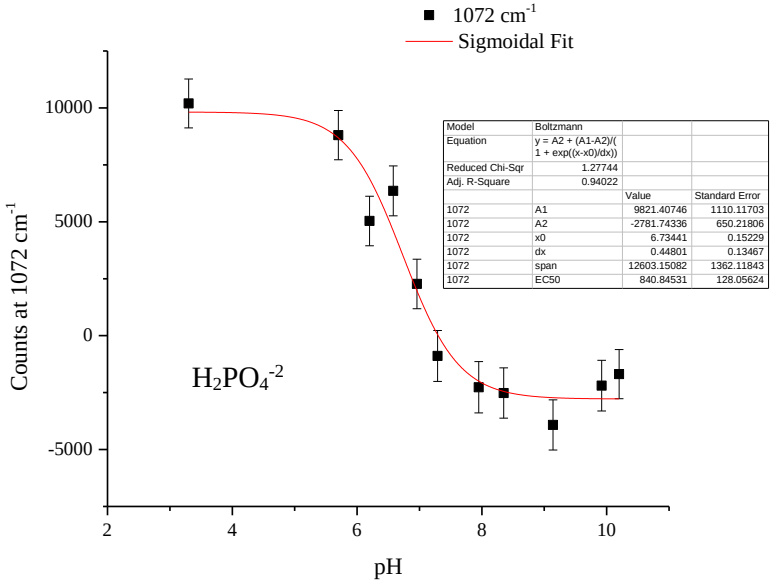

Figure 3.19. sigmoidal fit to data taken from raw Raman spectra of PBS as in Figures 3.15 and 3.16 for PBS. Error bars represent 2σ of raw data.

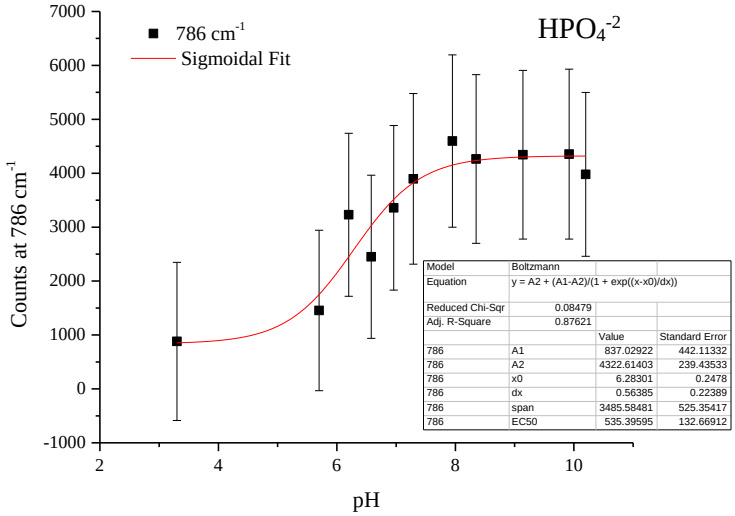

Figure 3.20. sigmoidal fit to data taken from raw Raman spectra of PBS as in Figures 3.15 and 3.16 for PBS. Error bars represent 2σ of raw data.

The titration involved is represented by equation 1 with equilibrium constant pK_{a2}.

$$H_2PO_4^{-1} \leftrightarrow H^+ + HPO_4^{-2} \qquad pK_{a2}=7.2 \qquad [1]$$

Equation 2 relates the equilibrium constant in terms of concentrations.

$$K_{a2}= [H^+][HPO_4^{-2}]/[H_2PO_4^{-1}] \qquad [2]$$

And using the definitions of pKa and pH we obtain [3]

$$pH= pK_{a2} + \log([HPO_4^{-2}]/[H_2PO_4^{-1}]) \qquad [3]$$

There are a variety of approaches[65] to calculate the pH of the CSF in the probed volume using this data. For example, the data in Figures 3.17- 3.20 can be fit to the data to obtain values for pK_{a2} for comparison with the literature. Choosing the best data, both r^2=0.96 with N=11, the sigmoidal fits to the data at 1072 and 985 cm^{-1} yield pK_{a2} of 6.78 with σ=0.15 and 6.74 with σ=0.15 respectively. Each of these values is low since in fact[66] pK_{a2} =7.2 suggesting a systematic artifact may be possible.

We note that three of the four sigmoidal fits reflect good statistical significance. Reduced chi-squared values obtained from the nonlinear fits of the 985 cm^{-1} and 1072 cm^{-1} data are 2.96 and 1.27 respectively. The 864 cm^{-1} also has a reduced chi-squared value of 0.95. The error bars are based on shot noise limited detection of the raw spectra i.e. before baseline subtraction and 95% confidence. These data are quite credible and should produce credible measures of pH. However, the 786 cm^{-1} data has a lower chi-squared value at 0.87 reflecting the fact that the span of the 786 cm^{-1} Raman signal is much smaller relative to the shot noise. This is reflected by the large 2σ error bars and lower r^2 values deem it much less usable as a viable titration curve.

To check for possible spectral overlap between the features of species involved in the equilibria, we obtained the spectrum in Figure 3.21 corresponding to high pH and no protons i.e. all D_2O and NaOD to make the solutions. This should reveal the presence of completely dissociated inorganic phosphate PO_4^{-3} since there are also no features whose Raman can be shifted downward. There does appear to be such a feature that would contribute to the observed 985 cm^{-1} in PBS and CSF but cannot contain protons. We take this feature to be associated with PO_4^{-3} and as such it would make a complicated contribution to the numerator of equation 3.

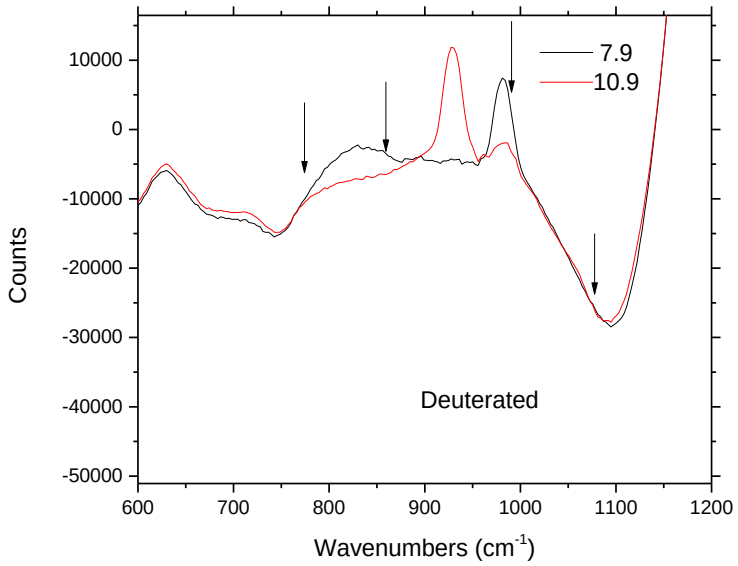

Figure 3.21. Depiction of two different pH solutions of PBS created in D_2O and made more basic with sodium deuteroxide. The arrows correspond to wavenumbers of interest from figures 3.15 and 3.16

We assume that since the pKa for the PBS calibration is known to be 7.2 and both Raman measurements gave an average pKa2 of 6.76 we should correct the CSF measurements by adding the difference i.e. 0.44 to calculated pH values from Raman features at those two wavelengths. To calculate the pH values from CSF we need to relate the number of Raman counts to the concentration of the Raman scatterer i.e. chemical species in Equation 3.

Since the concentration dependences of the various species in PBS are well known it is possible to use the titrations of the PBS itself to obtain this calibration. Utilizing the data from above and the calibration curve of PBS, created from correlating counts to concentrations[67] we were able to create a calibration curve for both concentrations of HPO_4^{2-} and $H_2O_4^-$ per counts from the data at the 985 and 1072 cm^{-1} respectively as shown in Figures 3.22. and 3.23. The assumption here is that the incremental change in observed Raman counts per unit change in mM scatterer is independent of turbidity for small enough turbidity. We have substantial evidence to

support this assumption[11,21] but the linearity of the calibrations below also suggest that we are correct.

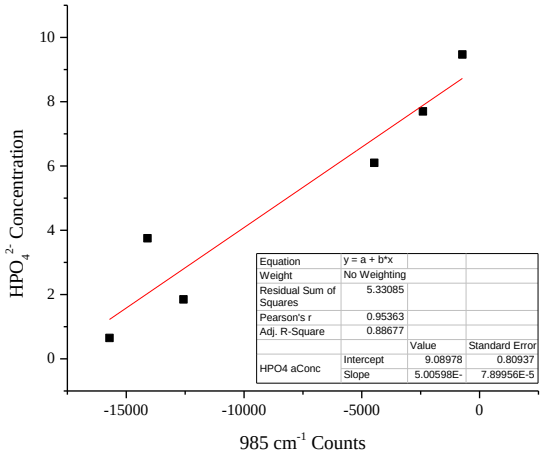

Figure 3.22. Calibration curve of HPO_4^{2-} concentration from counts at 985 wavenumbers. R-squared value of 0.89

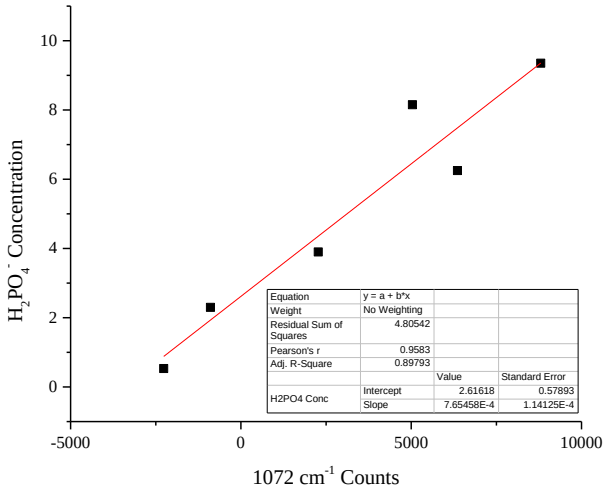

Figure 3.23. Calibration curve of $H_2PO_4^-$ concentration from counts of 1072 wavenumbers. R-squared value of 0.9

We then utilized these curves along with the equations above to calculate the successive changes in pH during each rat at each point for our 3 by 3 study.

After using a Q test[68] to remove outliers from only the control data, we could not do the Q test for the injured cords as we could not rule out that the change was due to injury, we calculated an average, standard deviation and coefficient of variance of the pH at each

successive change for both control and injured rat (n=30 for each injury and from 24-30 for control after Q test). Lastly, we pooled the whole study and compared Injury to Control (n=90 and 81 for injured and control respectively).

Table 3.1 Calculated average pH for each point for both Control and Injured cords over entire experiment and statistical correlation data.

	Injury A	Control A	P value	Injury B	Control B	P Value	Injury C	Control C	P Value
Average pH	7.10 n=30	6.89 n=27		7.05 n=30	6.83 n=27		7.05 n=30	7.03 n=24	
Standard deviation of pH	0.29	0.15	0.001	0.45	0.46	0.064	0.42	0.21	0.82
Coefficient of variance of pH	0.04	0.02	Very statistically significant	0.06	0.07	Not quite statistically significant	0.06	0.03	Not statistically significant

	Injury	Control	P Value
Average coefficient of pH	0.05 n=90	0.04 n=81	
Standard deviation of average coefficient of variance of pH	0.01	0.02	<0.0001 Extremely significantly different

With the aid of a very large n (81 and 90) we can say that the variance of the pH in the injury vs. the variance of the pH for control animal are statistically different. There is apparently more activity that would affect NIR emission spectra from the Injured cords than for the Control cords. Note that the pooling of data removes some time information from the resultant averages. So, over the entire course of an experiment, physiology in the CSF results in some pH variation even in the control animals, there is a significant difference between what occurs control cords vs. in injured cords.

Furthermore, comparison of pH at specific locations across control and injured cords shows that at 95% confidence, at location A pH is statistically different, B is different with 94.6% confidence, and C is not different. Since the injury occurs at B, something secondary occurs distal towards the brain during the time scale of our entire set of observations. Perhaps something happens later in the opposite direction i.e. towards caudal but presently we have no observations to support that speculation.

The actual measured pH of the Injured cords, where it differs from the Controls is higher. With the correction mentioned above, the averaged pH of the Controls is 7.3, in good agreement with literature-based expectations while the averaged pH of the Injured CSF was ≈7.42. We shall return to consideration of the rat model data after one more layer of validation of the Raman based measurement approach to pH measurement.

3.3.4 Pig Study Results

Our goal was to provide comparison of the pH values we measured using Raman spectra for rat spinal cords in vivo with a conventional analysis of physically sampled CSF. Sampling rat CSF is not feasible experimentally but there is good literature to guide a protocol for obtaining relevant physically sample CSF in a pig model. Though the pig protocol was slightly different than the rat for data collection i.e. one spot three times vs. three spots one time in a rat, we were still able to acquire Raman spectra of the pig cord successively for each scan both before harvesting CSF and after, as seen below in Figures 3.24 and 3.25. The spectra of pig tissue are much like those of the rats described earlier in this chapter.

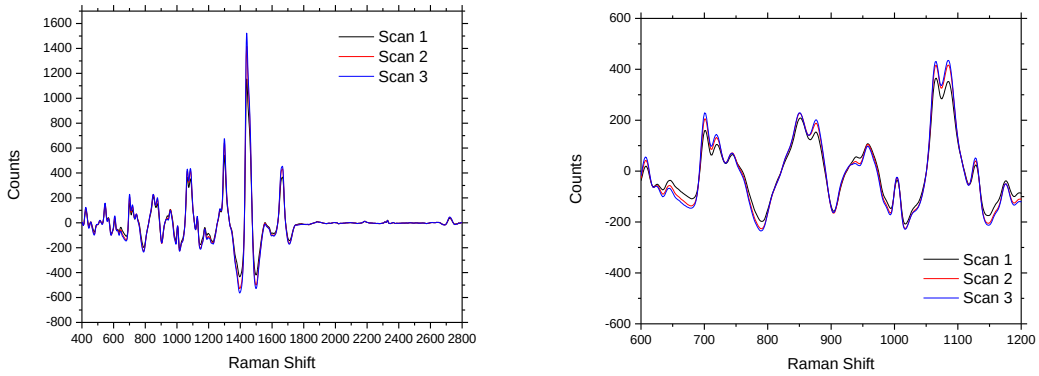

Figure 3.24. Left: Representative spectra of three consecutive scans of pig spinal cord before removal of CSF. Right: zoomed in spectra of the same pig focused on the area used to detect HPO_4 and H_2PO_4

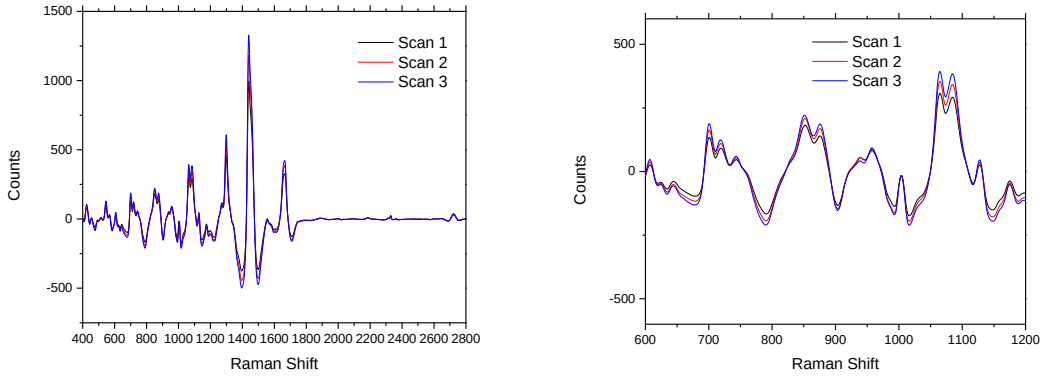

Figure 3.25. Left: Representative spectra of three consecutive scans of pig spinal cord after removal of CSF. Right: zoomed in spectra of the same pig focused on the area used to detect HPO_4 and H_2PO_4

In analogy with the rat data we can take the counts from the 985 cm^{-1} and 1072 cm^{-1} peaks and calculate a pH using the same calibration data and procedure described above. We attempted to validate this approach using the pig model because the pig is large enough that we were able to physically sample[69] the CSF and utilize a (Roche) Cobas b 221 blood gas system to measure the pH of the spinal fluid. The results can be seen below in Table 3.2 along with independent conventional instrument i.e. Cobas b 221 generated values from CSF harvested perimortem.

Table 3.2. pH calculations and comparison for pig spines and instrument

	Calculated pH Before Removal	Calculated pH After removal	Avg Calculated pH offset (0.44)	Cobas b 221 pH	Difference Ave-Cobas
Pig 1	6.55	6.65	7.04	6.93	+0.11
Pig 2	6.60	6.66	7.07	7.07	+0.00

There is a definitive offset between the raw calculated pH and the instrument that is apparently associated with the known artifact described above. This correlates to our data in the rats (which also reflects the standard offset across all data). The initial estimate of the agreement between a physically sampled pH and the Raman based pH is ± 0.06 pH units. We should emphasize that these pig results were obtained using a completely different spectroscopic system employing a completely different excitation wavelength (785 nm) than for the rat model results (830 nm).

There is much to consider in these data and the comments herein should be considered early since we will clearly learn much more about SCI. Nevertheless, this study suggests that including the correction for the spectral overlap artifact, the Raman based pH measurement will be sufficiently accurate and precise useful in many if not all tissues and systems that contain inorganic phosphate, in vitro and in vivo.

3.4 Discussion & Future Work

Raman spectroscopy is a strong analytical tool for examining the highly dynamic nature of living tissue. As mentioned, previous studies have used the technique in many venues. No work has been shown to use Raman spectroscopy to analyze changes of spinal cord injuries *in vivo* however. This study presents a novel application of Raman spectroscopy to measure chemical and physical changes in the spinal cords of rats over time after the effects of a contusion injury to better understand the complex chemistry and physiology of early SCI *in vivo*.

We have learned that NIR probing of spinal cord in vivo is very much like probing other tissues. We were encouraged that surface blood in the surgical field could be washed away significantly well to allow probing of the spinal cord itself without undue heating. As expected, and observed by literally every other example of NIR laser irradiation of biological materials, the decay of the raw IE with increasing laser exposure to any one spot indicates that there is photobleaching of the cord. The behavior and timescale of the autofluorescence when coming to equilibrium with the probing laser is comparable to perfused fingertip skin. Also, collected water on the surface does not seem to alter the Raman spectra or the apparent Hct values calculated using PV[O]H. Since water does not fluoresce or have an appreciable Raman spectrum this is not surprising. Apparently, surgical debris is also not problematic. Perhaps surprising, it is possible to maintain spatial registration to within ± 100μm during multi-hour noncontact experiments while maintaining hydration.

For nearly all manipulations, the control and injury groups had exactly the same physical movements. But some additional motion of the rat was involved in Injury experiments that was not included in the Control experiments. That is, the additional motion of orienting the animal with respect to the impactor and then returning the animal to our motor driven pallet. The only effect on our final quantitative conclusions would involve the coefficient of variation comparison. All other calculations would be unaffected.

Multiple line scans across specific locations along exposed cord of multiple rats, both control and injured give the general phenomenology of PV[O]H based scanning and image formation. Inflammation induced swelling e.g. due to edema at specific locations could occur as an after effect of the contusion injury and this could be manifest both/either as an decrease in apparent Hct, due the accumulation of fluids at the expense of formed components, or due to

change in the surface profile encountered by the probing laser. We can raise but certainly not settle these issues with this study because there any so many chemical and physiological factors involved but we can say that, compared to the timepoint before injury, the location at the injury site shows the greatest amount of statistically significant difference in the injured animals compared to controls. While this result agrees with our initial hypothesis, and seems unsurprising at this point, there were additional observation at both locations surrounding the injury site that warrant further discussion. We will return to this issue after a further summary of observations.

The line scans themselves suggest that such scanning can be used to produce images and can be interpretable in terms of increasing/decreasing fluorescence, changing angle of incidence (surface topology) or combinations of same. Assessing the behavior of autofluorescence in the presence of turbidity in a sensitive reproducible means, in response to various procedures involving SCI or cords in general, is certainly a possibility using the PV[O]H algorithm.

It is imperative to remember that the specific calibration for the PV[O]H algorithm used in this study was based on perfused human skin. Nevertheless, it produced reasonable Hct calculations suggesting that the basic spectroscopic and transport assumptions/requirements for the PV[O]H algorithm to be applicable may be met by spinal cord as well as by skin. More experience with SCI probing in this manner could result in a more specific calibration if other metrics, e.g. MRI imaging revealing water content of cords over the same time period could be used to guide a more specific calibration.

The abrupt but reproducible dips in line scans often observed in line scans e.g. 1000 sec in Figure 3.6 were possibly associated with near surface blood vessels. This hypothesis is supported by the orientation of the dips relative to the scanning, direct visual examination and their reproducibility. Raman spectra were not conclusive either way regarding this hypothesis,

but possibly, they could be dominated by Raman emission from more shallow tissues whereas the images were relying on autofluorescence (a much larger signal) for contrast. The comparison of the *in vivo* collected Raman spectra with those of *ex vivo* tissue and model media lends credence to the notion that there is not substantial penetration *through* even small cords by the probing laser light.

The Raman spectra show substantial systematic changes from beginning to end, even within Control experiments. Thus, surgically exposing the cord itself has consequences that may be evident in the overall observed spectroscopy. While there is much to discuss involving these new data beyond what we will engage in in this thesis, 2 issues warrant immediate speculation.

First, the PCA results for Component 2 across all animals show substantial variation in the 600 cm^{-1} regions. This region has two bicarbonate features and we would expect bicarbonate to be present in >25mM concentration in hypoxic in cerebrospinal fluid. Second, the clear systematic Raman activity in the 900-1100 cm^{-1} region in injured animals, that is statistically significantly different from the uninjured locations, suggests the presence of free inorganic phosphate in CSF in the immediate aftermath of injury.

This could be consistent with the observation of several related features shifting intensity in the both the 2^{nd} and 3^{rd} components. Although there is little protein in CSF, some phosphate production would initially involve available serine and threonine residues, offering different Raman shifts and susceptibility to hydrolysis. In addition, the fact that a single large Raman feature dominates Principal Component 3 over the long term (958 cm^{-1}) suggests there may be a site that may be relatively resistant to hydrolysis or is simply more stable than other sites. If this speculation turns out to be correct, then a treatment for SCI at the earliest stage might include kinase inhibitors and/or phophorylases.

Overall the changes in the spinal cord measured by Raman spectroscopy show similar bands to those previously reported in literature,[9,70] though differences in methods warrant further discussion. A possible result of doing live experiments may be that the laser itself is causing damage to the tissue over time, resulting in the changes seen. Additionally, exposure to an open environment i.e. air and subsequent use of anesthesia may also be affecting results.

There are multiple potential explanations for the systematic variation observed in the Raman spectra and we shall propose one plausible scenario that we currently believe is consistent with all available data. We speculate briefly at this point because we've demonstrated the capability to obtain this kind of data and there are ramifications and inferences concerning the underlying physiology and dominant chemistry of SCI. At the instant of impact, the local cardiac blood pulse and blood pressure will be at some random but homeostatic state, as will the neuron firing patterns of neurological homeostasis. Consistent with our observations in line scans, we assume a contusive injury without breakage of the larger blood vessels but with disruption of some of the smaller vessels.

Since rostral to caudal the CNS is inherently asymmetric, within the milliseconds the electrical connectivity of the brain to the most caudal CNS neurons becomes non-homeostatic. Breakdown of whatever neural electrical firing cycles are in progress when injury occurs would induce mis-correlated chemical responses, that in turn would have propagated in both directions from the point of injury. Because the timescale for diffusive mass transfer is always slower than for correlated electrical field propagation, unusual and probably pathological patterns of neurotransmitter release and uptake in the synaptic cleft might be the first chemical manifestation of the SCI. The normal periodic sequence of polarization-depolarization,

neurotransmitter release-uptake events would be interrupted. Effects distal to the injury site would be expected as the electrical pathology propagates.

Glutamate is the most plentiful amino acid and neurotransmitter in the CSF and so the following discussion also applies to the other neurotransmitters except that the concentrations of the others are lower than glutamate in the spinal cord locale. Normally, during this sequence within the synaptic cleft, glutamate can reach 10 mM for a period of milliseconds before reuptake into the surfaces of the neurons comprising the cleft. During necrosis of neurons e.g. due to ischemia and other physical and chemical insults, glutamate reuptake may be among the first impairments.

If there was impaired reuptake excitotoxicity associated with uncontrolled neuron firing and eventual cell death would likely ensue. Accumulation of excess glutamate in the synaptic cleft would leak into the CSF and the pH of the surrounding fluid would decrease, relative to Control, as the excess glutamate diffuses outward. But we observe statistically significantly higher pH for injured cord than for Control cord and our observed value for Control pH agrees with literature expectation. Note that the other neurotransmitters are either bases or amphoteric and normally exist in lower concentrations in the synaptic cleft so, for this reason we've chosen to focus on glutamate leakage as a primary driver of CSF pH change post injury.

Any changes in local neurotransmitter status occurs in the presence of the slow but steady flow of fresh CSF, rostral to caudal. In particular, the literature value of "normal" pH for CSF reflects the normal leakage of potentially all neurotransmitters into the CSF. On this basis we propose that it may also be possible that if e.g. glutamate release is reduced in the synaptic cleft, less glutamate can leak/diffuse into the CSF, and the pH would increase relative to normal glutamate release. The asymmetric response of the cord pH could reflect the fact that the sheer

number of synapses increases as we examine the spinal cord closer to the brain. The more synapses the greater the amount of neurotransmitter leakage and the greater the effect of impaired release.

This experiment will be powerful in many different realms. Since these surgeons are well equipped with both surgical tools and analytical instruments, we should be able to scan multiples places on the cord multiple times, due to the larger surgical field, and take physical sampling of the spinal fluid. We can then get real time pH measurements as well as a slew of other physiological data, including potentially glucose. To be able to get physical samples and real time data to compare to our calculated data would be a very powerful study and speak to just how sound our calculations are.

A pilot study of this imaging shows there is some promise in using PV[O]H as a viable replacement for *in vivo* imaging of SCI. Preliminary studies show that an increase in apparent Hct for an injury are much more prominent than a healthy cord and furthermore show that the increase is localized around the contusion. The importance of this is twofold, first in location of an injury with minor invasive technique and second the fact the resulting response of the cord after injury is rather rapid in the grand scheme of things. Being able to quickly map and locate an injury could go a long way in prevention of long-term damage created from the formation of a glial scar.

More work is needed in both portions of this study. Mainly the use of *in vivo* spinal cord probing using PV[O]H as an optical profilometry tool. The current study has n=1 which means no statistical workup could be attempted to validate our hypothesis. To that point, the line scan studies were only on a 3 by 3 test scale. These numbers need to be greatly increased to provide a stronger statistical argument that Raman measurements can draw conclusions about spinal cord

injury. We also need to be able to have a comparison to our image studies. Excising the spinal cord after completing our study and taking images of it to compare to our profilometry scan would go a long way and showing the success of our imaging technique.

A greater understanding of the chemical and physical progression of SCI and the timescale at which it occurs would allow for better correlation between line studies and mapping studies. If we can definitely say that chemical processes are occurring at a certain time post injury and that can correlate to a specific image created, that would go a long way in prevention of long-term effects of SCI.

3.5 Conclusions

We set out to utilize Raman spectroscopy, specifically PV[O]H, as a clinical tool for assessing and understanding the chemical processes of spinal cord injury. While conducting line scans of the cords we were able to attain Raman spectra indicative of chemical responses to the injury as well as phosphate changes that were statistically significantly different between injured cords and control cords. We were able to identify peaks corresponding to inorganic phosphate in these spectra and extrapolated early pH change calculations from this data. The line scans also showed this process could be used as a method of optical profilometry of cords. The pH of CSF for injured rat spinal cords fluctuates more in the first three hours after injury relative to Controls ($p<0.0001$, $N=81$). The actual pH at the location of injury and at a location immediate rostral are different ($N=27$, $p<0.064$ and $p<0.001$) for Controls and Injured animals. It is possible to measure pH in many aqueous systems containing inorganic phosphate label-free, noninvasively using Raman spectroscopy and without physical sampling of materials.

Chapter 4: Non-Invasive Spectroscopic Measurements of Cell Viability and Study of Metabolic Activity in Tissue Culture of Mammalian Cells

4.1 Introduction

The purpose of this research is to track the viability of a cell culture through all stages of growth and propagation, without risking outside contamination or introducing outside chemicals that can damage the cells and/or itself affect the culture's viability.[20] We use Raman Spectroscopy to non-invasively track metabolic activity and cell growth without physically disturbing the cell culture. We stipulate that since cells evolved to exist in a solar lit environment, their "native" environment is illuminated at reasonable solar-like irradiances. With this definition we can assume the effect of the light to conduct the spectroscopy to be very small but still possibly discernable from the same cells living in a dark environment.

As a prelude to testing live cultures we invasively analyze nutrient depletion and waste production in "cultured medium" (CM) that was sampled from a culture, spun down and analyzed by Raman, in comparison with a "neat medium" (NM) which has not maintained a culture. If the spectroscopy of these physically sampled cultures is not sufficiently revealing, then it will not be possible *in vivo* i.e. in culture flasks. In that connection, we will also study the problem of overcoming the background fluorescence and Raman spectral features associated with the culture flasks that are used to house the cells.

4.2 Experimental

4.2.1 Culture Selection

Medium samples were supplied for sampling from the Hougland Lab in the Chemistry Department. Medium was made of a combination of Dubelco's Modification of Eagle's Medium and is a 10% (v/v) Fetal Bovine Serum (FBS) and 1% Penicillin/Streptomycin solution. The cell line was the NIH3T3 mouse fibroblast cell line. It should be noted for analysis that the medium contained 4.5 g/L (2.5 mM) glucose in the medium as a food/carbon source.

Two separate samples of medium where supplied for analysis. The first was a blank medium with no cells present that could be used as a reference. This was referred to as neat medium (NM). The second samples supplied contained cells and are referred to as cultured medium (CM). NM was treated just as the cells were i.e. kept in the same environment, and sampling occurred from the same style batches at the same time. CM contained cells that were removed by centrifugation before being tested. This sample had a Raman spectrum run on it. It was removed and then filtered with Whatman© 0.2µm Inorganic Membrane filters. This Sample was then run again in the Raman spectrometer.

The experiment was first run over the course of four days with one collection each day. When it was found that more data points were needed to perform certain analytical practices (see results), the same experiment was run, over another four days, but collection was taken three times each day, with two collections occurring on the final day to give a total of eleven samples over the course of 99 hours. It should be noted that the doubling time of the NIH3T3 cells is roughly 1 day.

4.2.2 Culture Flask Study

Once determined that running the medium studies alone was a success it was decided that *in vivo* studies on the cells would be attempted. First the issue of penetrating the polystyrene culture flask without losing signal was an issue. Numerous tests were done to determine if it would be possible to overcome this issue. Manipulation of the polystyrene flasks by heat, dissolving, and machining all proved to be unsuccessful.

In order to assess the gross background produced by the spectrum of the culture flasks 8, 50 mL vent cap, tissue culture flasks (Jet Biofil©) were obtained from the Hougland lab. Each flask, while still empty was placed in such a way that the 830 nm laser would focus where liquid would be, had there been some present (roughly 25 mL). The holder was set up in such a way that the laser would hit the same spot on each flask hopefully minimizing variation between flasks. Each flask was placed in the holder and run on the spectrometer (described below). Also, 1 flask was then placed in the holder 5 separate times i.e. removed and replaced between taking 5 consecutive spectra to see the effect of simply removing the flask.

Once determined that the polystyrene peaks could be removed, different dilutions of glucose, ranging first from 1M down to 10 mM and then from 100 mM down to 10 mM with a more precise dilution were made and run.

4.2.3 *In vitro* study

Upon determining that the signal from the medium could be interpreted through a flask, without removing the flask signal from the spectrum, the same study was done as above. Six flasks were set up, three with live cells, and three that were just medium, in line to determine changes over another four-day period. Each flask was scanned three times a day, morning, mid-day and afternoon, for the four-day period, again roughly a 99-hour experiment. An apparatus was assembled to ensure that the same spot on each flask was used for each scan. The probe for the spectrometer was pressed up next to the flask making contact but not pressing too hard to ensure the flask top stayed flat. A stage micrometer was implemented to ensure uniform focal length across each flask. The samples were stored in an oven to ensure proper cell growth while not being scanned.

4.2.4 Raman Spectroscopy Set-up

An 830 nm spectroscopic measurement was employed using a modified Raman spectrometer. (Lambda Solutions, Waltham, MA). There was an additional notch filter (Semrock, Rochester, NY) placed between the collimating lens and grating to allow for adjustment of both the IE and EE to find an optimal dynamic range. Spectrum collection time was 200 seconds, giving ten thousand accumulations of 20 msec frames. The laser power was set in the system to 0.9 Volts corresponding to 225mW CW. The CCD was cooled to -15°C and signal was collected as 100% backscattered light from the source. Dark current spectra were run prior to each session and subtracted from all spectra to ensure no discrepancy due to CCD drift.

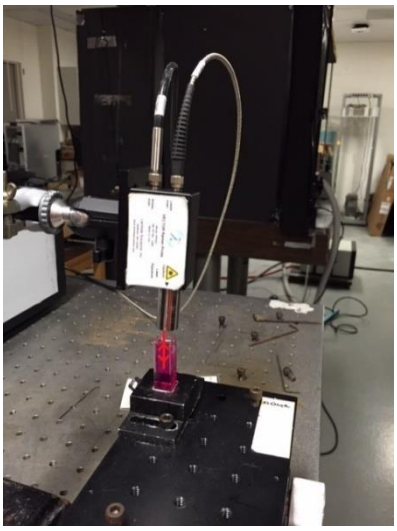

Figure 4.1. Schematic diagram for the 830 nm Raman Spectrometer (Lambda Solutions). The silver fiber bundle is the laser and the black cable is the detector port.

Data analysis was carried out in Microsoft Excel and Origin 9.1. Raw spectra were cropped to the range of roughly 300 $cm^{-1}$to 2450 $cm^{-1}$and a "101-7" arbitrary baseline subtraction was applied to accentuate Raman features from the raw spectra. To execute a 101-7 baseline subtraction a 101-point adjacent average of the raw cropped spectrum is produced in Origin and subtracted from the raw spectrum. Lastly, a 7-point adjacent average smooth of this difference is carried out to reduce out the high frequency noise.[43]

4.3 Results

4.3.1 Medium Testing

Prior to any testing for viability being done, a pre-culturing (NM) and post culturing (CM), after four days were done to see if any differences could be seen. After applying the 101-7 baseline correction it can be seen that in fact there is a difference between NM and CM.

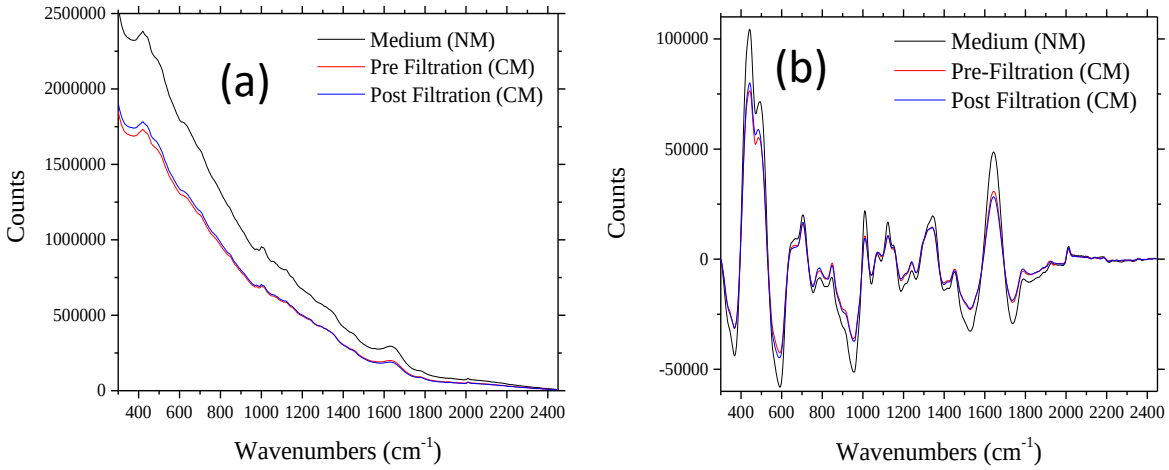

Figure 4.2. (a) Raw spectra of the NM as well as the CM both pre and post filtration. (b) 101-7 baseline corrected spectra of (a).

Filtration of the CM was done to ensure all cells and cell remains had been removed. As seen in the Figure below there is not a large difference in pre and post filtered medium.

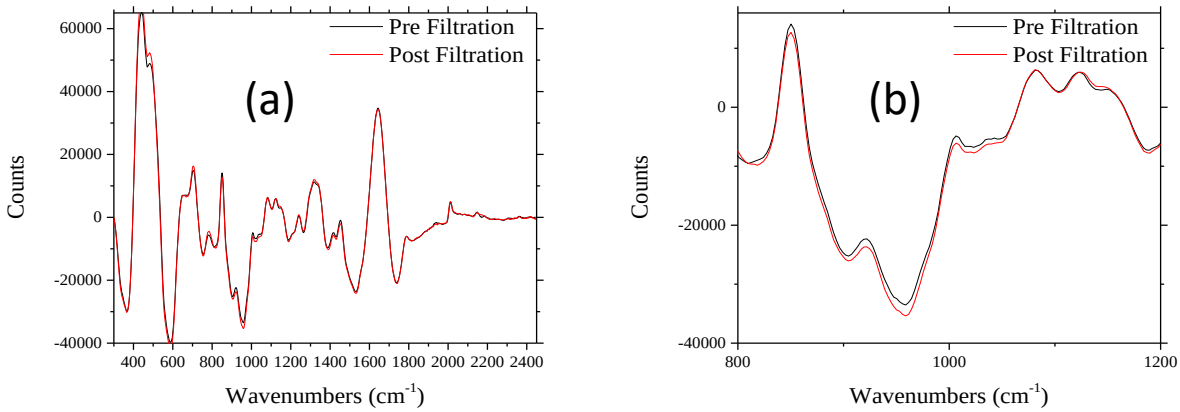

Figure 4.3. (a) Comparison of pre-filtration and post-filtration of CM. Used to show that filtering seemed to not have an overall effect on the spectrum of the CM. (b) Close up of region from roughly 800 to 1200 cm^{-1} showing slight but inconsistent changes.

A day by day comparison was done for NM and CM that had been used to culture NIH3T3 mouse fibroblast cells. The NM was treated like that of CM except no cells had ever been present in the NM. Cells were cultured for a period of four days with a collection of NM and CM each day at approximately the same time. There would appear to be systematic changes occurring in

various locations on the spectrum. The increasing peak heights correlate to chemical production by the cells and the decreasing peak heights correlate to chemical consumption by the cells.

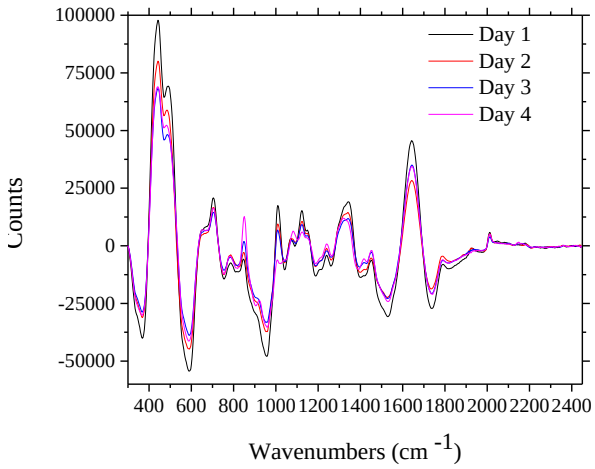

Figure 4.4. Comparison of 4 days of CM.

Taking note in the Figure above there are several spots that have decreasing peaks. Some of the most obvious are at 442,490, 1123, 1150 and 1344 cm^{-1}. From past work done in our lab, and as shown by the spectrum below we can associate all of these peaks to glucose.[71] This makes sense as it is well known that mammalian cells require glucose as a source of carbon and so is included in many media.[71]

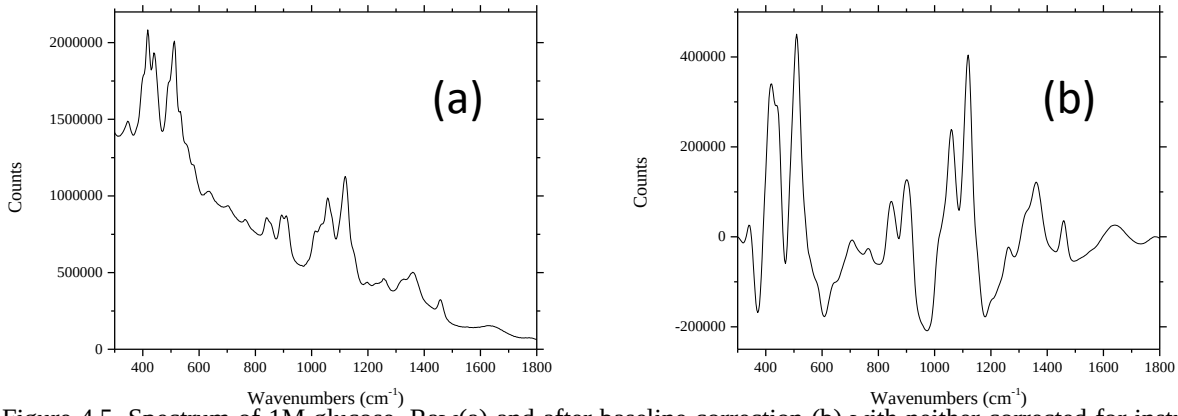

Figure 4.5. Spectrum of 1M glucose, Raw(a) and after baseline correction (b) with neither corrected for instrument response function.

The 1344 cm^{-1} peak is of certain interest to us. As can be seen, the rest of the glucose peaks are decreasing from day to day continuously whereas this peak seems to essentially be the same for days 3 and 4. This could in fact be due to one of two things. The first is that the cells stopped ingesting whatever is present that causes that peak after day 3 in the culture. If this were so, then the rest of the glucose peaks, we would assume, would also level off. It is much more likely that in fact this peak is two separate components, one growing or being produced, and the other being depleted at the same time. If this is so it can be assumed that these components would be roughly around the same quantity during the period of days three and four.

More to the point on the 1344 cm^{-1} peak is the 1670 cm^{-1} peak. This peak also appears to be decreasing over the four-day span. Water produces a broad peak at roughly 1650 cm^{-1} which can be seen very strongly in both raw and baseline corrected spectra. It makes sense that water is decreasing from day to day due to an increase in the concentration of all other species, and the volume they occupy in the culture. As they increase, the volume percent of water, even in filtered medium, is decreasing.

Another common species that shows up in biochemical Raman spectra at around 1650 cm^{-1} is protein[8], more specifically the "amide I" i.e. the CH stretching vibration localized on the amide linkages of the protein. Most protein in the medium can be expected to contribute to this feature so generic "protein" could be accumulating or could be depleting depending on many different factors in the course of a specific culture. It should be noted that there are other peaks that are systematically decreasing but cannot be completely assigned at this time.

Next, we observe peaks that increase during the monitoring period such as the peak at 850 cm^{-1}. Original thought process through collaboration with the Hougland lab lead us to believe that the peak could be related to the glycosidic linkage at the anomeric carbon.[71] According to the literature[72] this peak could be an indication of glycosylation production. Glycosylation is the enzyme catalyzed addition of short chains of carbohydrates covalently bonded to the peptide side chains of a protein. This process is of importance to the biomedical world, more specifically biopharmaceuticals as glycosylation has a great impact on pharmacokinetics.[43]

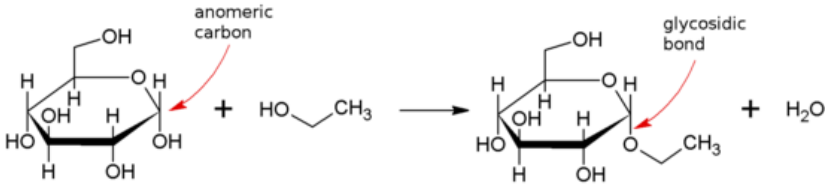

Figure 4.6. Formation of ethyl glucoside from linkage of ethanol and glucose

Through later research[73,74] we believe that the peak could also resemble a part of the extracellular matrix (ECM) produced by the cells. This is also feasible as it is another component that most cells excrete from their systems into their environment as a way of life. ECM has many Raman peaks but the 850 cm^{-1} peak could be from tyrosine in it. Previous research[73] states that tyrosine does exhibit a doublet at 834 cm^{-1} as well at 850 cm^{-1} but due to our resolution we may

not see that peak. If that's the case then this peak could very well be from tyrosine, which is found in some forms of mammalian cell ECM.[74]

Once the preliminary data was analyzed, a principal component analysis was performed on the spectra. Principal component analysis (PCA)[75] is a chemometric/statistical technique that reduces a multi-component system, for instance our spectra, into the smallest number of linearly independent, statistically significant components so as to analyze the variation of said components over time. We took our four-day sample set and presented it to Dr. Goodisman to put through a PCA program he had developed which generated the data in Figure 4.7.

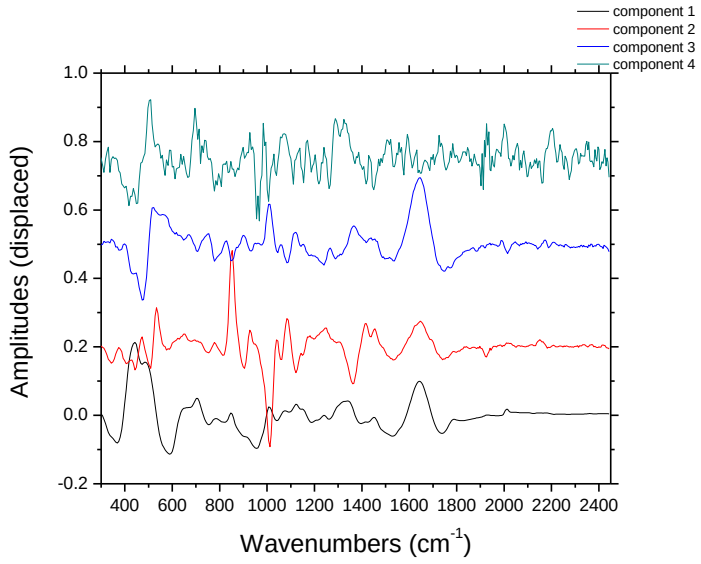

Figure 4.7. Principal component analysis of the four-day sample set of CM (Figure 2.4). Component 1 is black, component 2 is red, component 3 is blue and component 4 is green. We believe component 1 (black) is glucose and component 2 (red) is our glycosylation peak or ECM. Note that for computational expedience Goodisman used PCA on a subset of the data points and the spectral resolution of his "components" is therefore reduced relative to the original spectra.

From the PCA above, it was determined that component 1 (black) and component 2 (red), showed the most promising results. It would appear from the spectra that component one is glucose when compared to the spectra above (Figure 4.5). The data from the four-day study PCA was graphed as an intensity of the glucose peak (component one). As can be seen from Figure 4.8, it decreases from day to day. This is indicative of glucose consumption which proves promising results that we can see metabolic activity in medium as we know glucose is used as a main source of nutrition for cells. Figure 4.8 also shows an overlay of PCA 1 and a standard spectrum of 1M glucose. As can be seen the peaks match up almost perfectly. The discrepancies can be accounted for due to the resolution of the PCA vs. that of the spectrograph. The PCA is 416 points over 2150 cm^{-1} (roughly a point every 5 cm^{-1}) whereas the spectrograph is 832 points over that span (or roughly a point every 2.5 cm^{-1}). The increased resolution causes for the definition between peaks that cannot be seen with the PCA as well.

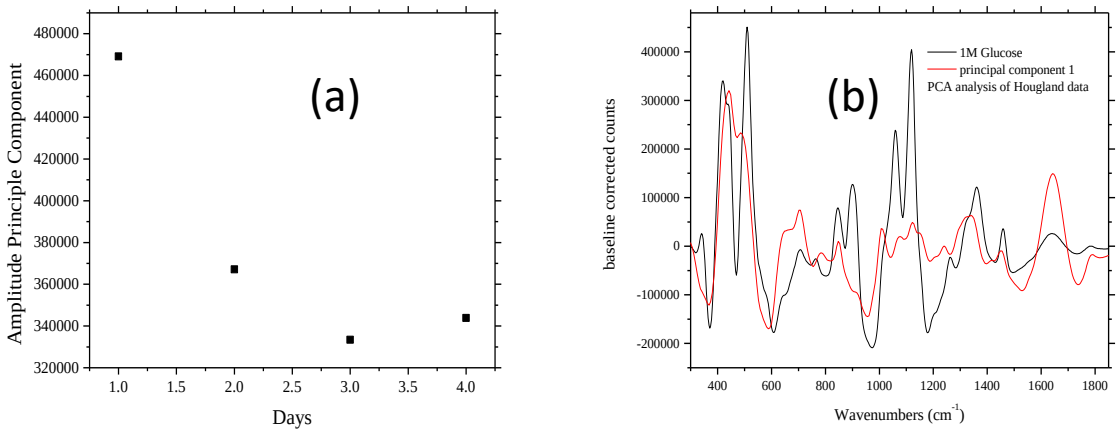

Figure 4.8. Graph of intensity of component one over the course of the four-day period(a). (b) PCA of component 1 (red) superimposed over the spectrum of 1M glucose (black).

From the PCA data it would also appear that component 2 is related to the 850 cm^{-1} peak. Whether that peak would be a glycosylation peak or ECM it is quite apparent from Figure 4.9 that it is increasing over the four-day study. This is very promising in taking steps toward showing that in medium studies, glycosylation production or ECM production can be used as a measure of metabolic, i.e. anabolic activity, in these cells. It should again be noted that since there was data from four days (four data sets) that four components could be extracted, though due to the low number of data sets, components 3 and 4 come out with too much noise to make a viable comparison.

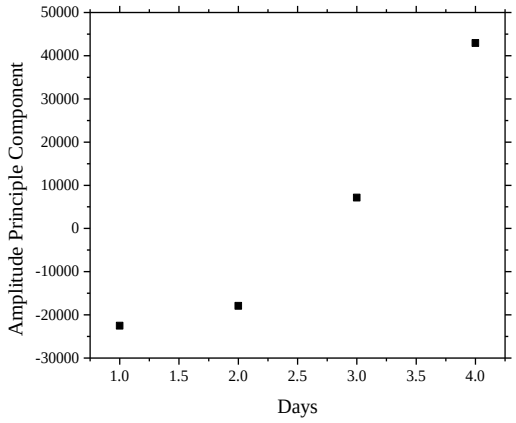

Figure 4.9. Graph of intensity of component one over the course of the four-day period. We believe this component to be the glycosylated protein (our 850 cm^{-1} peak) or possible ECM.

To get more accurate, and frankly more components in general, the testing of medium was extended to taking three reading of NM and CM a day over the four-day grow period, 99 hours. Results can be seen below in Figure 4.10.

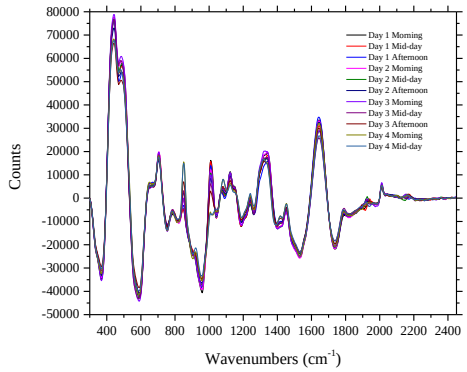

Figure 4.10. Comparison of 4 days of CM, with 3 data points taken each day, 2 on the final day, giving 11 separate spectra.

It can be seen in these comparison spectra that the same behavior in the presumed glucose and glycosylation/ECM peaks are observed. This data further supports the hypothesis of glucose consumption and glycosylation/ECM production. Below can be seen an enlargement of these regions to further show the change (Figure 4.11).

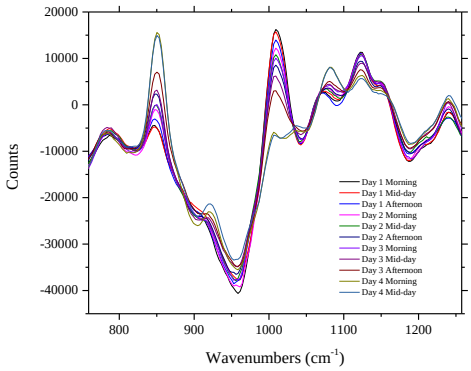

Figure 4.11. Enlarged section of Figure 2.10 showing an increase in the glycosylation, ECM peak (850 cm^{-1}) and a decrease in glucose (roughly 1000 cm^{-1} and 1100 cm^{-1})

Using the Origin 9.1 data analysis program, peak heights were determined for the 850 cm^{-1} peak and the 1123 cm^{-1} peak which could be a glucose peak.[71] As shown below in Figure 4.12, the graphs again show an overall decrease for the glucose and an increase for the 850 cm^{-1}peak. The data was broken up into days due to the fact that NIH3T3 cells have a doubling time of roughly 20 hours.[76] Assuming that the cell number density doubled in a roughly 24-hour time span, and

that their per cell metabolic activity, i.e. catabolism and anabolism rates is not a function of the number density, the slopes of their production and consumption would double in that same roughly 24-hour time period.

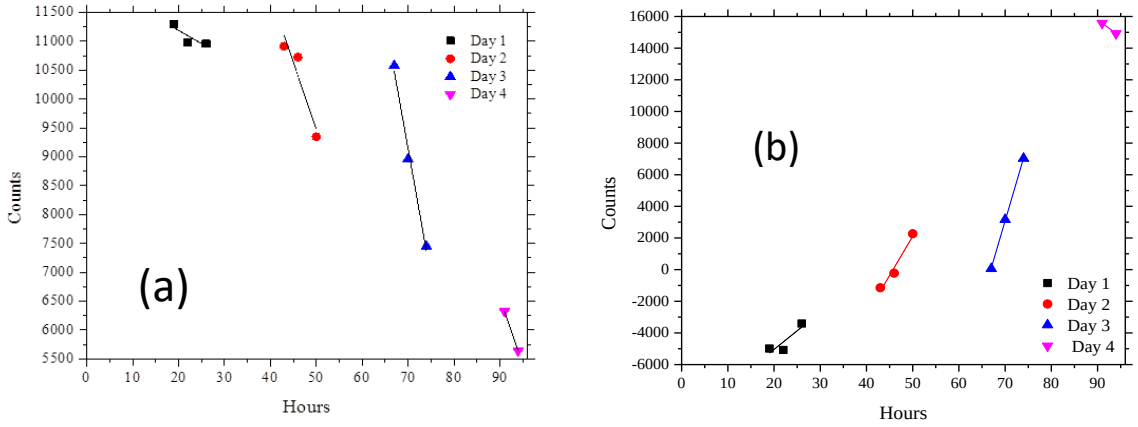

Figure 4.12. Count of 101-7 data of (a) peak 1123 cm^{-1} and (b) 850 cm^{-1}

The slopes for days 1 through 3 (day four only had 2 data points and thus the slope was omitted) of component 1 were roughly -45, -230, and -455 counts/hour respectively. For component 2, the slopes, again only for days 1 through 3, were 235, 495, and 993 counts/hour respectively. Using the Q-test[68] and N=4, we can exclude the earliest point for component 1 at 99% confidence and so averaging the remaining daily ratios for both components resulted in 2.03±0.08 (±2σ). Thus the roughly 24 hours doubling time is verified at 95% confidence.

PCA was then performed again on this larger data set. Again it was seen that component one (the most abundant) was glucose and component 2 was our 850 cm^{-1} peak. Below the results can be seen in Figure 4.13. The same pattern was seen as in the previous peak height graphs so again day to day slopes were evaluated. Component 1 slopes were -1603, -2640, and -5813 counts/hour respectively. For component 2 the slopes were 286, 1011, and 2275 counts/hour respectively. This data correlates to Figure 4.12 and thus we believe it to be real and indicative of

doubling times. In this case no data can be excluded and the average daily ratio was 2.4±0.8 (±2σ) also verifying the expected roughly 24-hour doubling time for NIH3T3 cells at 95% confidence.

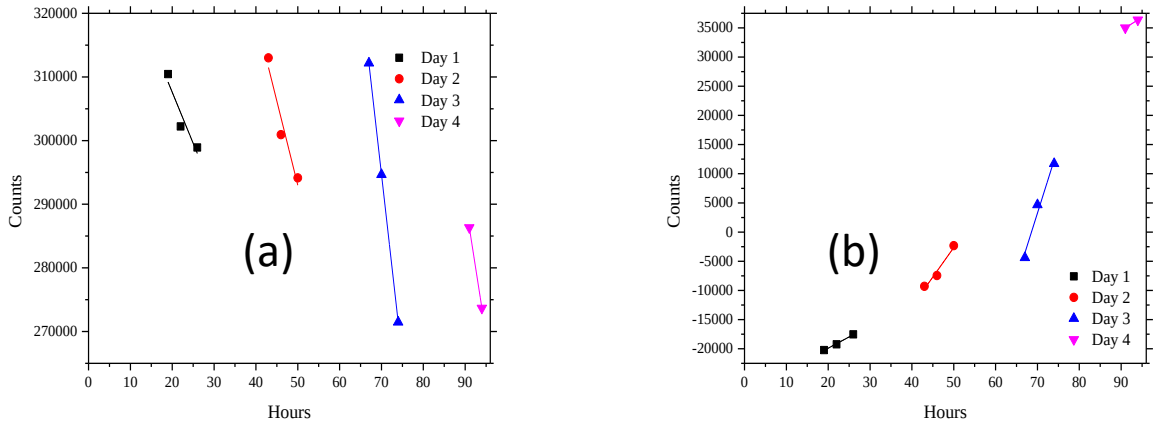

Figure 4.13. PCA of component one (glucose) and component two (850 cm^{-1} peak) over the four-day study.

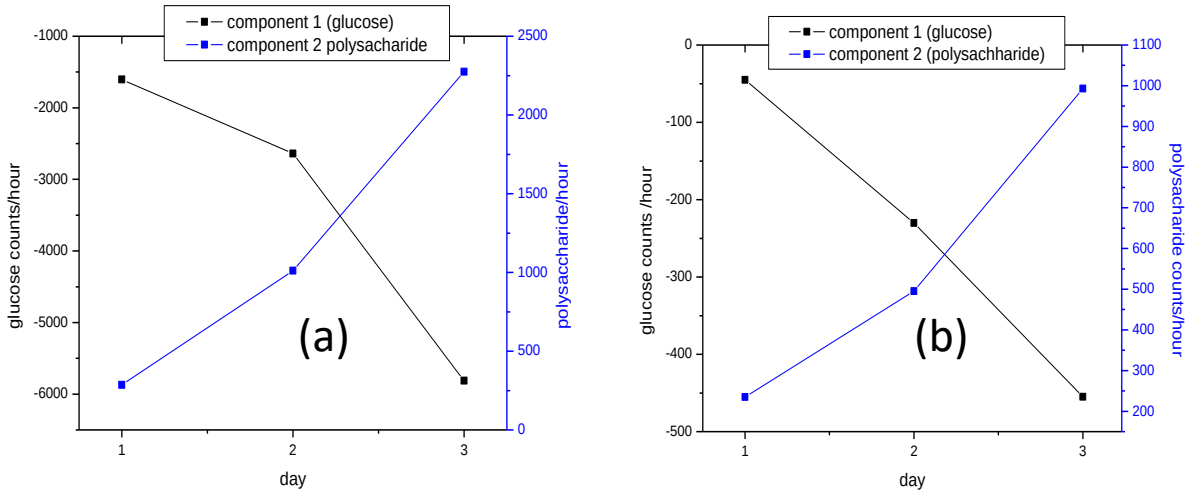

Figure 4.14. (a) depiction of counts per hour of glucose (black) and polysaccharide (blue) over the three-day study from first trial PCA. (b) the same as (a) for the second PCA run with more sample points. Both are accurate depictions of glucose uptake (decreasing slope) at roughly the same interval of polysaccharide production.

4.3.2 Culture Flask Testing

Since it was determined that from the medium of mammalian cells we can determine metabolic activity and viability, the next hurdle is to test these cultures *in vivo* with the actual cells still intact and without disrupting the cultures. To do this we first need to determine if we can take spectra of something inside a culture flask. To do this, first 8 separate flasks were tested with the laser focal point set to where the culture would fill the flask. As can be seen in Figure 4.15 there is an over powering peak right at roughly 1000 cm^{-1}. The goal is to determine if this peak can be precisely and accurately subtracted from raw spectra to see the Raman features of the solution inside the flask.

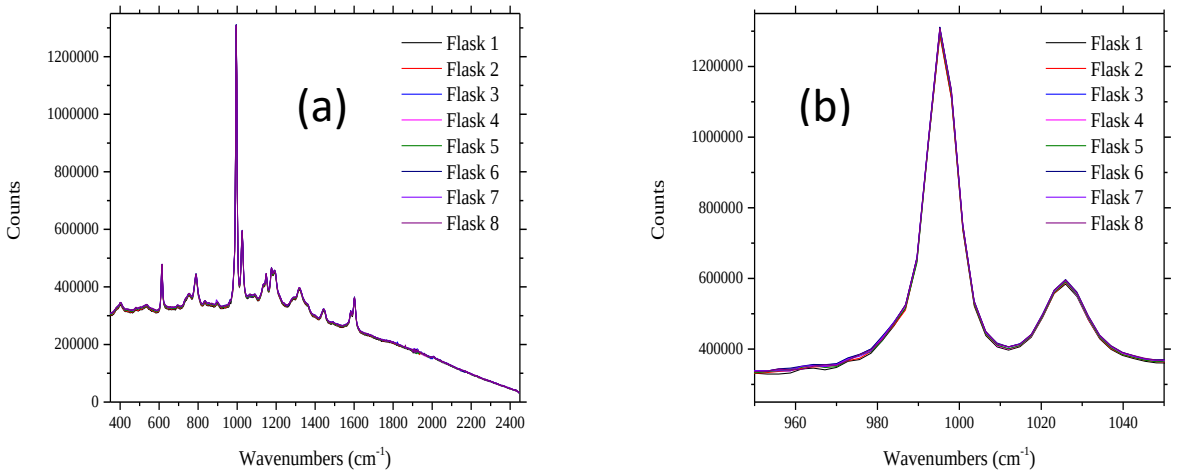

Figure 4.15. 8 different flasks placed in the same spot (a). An enlargement of the prominent peak at roughly 995 cm^{-1} (b)

Through the testing of multiple different flasks, and the same flask being displaced and then placed back in the same location it was determined that subtraction of the peaks could be done if the same flask was used and was placed in the same place.

Table 4.1: Average Peak Height, Standard Deviation, and Standard Error for Flask Evaluation.

		614 cm^{-1}	995 cm^{-1}	1602 cm^{-1}		614 cm^{-1}	995 cm^{-1}	1602 cm^{-1}
Avg.	8 Flasks	475019.1	1302765	362222.8	1 Flask 5 Times	521412.8	1447838	406989.2
St.Dev.		4005.42	8852.30	2696.33		1892.931	4742.69	1429.63
SEM		1416.13	3129.76	953.30		846.5446	2121.00	639.35

The table above shows that even though both the standard deviation and standard error seem high, as high as 3100 counts, that is still less than 1% of the mean counts in many cases, around 0.2% for the 8 different flasks and 0.1% for 1 flask 5 times. This suggests we could subtract the empty flask spectrum from that of one filled with medium and quantitatively monitor e.g. glucose consumption using Raman features.

We used a standard solution with well-defined Raman peaks relevant to the cultures to observe how well peaks can be measured after subtraction. 1 Molar glucose was first used to see if it was possible to see glucose at all. Serial dilutions were then carried out down to 10 mM and then in a smaller spread, from 100 mM to 10 mM. Figure 2.16 shows that the container has a well-defined Raman spectrum with a dominating peak at roughly 1000 cm^{-1}. There are however peaks at roughly 440 and 490 cm^{-1}that can be used to determine the glucose concentration in aqueous solution after subtracting the flask Raman spectrum.

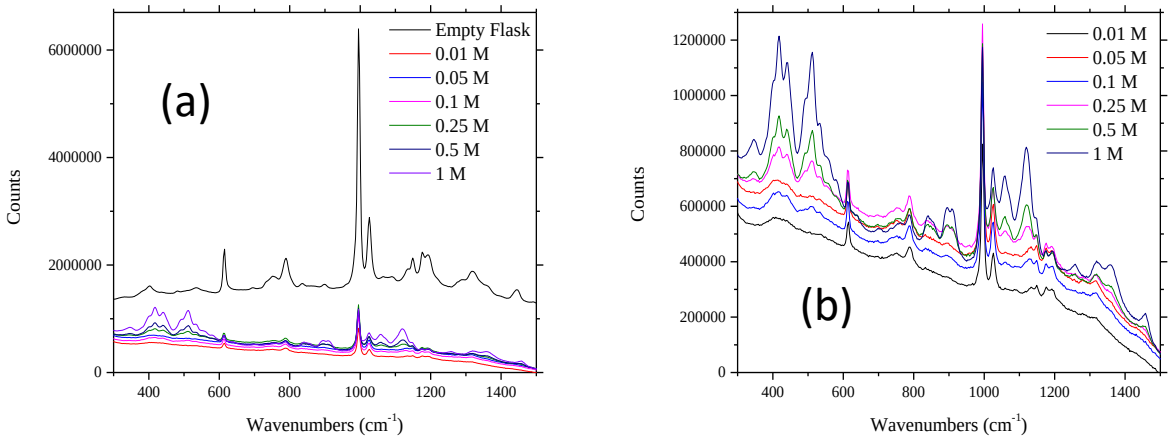

Figure 4.16. Glucose in solution in culture flask, along with the empty flask for comparison (a). An enlargement of a(b). Glucose ranges from 1 M to 10 mM.

We integrate over a specified area (365-575 cm^{-1}) for each spectrum of glucose. The integrated counts of this were then graphed against the concentration and a line of best fit was made (Figure 4.17). It should be noted that before the integration was done, the baseline was adjusted using a machine implementable algorithm[77] to get an accurate measurement of counts. The R-squared value of the original plot was 0.996. This is slightly skewed though since there is such a large gap from 0.25 M to 0.5 M and 1M glucose. When the two high points are not included, the R-squared value does drop to 0.97 but that is still remarkably high giving promise that glucose concentration could be determined from a set integration in the spectra.

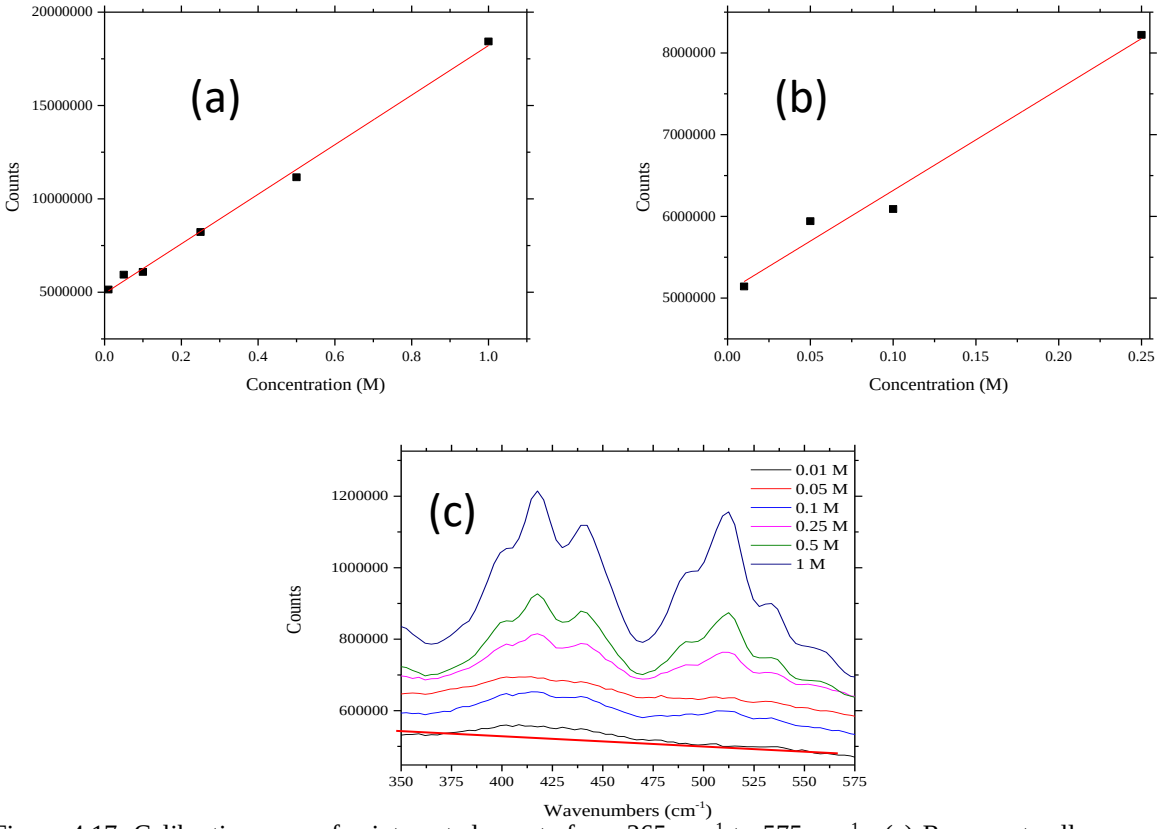

Figure 4.17. Calibration curve for integrated counts from 365 cm^{-1} to 575 cm^{-1}. (a) Represents all concentrations tested and gives a line of best fit as y=1.33E7(x) + 4.94E6 with an R^2= 0.996. The error on the slope is 362529 counts/M and the error on the intercept is 170369 counts. (b) Represents the same data set but only the low end and gives a line of best fit of y=1.24E7(x) + 5.08E6 with R^2= 0.97. The error on the slope is 1329880 counts and the error on the intercept is 182222 counts/M (c) expanded scale for section of glucose spectrum used for calibration curve. The baseline used for integration of the 10 mM spectrum depicted as the straight red line at the bottom of the spectra.

We extrapolate these results below to suggest the measurement timescale and other conditions that will be needed to allow direct measurement of glucose in the range of concentrations that are typical in commercial culture media. Glucose or another carbon source is needed in all chemically defined media and so it is the single most important substance to monitor to assess the viability and activities of a culture.

We now have an accurate accounting of both Raman counts per hour of glucose consumed (from Figure 4.13) from the PCA and another accounting for Raman counts/concentration of glucose (Figure 4.17). We can use the slopes of each graph to get an accurate measure of glucose consumption per hour.

To gain a rate of consumption we observe the units in the slope.

$$\frac{Counts}{Hour} \times \frac{Counts}{mM}$$

To cancel counts we need to invert the second slope giving:

$$\frac{\cancel{Counts}}{Hour} \times \frac{mM}{\cancel{Counts}}$$

After calculation we get 0.121 mM/hr, 0.198 mM/hr, and 0.437 mM/hour glucose consumption for each day respectively, which converts into 3.36×10^{-5} mM/sec, 5.50×10^{-5} mM/sec, and 1.21×10^{-4} mM/sec respectively. Our goal is to determine if it is feasible that this much glucose is being consumed by the number of cells present. To do this we will need to calculate the rate in terms of molecules of glucose consumed per second per cell in culture.

.

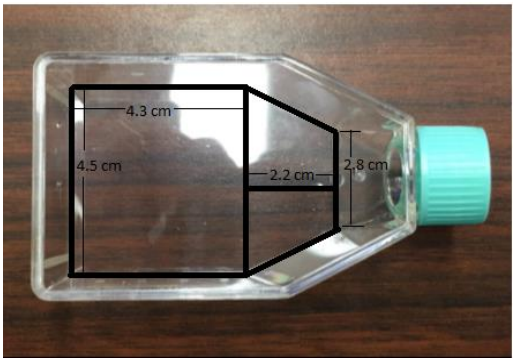

Figure 4.18. Measurements of culture flask used to grow cells. Area of the face of the flask= area of rectangle measurement + area of trapezoid measurements= 27.16 cm^2

Above in Figure 4.18 we can see the dimensions of the flask used to culture these cells. We know[75] that the cells plate at roughly 10^4 cells/cm^2. These measurements yield an area of 27.16 cm^2. This would mean that on days 1, 2 and 3 of cell culture, there are presumably 2.7 x 10^5 cells, 5.4 x 10^5 cells, and 1.1 x 10^6 cells respectively. We also need to know the presumed volume of medium that would be in this flask. If the medium measured roughly 1 cm high, we can assume the volume to be 27.16 cm^3. With these and the values for glucose consumption rate that we have calculated we can combine them to determine an average number of glucose molecules that each cell consumes from the following equation:

$$\frac{dM}{dt} = N_{cells} \times R_m \times \frac{sec}{hr} \times \frac{1}{N_A} \times \frac{1}{V_c}$$

Where dM/dt is the change in concentration (M) per unit time (hours), N_{cells} is the number of cells at the given time, R_m is the rate of consumption (molecules/sec), N_a is Avogadro's number per second, and V_c is the volume of the culture, 27.16 cm^3 in our case. If we rearrange the equation, we can solve for R_m.

$$R_m = \frac{dM}{dt} \times N_a \times V_c \times \frac{hr}{sec} \times \frac{1}{N_{cells}}$$

We calculate that the average glucose consumption comes out to $7.23 \times 10^{10} \pm 3.29 \times 10^{10}$ molecules/sec per cell. The relatively high uncertainty (roughly 45%) could be due to the fact that we have taken these calculations over a 3-day span and assumed the cells were behaving the same way the whole time. The cells could be in different stages of growth during each time point which could cause them to consume glucose at a different rate. Previous research[78] done has also attempted to calculate this rate. They were able to show that the rate varies greatly, based on separate 24-hour periods, upwards of 50% difference. Since our number is an average over a great span of time it is feasible that this is the cause for a higher uncertainty. This means that for this to be possible there needs to be more than 10^{10} molecules that the cells have access to.

To show this we can calculate profiles estimating the rate at which glucose molecules strike the flat side of one cell. We assume that 1/6 the molecules within 1 mean free path of the surface jump to the surface, and multiply this number by the number of jumps per second to get the rate at which molecules reach the surface. The factor of 1/6 comes because there are 6 possible directions a glucose molecule can jump, only one of which is favorable. This is made possible by the Einstein-Smoluchowski equation which relates diffusion coefficients to the parameters used in the formulations of a random walk model.[79]

$$Diffusion\ Constant\ (D) = \frac{\lambda^2}{2\tau}$$

where τ is the average time between jumps. Also, the mean free path λ for glucose in water[24] is 2.5×10^{-8}cm. Then $\tau = 4.66 \times 10^{-11}$s. The rate at which glucose molecules in solution reach the surface is therefore:

$$\frac{(2.5 \times 10^{-6}) \times (6.022 \times 10^{23})(\frac{2.5 \times 10^{-8}}{6})}{4.66 \times 10^{-11}} = 1.35 \times 10^{20} cm^{-2} s^{-1}$$

Assuming the cell cross-sectional area is $1\mu^2 = 10^{-12}m^2$, the number hitting a cell cross-section is $1.35x10^{12}$ per second. This value is quite high and means that while the cell is consuming roughly 10^{10} molecules/sec, there are ample molecules around for it to choose from.

4.3.3 *In Vitro* studies

After showing that flask measurements can be replicated, a full *in vitro* experiment was attempted. Below you can see the baseline corrected results for that experiment.

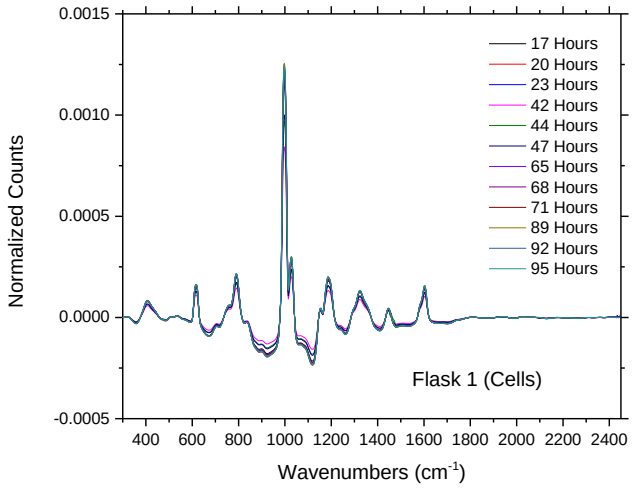

Figure 4.19. Example 101-7 baseline corrected spectra of flask containing cells for whole 95-hour experimentation. Note the overpowering peak at roughly 1000 cm^{-1} indicative of polystyrene case.

Through closer examination the first peaks we attempted to use for glucose consumption were some well known glucose peaks (mentioned above), 570 cm^{-1} and 1120 cm^{-1}.

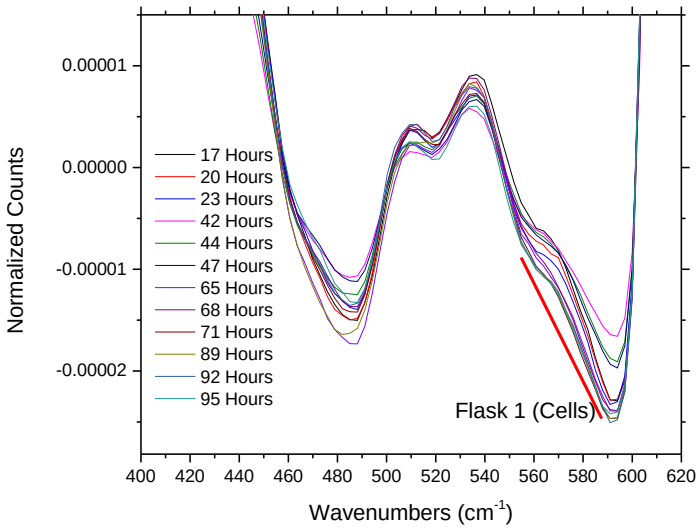

Figure 4.20. Zoomed in version of the 570 cm^{-1} region of a flask containing cells.

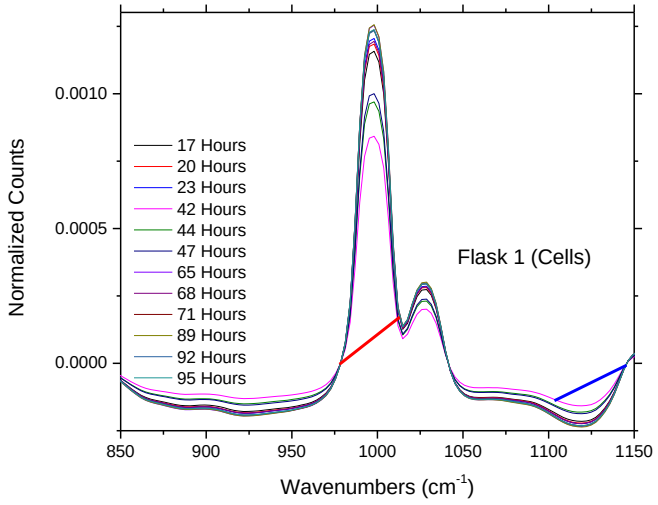

Figure 4.21. Zoomed in version of both the 1000 cm^{-1} (polystyrene) and 1120 cm^{-1} region of the flask containing cells.

Upon closer analysis at each of the peak areas we can see (as we would assume) a general decrease in signal for both glucose peaks over time. This however is not entirely conclusive as, especially during day two of the experiment, it would appear that there is a discrepancy in the data.

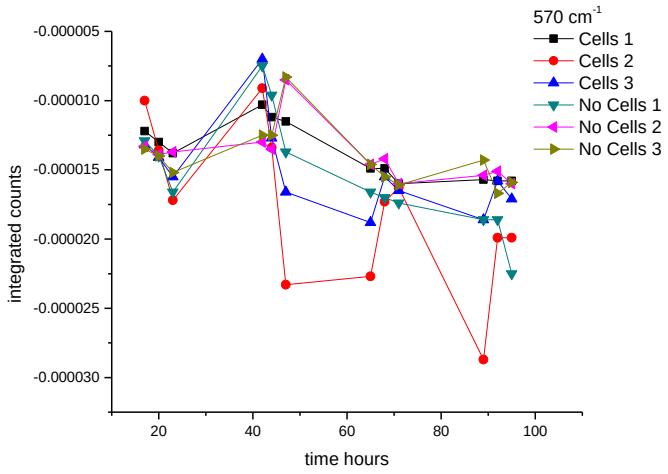

Figure 4.22. Integrated counts at 570 cm^{-1} for each flask over the entire study.

We took it one step further and compared simply one flask with cells to one flask without cells. Again, there is some difference between the two flasks but any data is skewed with the event occurring during day 2.

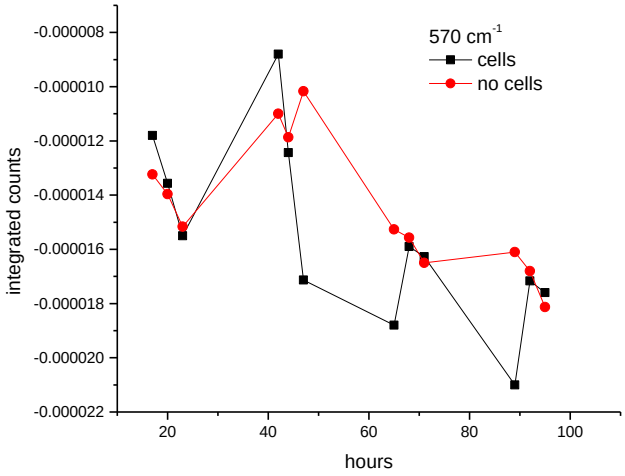

Figure 4.23. Comparison of integrated counts at 570 cm^{-1} one flask containing cells to one flask not containing cells and one containing them.

Further examination of all spectra collected over the study on one collective graph further depict (figure 4.24 below) that there was a definitive problem occurring in the second day. If we just arbitrarily remove that day (figure 4.25) the best fit line of the data, still with a negative slope, retains a much greater R^2 value.

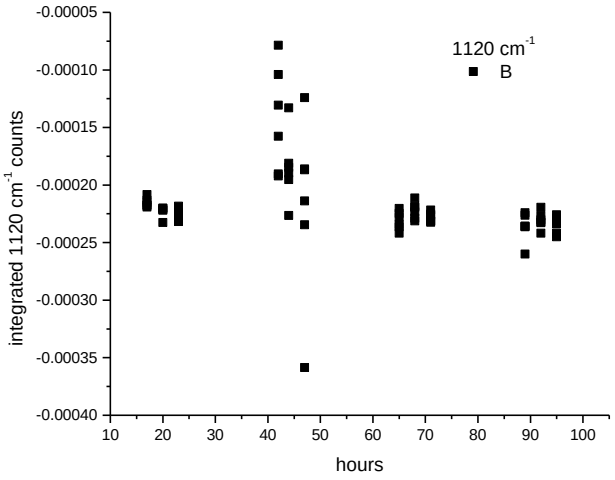

Figure 4.24. Collective data of every flask at every timepoint at 1120 cm^{-1} over entire 95-hour study.

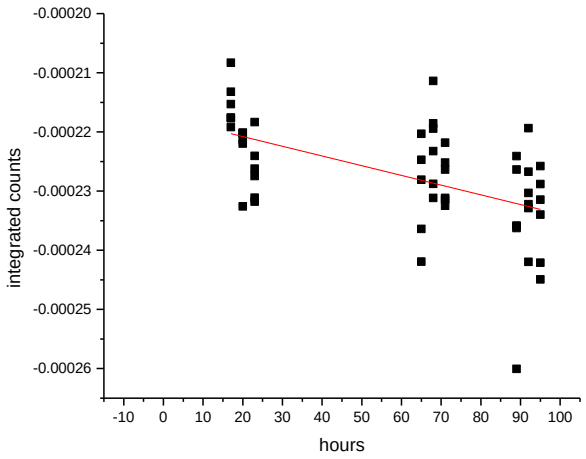

Figure 4.25. The same data as in 2.24 but day two data (42,44,47 hours) have been removed to attain a better R-squared value

4.4 Discussion &Future Work

Through the above studies it has been shown that cell viability as manifested by metabolic activity can be monitored non-invasively without any cells present in a culture. This is done by identifying certain biomarkers in a spectrum of medium that has not been cultured (NM) and seeing the difference between that and one of cultured medium (CM). It can be seen that certain peaks in the spectrum increase in intensity over the course of a multiple day test while other peaks decrease in intensity.

Through Principal Component Analysis, two definitive components emerge that span the temporal variation. The first principal component was identified as glucose, which was compared with and validated with a standard glucose spectrum. It was also determined that the glucose decreases over the four-day period. This would coincide with the fact that mammalians cells use glucose as a source of food while in culture so it is expected that it would decrease from day to day.

In addition, the 850 cm^{-1} peak has been identified as increasing over the course of the four-day experiment. This would also make sense as we believe this peak could be either a glycosylation product or the production of extracellular matrix.[73] Although we don't have authentic spectra of either material taken using the same instrument for comparison, the strength and Raman shift of this feature is consistent with the piling up of Raman activity due to many similar or identical saccharide linkages at the anomeric carbon. This tentative assignment also makes sense due to the empirical fact that organisms consume carbon containing materials to survive, and subsequently produce metabolic waste and related by-products.

A remaining challenge would be to attempt to equate or "balance" the amount of carbon consumed as glucose to the amount of carbon incorporated into this material and the increasing numbers of organisms produced throughout the life cycle of the culture. Similarly, energy balance between the consumption of energy i.e. glucose and the energy expenditures of the organisms/culture must also be maintained and could serve as another check on the completeness of the Raman spectra in manifesting the total culture metabolism.

Next it has been determined that there is the capability to take spectra of the contents of a culture flask non-invasively without disrupting the system in any manner. According to spectra shown above, for a 200 second acquisition time using our current instrumentation without any additional optimization it is *already* possible to physically see glucose peaks down to below 10 mM concentrations, a good start toward being able to look at medium studies *in vivo.*

Since we can easily 1) double that acquisition time and/or 2) double the incident laser power with a resulting improvement in raw signal to noise of *a factor of* 1.4 for <u>each</u> increase (if we are shot-noise limited), we fully expect to achieve a <2.5 mM detection limit for glucose, even with subtraction of a culture bottle spectrum. The standard glucose concentration for commercially available culture media is typically 2.5 mM so quantitatively monitoring metabolism induced changes of 0.05 mM in e.g. glucose using standard culture media on a 15-minute acquisition time, probably with higher laser excitation power should be routinely possible.

Based on the success of this exploratory study, there are many things that can and should be done with this approach. First, we plan on quantifying these components that have been extracted from the spectra of the medium testing. To do this calibration curves must be made for materials that are potentially associated with the 850 cm^{-1} peak. Using work such as that done by Amgen[80] we should be able to isolate a glycosylated product and test it for the presence of an 850

cm^{-1} peak. If, on the other hand, it is determined (possibly through trying to reproduce Amgen's work) that the peak is more likely ECM we can compare with spectra of e.g. chondroitin based materials, hyaluronic acid, and similar polysaccharide materials e.g. Glycosaminoglycans (GAGs). Alternatively, commercial extra cellular matrix materials like Laminin,[81] which is a glycosylated protein and possesses at least one linkage at the anomeric carbon, are available that present a possible path to independent calibration.

There are a multitude of things that could cause for this disruption, one of which could be connected to the polystyrene. In theory, and shown above in the flask study, the 1000 cm^{-1} peak of the spectra that is connected to polystyrene should stay relatively level for each flask (standard deviation of less than 1 percent. If we take a look at this peak across all flasks though we can see that there is a much higher variability than this in the *in vivo* study.

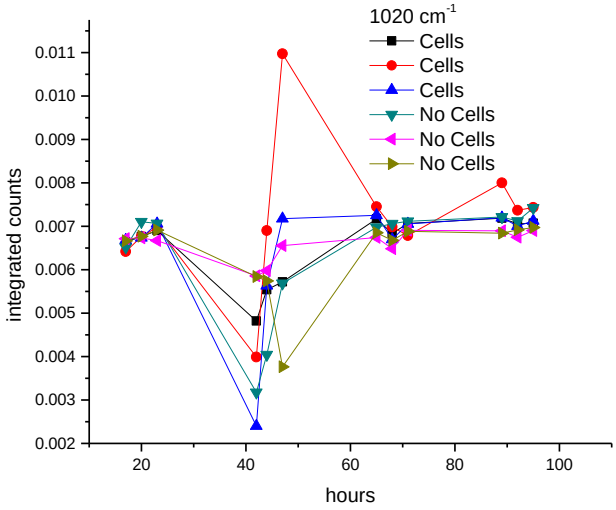

Figure 4.26. Collective data of every flask at every timepoint at 1020 cm^{-1} over entire 95-hour study

As you can see there is a mostly flat line across the data for each flask but again on day two there is a very high variability in it. This could mean that there was either an environmental factor, be it a light leak in the system, inconsistent probe placement, etc., that could have occurred causing the skewed data.

We wanted to take this further though to ensure that we would be able to cleanly see glucose in the DMEM medium that was used. In the original testing for glucose through flasks, glucose was dissolved in water. This however didn't account for a potential overlap of peaks from the medium. To verify the peaks, glucose was dissolved in the medium used for the cells in varying concentrations in a cuvette. Below you can see a sample spectrum of glucose in culture medium. As can be seen it is hard to make out glucose peaks from this medium.

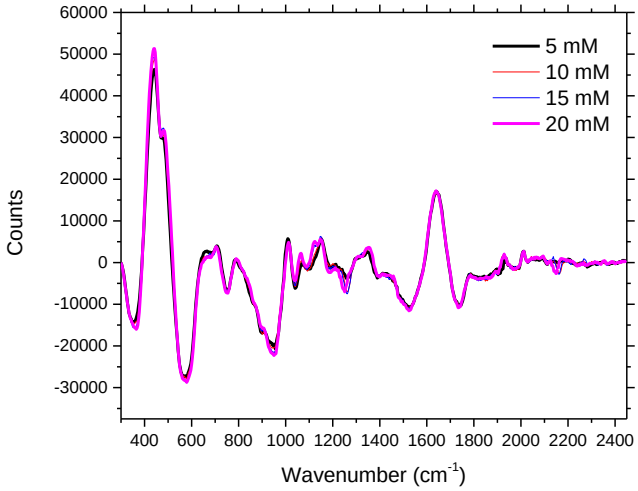

Figure 4.27. Added glucose concentrations in DMEM medium in a cuvette to simulate glucose in mammalian cell cultures.

If we stick with some of the peaks we have looked at through this study, 570. 1120, and 1345 cm^{-1}, we can see that there is indeed some overlapping the spectra above. 1020 cm^{-1} is also a known glucose peak but we can immediately rule that out as the polystyrene peak dominates that area. Through just quick observation of the above live studies as well as the polystyrene spectra early in this chapter, the broadness of the polystyrene peak overlaps the 1123 cm^{-1} peak,

thus counting it out. If we can isolate a peak that is evident in glucose but not in DMEM we might be able to still observe consumption.

One of the main ingredients to this medium is Pyruvate. This is a chemical used to facilitate the metabolic activity of the cells[82]. Below you can see a spectrum of straight pyruvate. As can be seen, it turns out that there is a prominent peak in a few of the same areas as for glucose.

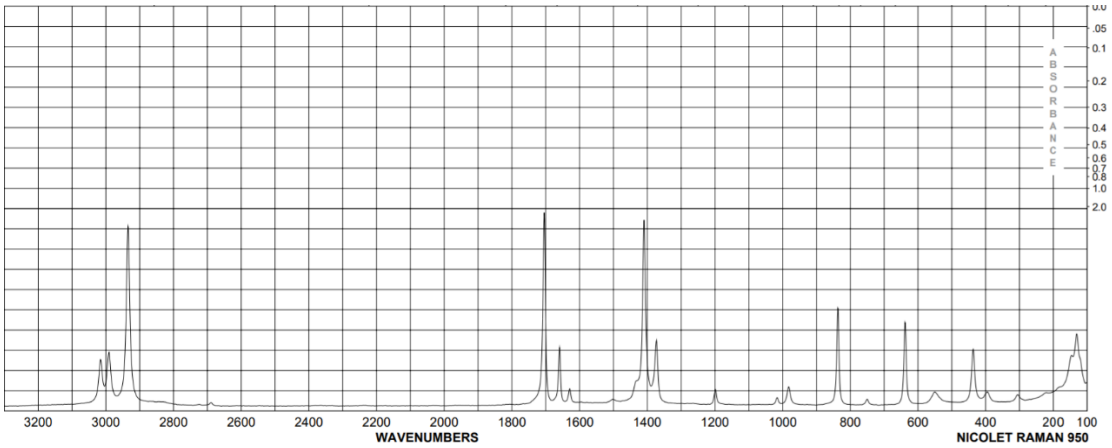

Figure 4.28. Spectrum of Pyruvate from Sigma Aldrich database. Notice the small, but distinct peak around 570 cm^{-1}

As can be seen above this pyruvate additive in the DMEM has a noticeable peak at 570 cm^{-1} (one of our original glucose marker peak) which could distort was we would think to be glucose in the medium.

Taking all the above into consideration there is still one peak however that appears to not be overlapping in either the pyruvate or straight medium spectra that behaves properly in our glucose calibration spectra (Figure 4.27). As you can see below this peak in the medium cuvette studies still increases as glucose concentration increases (Figures 4.29 and 4.30) as well as increases when placed in a flask (Figure 4.31). It also as shown above in our preliminary *in vitro* medium studies, increased in just the medium.

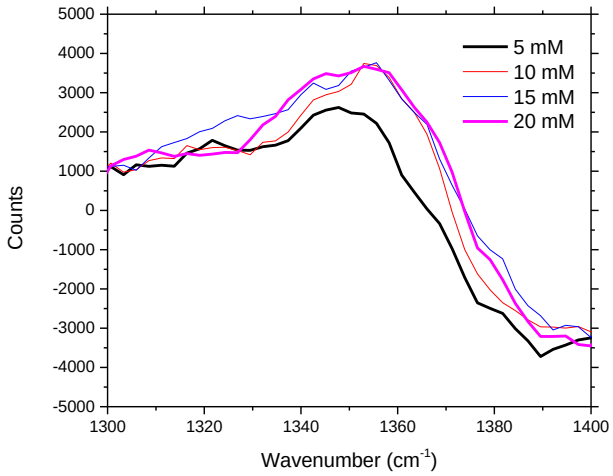

Figure 4.29. Close up of the 1345 cm^{-1} region of glucose in DMEM medium studies taken from a cuvette.

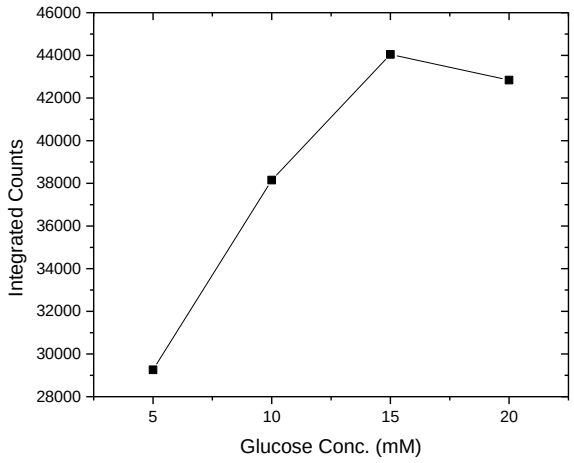

Figure 4.30. Integrated counts of each concentration of glucose at 1345 cm^{-1} in DMEM medium taken from cuvette.

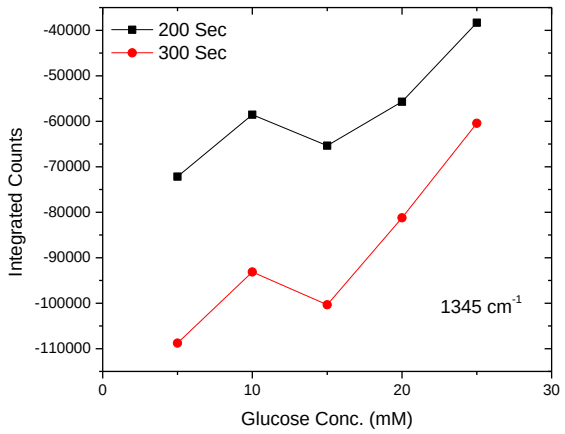

Figure 4.31. Integrated counts of glucose at 1345 cm^{-1} from glucose in water solution through polystyrene flask.

We have assumed that the excitation i.e. laser light has no effect on the cells in culture. This may or may not be true. While germicidal lamps i.e. UV lights are well known to kill bacteria and even somewhat longer wavelengths as well,[83-85] and this can be expected for most if not all cell types that utilize DNA and RNA, it is assumed that near infrared (NIR) is benign if not completely without effect. Power densities in the NIR exceeding 30W/cm^2 are approved by the institutional review boards (IRBs) for routine probing of human skin and other viable tissues. Nevertheless, we do not take this as a guarantee that NIR has no effect whatsoever. NIR is absorbed weakly by porphyrin like molecules and these species play a central role in mitochondrial function as well as other function.

As stated in the Introduction, our prominent goal is to noninvasively monitor flasks of live cultures, possibly containing sessile cells. We can do multiple types of testing on the cells e.g. simultaneously monitor glucose uptake, ECM production and possibly other substances given a more complete assignment of the observed Raman spectrum. Note that an algorithm was developed specifically to account for effects of the variable turbidity on performing quantitative spectroscopy of such cultures as they mature.[9,11,86]

As can be seen above, the process has been started to account for how many glucose molecules are being consumed by individual cells in each culture. The ultimate goal is to prove that using our method we can account for loss of glucose and gain of polysaccharide in a way of showing balance in the system. We aim to do this in real time cultures as well as just medium studies.

Long term we would like to transition to stem cell viability. A large problem that is currently seen in the harvesting and culturing of stem cells is the lack of viability after thawing since they are stored at low temperature immediately after harvesting and not defrosted until just before they are used in treatments and research.[87] We aim to use this *in vivo* technique to study the effects of natural anti-freezing proteins (AFPs) that are used for preserving frozen cells. These proteins are thought to inhibit the growth of ice crystals by binding to the surfaces of ice. This binding leads to a lowering of the non-equilibrium freezing point below the melting temperature.[88]

If we can start to understand the behavior of the AFPs then we can move toward using Raman spectroscopy in quality control and assurance (QA/QC) in commercial stem cell production. Stem cells damaged during thawing go through apoptosis, or programmed cell death, a process that is checked using markers in the cell including dye exclusion. Currently these markers can cause a reaction during the cryopreservation cycle leading to higher apoptosis rates. With an improved understanding of AFPs, their behavior with cells, and how the cells behave in general, we hope to improve preservation and recovery of stem cells thus increasing the net yield of viable cells.[88]

As discussed above you can see there are still some issues in analyzing glucose consumption from a live cell culture. It is believed that it can be attained from a different peak than what was used before. Unfortunately, due to lack of supplies another attempt was not

completed. In the future we would want to attempt another *in vitro* run. Certain things would change not only in analysis but also in experimental set up. Part of the problem with this approach is the lack of liquid in the flask (roughly 5 to 10 mL). This means that the focal point of the laser will barely be in the liquid, so it is imperative that the probe be placed in the same location and depth for each run.

4.5 Conclusions

It appears possible to non-invasively track the metabolic activity of cultured cells without disruption of the cells themselves, through means of Raman Spectroscopy as a test of viability. Results showed success in the ability to monitor glucose uptake and polysaccharide production using only medium where cells had previously been cultured. Through work with different cases we successfully showed that glucose concentration can be measured, with 95% confidence, down to 10 mM concentrations without physically sampling the culture. Extrapolation of these results strongly suggests that longer data acquisition times and higher laser power will push the lower limit of concentration even lower allowing monitoring of live cultures in real time.

Chapter 5: Using Raman Spectroscopic Techniques to Probe the Behavior of Bones, Both Healthy and Altered by High Dose Radiation Therapy Treatments, As a Method of Determination of Change in Composition and Physiology.

5.1 Introduction

As mentioned in the introduction to this thesis, a seemingly unavoidable side effect of said radiation therapy for soft and hard tissue cancer patients is post-radiation induced bone fragility and fractures. Both in frequency and type, many fractures have been reported when radiotherapy has been used as treatment. Two of the more predominant injuries that occur are in the pelvis following radiation for anorectal and gynecologic malignancies, and rib fractures following radiotherapy for breast cancer.[22,25,26] These injuries not only occur but also take longer, roughly six months or greater, than average fractures to heal.[27,28] The main goal of this chapter of the thesis is to probe radiated bones and study the chemical response to radiation that may attribute to these fractures.

These injuries not only occur but also take longer, roughly six months or greater, than average fractures to heal.[28,29] Some of these injuries even require bone resections to salvage the limbs.[89] Advances have been made to identify risk figures that cause these fractures but overall they are still difficult to predict. Other types of preventative measures such as radiotherapy dose modification remain elusive and no conclusive decision for treatment for high risk patients has become available.[90,91]

One large limiting factor for moving toward a solution for this problem is a general ignorance of the physiology and pathology that causes bone fragility in radiotherapy patients. Clinical trials have not presented much positive results as to how radiation induced processes cause bones to become fragile and require more time to heal than normal fractures.[30,31] Early studies used

full body irradiation and thus are less applicable to the current problem. [30,31] Newer but still limited studies were conducted using a more focused radiation field but the study seems inconsistent and inconclusive with its aim to explain the weakened bones.[32] An independent clinical study showed that irradiation did not routinely decrease bone density and further suggested a material abnormality internally in irradiated bones.[33]

To further the Morris group studies, we produced a Raman spectroscopic system that is intentionally *not* identical to their system but should produce results that can be related to their observations, possibly leading to a better overall understanding of the state of the system i.e. bones. The Gong work used a Raman microscope which preferentially samples the near surface region of the bones. Retesting the work of the Gong study with our system may provide a more nuanced assessment of their results and their interpretation since our system samples the bones at greater depths. The correct understanding will be able to explain these results as well as the Gong results. Moreover, simply probing different parts of the bones e.g. the same locations relative to macroscopic bone features i.e. diaphysis or metaphysis but deeper, may reveal morphology and processes that simply do not occur on the surface. We have searched for changes and abnormalities that can be seen in treated bones.

We also aim to study the compositional and morphological differences of bones that will be used subsequently in fracture toughness tests to assess the likelihood of a break by documenting the stress that is needed to break. Combining actual mechanical testing with Raman testing could put more of a meaning to the values that the Morris group has discovered. We study the difference between groups of bones as well, from untreated bones (sham), to bones that have been treated with radiotherapy (irr) and bones on the other side of the body of an irradiated limb (contra-lateral). The contralateral bones have been used in other studies as controls and the appropriateness of this

choice of control can also be assessed in our work. We lastly want to examine more closely the inside of the bone, the marrow and blood supply and see what physiological changes occur in the cavity of the bone as radiotherapy occurs. This work is well beyond the protocol employed by the Morris Group in the Gong paper.

5.2 Experimental

5.2.1 Raman Spectroscopy

Raman measurements are made using a 785 nm, continuous wave external cavity laser (Process Instruments, Salt Lake, UT) with a measured power of no more than 150 mW at the location of the sample in a bandwidth of 1.5 cm^{-1} within a multimode spatial distribution. The spatial distribution of the laser is roughly a square shape with a spot size of roughly 0.125 mm wide at the focus as measured using burn marks on Zap-It® paper. The sample bones are held by a custom-made holder created in the machine shop with fiducial markings spaced 1 mm apart for measurement purposes (Figure 3.1). The sample holder is modeled after a cuvette to fit the existing holder, hollowed in the middle to minimize reflections and painted black. The depth of focus of the laser was set so that the focus i.e. beam waist of the incident light was placed in the center of the bone cavity. The actual focus was located by observing the extinguishing of the beam in the far field while crossing the beam with a razor blade at various locations until the direction of movement of the blade cannot be discerned.[92] This actually occurs over the full depth of focus of the beam and so the waist was taken as the center of this range.

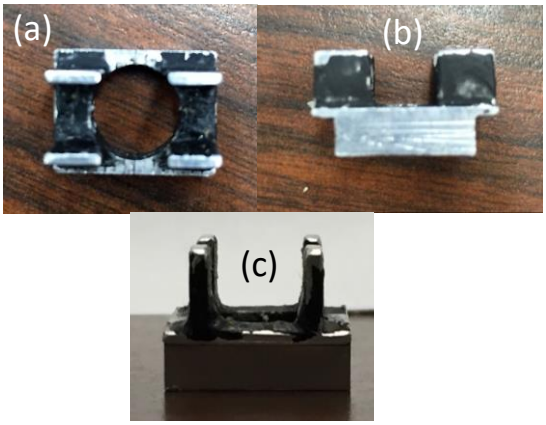

Figure 5.1. Sample holder from the top (a), Side (b) and end(c). The base was cut off to better fit in the cuvette holder. The spacing is roughly 1cm between "arms".

Data from the study was collected on an Andor CCD Camera, which was cooled to -55°C with an acquisition time of 2 minutes. There were 6000 accumulations of 20 msec frames for each spectrum. The set up can be seen below in Figure 5.3.[11] Not shown in the Figure are two added optical elements that are inserted to measure depolarization ratios. A half-waveplate (WPMH05M-78, Thorlabs, Inc, Newton, NJ.) was placed in between the laser and first clean up filter in order to select the polarization direction of the laser beam so as to be parallel or perpendicular to the long axis of the diaphysis of the sample.

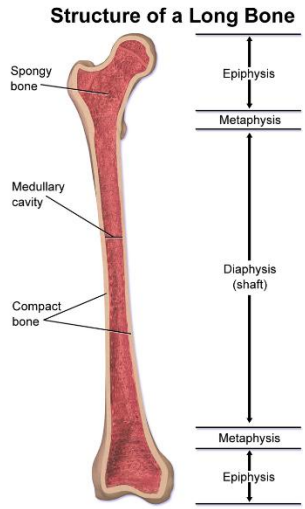

Figure 5.2: Anatomy of a Femur.[93]

A polarization analyzer (LPNIR050, Thorlabs, Inc, Newton, NJ) was placed between the final focusing lens and the spectrograph to select the parallel or perpendicular polarization components. These optics are the same as in the Gong work, as was the 50 µm slit employed in the spectrograph. Dark Currents were collected over the same time frame and subtracted to ensure no Raman shift dependent noise was added from the CCD chip before baseline subtraction.

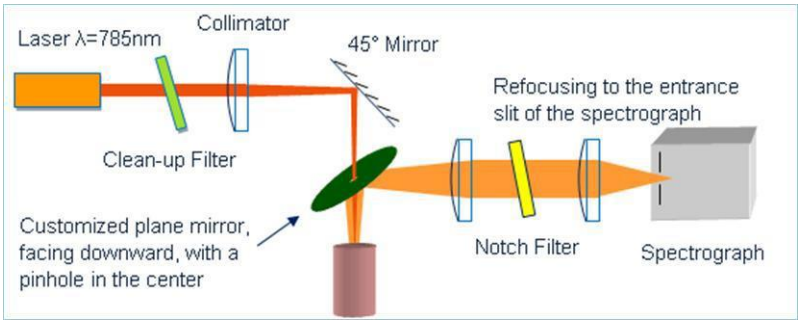

Figure 5.3. Experimental setup of the 785 nm NIR laser with added half-waveplate and polarization analyzer (not pictured) that were also employed for the experiments.[11]

The same set up as described in chapter one for the 830 nm laser was also employed. The only change was exposure time of 120 seconds as opposed to 200, making for 6000 accumulations as opposed to 10000. The laser power was also kept 160mw CW. Dark current spectra were again run prior to each session and subtracted from all spectra to ensure no discrepancy due to pixel dependent CCD noise.

Data analysis was again carried out in Microsoft Excel and Origin 9.1. Raw spectra were cropped to the range of roughly 550 cm^{-1} and a "101-7" arbitrary baseline smoothing as described in Chapter 4 of this thesis was again applied to extract Raman features from the raw spectra. Calculations were carried out by identifying local minima adjacent to peaks of interest and assigning the indicated baseline of the peak to 0 counts. Integration was then done on each peak and calculations were done with integration parameters i.e. Raman shifts following the Gong paper. Table 5.1 below describes which peaks were used for each parameter. To ensure that integrations were accurate across a homologous series of spectra, the same points adjacent to peaks were used to adjust the integration baseline so integration was of purely the peak with no blank counts included.

Table 5.1. Parameters Used for Study from Gong[39].

Parameter	**Peaks used**
Mineral/Matrix Ratio	958 cm^{-1}/ (854+871) cm^{-1}
Carbonate/Phosphate Ratio	1070 cm^{-1}/ 958 cm^{-1}
Mineral Crystallinity	1/width at half-height of 958 cm^{-1}
Collagen Cross-Linking Ratio	1660 cm^{-1}/1685 cm^{-1}
Depolarization Ratio of Mineral	$I_{985\ perpendicular}$ / $I_{985\ parallel}$
Depolarization Ratio of Collagen	$I_{1660\ perpendicular}$ / $I_{1660\ parallel}$

5.2.2 Depolarization Ratio

Determination of the extent of depolarization of the system was needed to show that the new lenses in fact worked. Carbon Tetrachloride was used as a standard as it has 3 well defined peaks each with a well-defined depolarization ratio[94]. The sample was first run on a real time status on the 785 nm laser to align the half-wave-plate and polarization analyzer in a way that a definitive parallel and perpendicular range could be set to zero and 90 degrees. The optics were also adjusted to maximize signal of Carbon Tetrachloride.

5.2.3 Preliminary Bone Work

A preliminary group of random murine tibias and femurs from different studies were supplied to us from the Damron group at Upstate University. Normal spectra were run on the bones to determine if the different probing characteristics e.g. depth of focus and beam size and shape replicated the data from the Morris group. Studies were conducted using the 785 nm and 830 nm lasers to explore the effect of variation of the multiple parameters for the study, i.e. laser power, duration of scan, and slit width. Bones were scanned at different orientations as well as different location on bones.

To better understand where the laser was probing, the metaphysis of each bone, both tibia and femur, were cut off using medical scissors. The bones were then washed out using saline solution (0.9% NaCl) and images were taken again. Finally, 1M glucose was injected into the bone cavity and another scan was taken. This was also conducted on both the 785 nm and 830 nm laser.

5.2.4 Blind Bone Case Study

Murine samples were supplied from the Damron group at Upstate University. The list of samples included eight mice. Four of the mice were controls (sham (S), each providing two control tibias and two control femurs for testing, 8 control samples total. Four of the mice were irradiated (IRR) for 4 weeks prior to sacrificing. Only one side of each of the four mice was treated with radiotherapy. This gave four tibias and four femurs that had been treated with radiotherapy. The opposite side limb of the mice (Contralateral (C)) was not treated with radiotherapy but was still supplied to test for differences between it and the control limbs. This gave a total of 32 bones, 16 tibias and 16 femurs for blind testing.

Each bone was set in the custom holder in the 785 nm instrument so the test spot was near the middle of the diaphysis and run twice, once with the polarization parallel and one with it perpendicular. The bone was then moved over to the 830 nm laser and run on that instrument. To ensure that the 830 nm laser did not damage the bone it was then run again with the polarizer set parallel on the 785 nm laser. The bone was then relocated and the metaphysis of the bone was tested with the polarizer set to parallel. The bone was kept hydrated between scans by using a dropper bottle of saline solution (0.9% NaCl).

The metaphysis of the femurs was then chopped off and the inside marrow was sucked out using a standard syringe and washed with saline solution. These bones were then run again as an "empty" bone. We have dubbed this process "Marrow Cavity Evacuation" (MCE)

5.2.5 Depolarization Sampling In a Turbid Medium

Enough carbon tetrabromide (Sigma Aldrich Density:3.42 g/cm^3) was added to 7.2 ml of carbon tetrachloride (Sigma Aldrich Density:1.59 g/cm^3) to make 10 ml of a mixture with density of 1.80 g/cm^3. Quartz spheres (Cospheric, Inc. 8μm dia. Density 1.8 g/cm^3) were added in 250 μL aliquots from a 0.013 (v/v) stock solution. The solution was then stirred in cuvette to assure suspension of the spheres mimicking turbidity. Stirring was stopped just prior to scans being collected. Collection data was taken with the same parameters as the bone samples. Parallel and perpendicular scans were taken for each of the 10 samples.

5.3 Results

5.3.1 Preliminary Work with Polarizers and Bones (785 nm laser)

The lowest depolarization ratio that could be attained was roughly 0.05. This is 10 times the literature value of carbon tetrachloride which has a depolarization ratio of 0.005[94]. Figure 5.4 shows spectra of CCl_4 with the polarizer set to both parallel and perpendicular settings. With perfect aberration-free optics it's not possible to obtain polarized Raman spectra that exhibit greater polarization than the incident laser light itself. According to the manufacturer of our 785 nm laser (Lee Smith, Process Laser Inc. Salt Lake, UT) the laser polarization ratio is 0.02 accounting for about half of the discrepancy between our measured CCL_4 depolarization ratio and the literature value. The performance is actually quite acceptable for our bone study purposes since the strongest depolarization ratios that are expected, based on the Gong[39] work, are no less than 0.2 and we can measure down to 0.05. We note that it is not stated in Gong et. al how well their system works on a standard isotropic system e.g. CCl_4. Given the specifications of their laser[39] (obtained from their laser manufacturer Scott Rudder, Innovative Photonic Solutions, Monmouth

Junction, NJ) it also has a polarization ratio of 0.02 and their lowest measureable depolarization ratio is the same as ours.

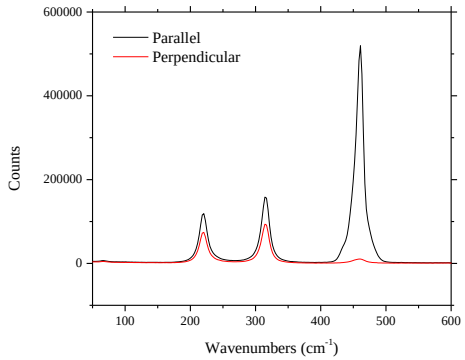

Figure 5.4. An overlap of Carbon Tetrachloride both with parallel (black) and perpendicular (red) polarization alignment.

Our next task was to assess our capability to replicate depolarization ratios from bones to that of the Morris Group. Below a raw spectrum of a bone as well as the 101-7 baseline corrected spectrum can be seen.

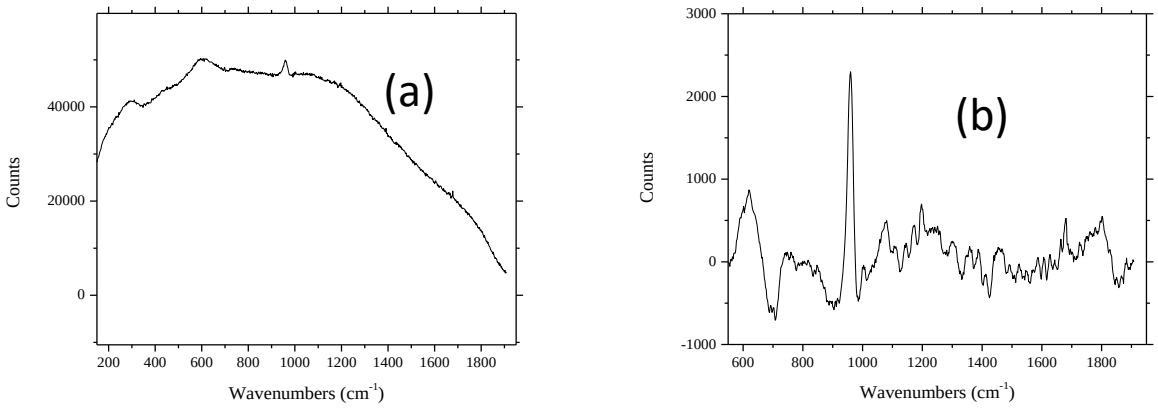

Figure 5.5. Raw spectrum (a) and (b) 101-7 baseline subtracted spectrum of a Femur using the 785 system.

The raw spectrum contains fluorescence from the bone material and any blood that may still be contained in the bone. Notice that the peak at roughly 958 cm^{-1}, which is referred to as the phosphate or hydroxyapatite peak, can be seen even before the baseline subtraction is performed. This peak is prominent in all bone spectra e.g. as presented in the Gong paper. Other peaks of interest that coincide with the Gong paper are 1070 cm^{-1} (carbonate), and 1650 cm^{-1} (amide I). A certain peak that we found of interest that the Gong paper acknowledges but does not use in bone monitoring is the 1445 cm^{-1} peak that they refer to as "CH_2 deformation". This Raman feature is actually a strong indicator of fat and to a lesser extent protein whenever it is observed. The same procedure was done with tibias to check for similarities (Figure 5.6).

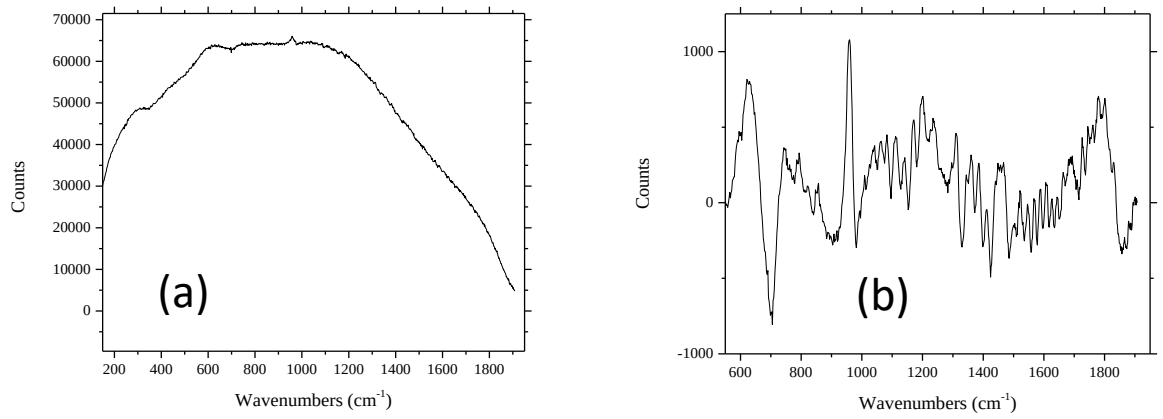

Figure 5.6. Raw Spectra (a) and 101-7 baseline corrected spectra (b) of tibia on the 785 laser.

After looking at the spectra above we changed the polarization analyzer to perpendicular and performed another scan. According to the Gong paper, the integration of the 958 cm^{-1} (I_{958}) for the perpendicular spectrum should be roughly 21 percent i.e. $I_{958perp}/I_{958par}$ =0.218. Below you can see an overlap of the parallel and perpendicular spectra.

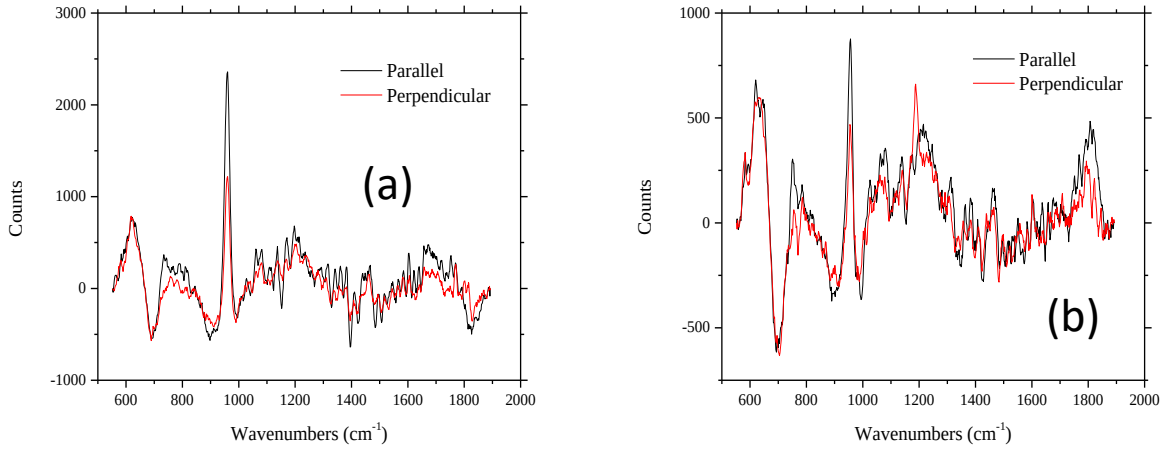

Figure 5.7. The parallel and perpendicular spectra of Femur (a) and Tibia (b). It should be noted that though some peaks appear to be more intense when perpendicular, after baseline corrections and integration the area is roughly the same as parallel, if not less.

As can be seen from the above, there is a large change in the peak intensity of the 958 cm^{-1} peak. When an integration was performed on each peak though, it was found that the ratio ($I_{958perp}/I_{958par}$) was roughly 0.59 and 0.64 for the femur and tibia respectfully. We tested the other parameters with a set of 6 tibias and 6 femurs however and compared them to the Gong paper, which can be seen below in table 5.2.

Table 5.2: Raman Parameter Calculations on the 785 nm laser for comparison with Gong et. Al[39].

Raman Parameter	Femur Measurement	Tibia Measurement	Gong Paper
Mineral/Matrix	N/A*	N/A*	14.67 ± 3.11
Crystallinity	0.047 ± 0.002	0.0457 ± 0.002	0.0572 ± 0.06
Carbonate/Mineral	0.201 ± 0.037	0.200 ±0.044	0.246 ± 0.022
Collagen Cross-Linking Ratio	2.698 ± 0.362	2.687 ± 0.763	2.29 ± 0.44
Depolarization Ratio of Mineral	0.632 ± 0.027	0.644 ± 0.045	0.218 ±0.047
Depolarization Ratio of Collagen	0.597 ± 0.070	0.503 ± 0.066	0.556 ± 0.041

*No Matrix peak (874 cm^{-1}) was clearly dominant in the spectra collected
N=6 for both tibia and femur.
± is Standard Error (Standard deviation divided by the square root of N) for our data and standard deviation for Gong data.

The data in the table above affirms that our system does in fact reproduce nearly all of the Morris group results. However, the hydroxyapatite peak depolarization ratio did not replicate the Gong paper result. This will be discussed in greater detail in the Discussion section, however, knowing that Raman signals originating deeper in the bone would experience more polarization changing scattering before being detected and that the effect would be to increase the measured polarization ratios, the lack of agreement stimulated a series of experiments to determine the origin of the Raman signals.

To test the hypothesis that our probing of the sampling site was deeper than the Gong data we employed two tactics. First, we chopped the metaphysis off the bone and using a syringe, sucked the marrow out of the cavity of the bone. The removed material was beyond translucent not allowing one to view images through a thin coating on paper. Also, as expected, it was yellow with red depending on the amount blood mixed in. It should be noted that these bones were not rinsed with saline (as in later studies). Figure 5.8 below shows both the raw and baseline corrected spectra of a representative femur that has been cleaned out. It should also be noted that this was attempted with tibias as well, but the cavity was too small and thus it could not be sufficiently cleaned.

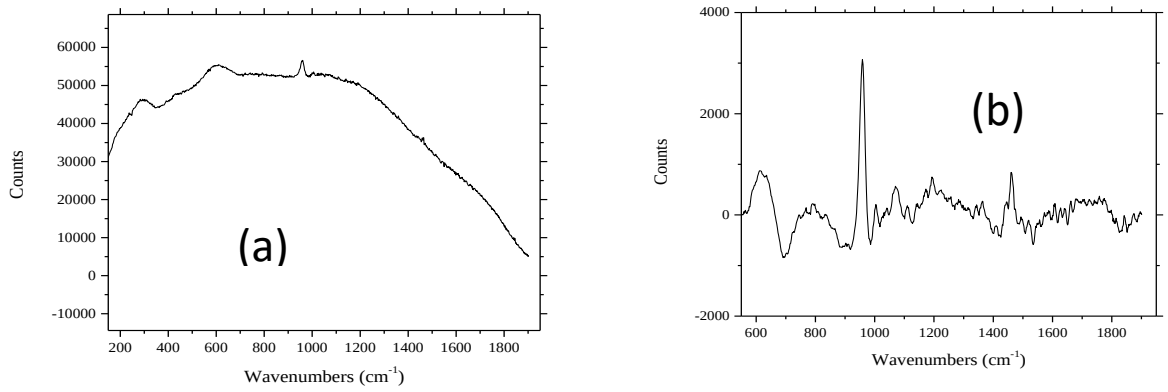

Figure 5.8. Raw spectrum (a) and 101-7 baseline corrected spectrum (b) of an empty femur.

When the full femur and empty femur spectra are plotted together, both baseline corrected, (Figure 5.8) it can be seen that the 958 cm^{-1} peak increased significantly with MCE. This makes sense since removing a multiple scattering material out of the medullary cavity would 1) allow increased penetration of the incident laser to the other side of the bone causing higher signal from matrix and 2) increase the fraction of remitted light from both sides of the cavity region that reaches the detector.

The 1450 cm^{-1} peak appears to have two components, 1435 cm^{-1} and 1465 cm^{-1}, one that sharply increased and another small shoulder that was much less strongly affected by MCE. This suggests that the two features that overlap to form the 1450 cm^{-1} peak originate from *both* the matrix itself and materials in the marrow cavity of the bone. This is not surprising[95] since>35% of the primary structure of collagen is proline and hydroxyproline and both of these amino acids have at least 2 CH_2 groups each that will contribute to Raman scattering near 1450 cm^{-1}. Thus, we must consider propagation of light in different regions of the bone to understand how collagen found in the bone matrix could contribute to the 1450 cm^{-1} activity and be affected by our changes to the marrow cavity. With turbidity i.e. multiple scattering in mind we consider the question of the optical properties of the marrow contents.

Beyond the empirical observation that the extracted material appeared beyond translucent, we know that in addition to a variety of cells, from stem cells to various blood cells including red blood cells (RBCs), the marrow cavity contains fatty materials that are not soluble/miscible in water and that there is water also in the marrow cavity. Thus, we expect micro globules of fat and water to be dispersed in the marrow cavity, creating a substantial multiple scattering within the marrow cavity. We also know[96] that the scattering coefficient for RBCs is 30 mm^{-1} indicating that on average a photon experiences 3 elastic scattering event per 10 μm of path. As will be discussed

and shown directly below, in addition to polarization randomization, multiple scattering leads to radiation trapping and net loss of signal.

As a separate issue we suspect that it's also likely that that since the bone was not washed with saline, some marrow cavity materials including fat, instead of being fully cleaned out, were pushed by the syringe needle into the cracks and crevices of the bone wall forming the marrow cavity, which could increase the Raman signals from those materials. Furthermore, we observed that the needle is a close fit to the marrow cavity and the internal surface of the marrow cavity is scraped clean of surface materials to some extent, in some locations i.e. the bone is not a perfect cylinder in addition to being bent. Since the internal diameter of the marrow cavity is not constant, both removal of wall and redistribution of marrow materials probably occurs that to some extent is ameliorated by the saline wash.

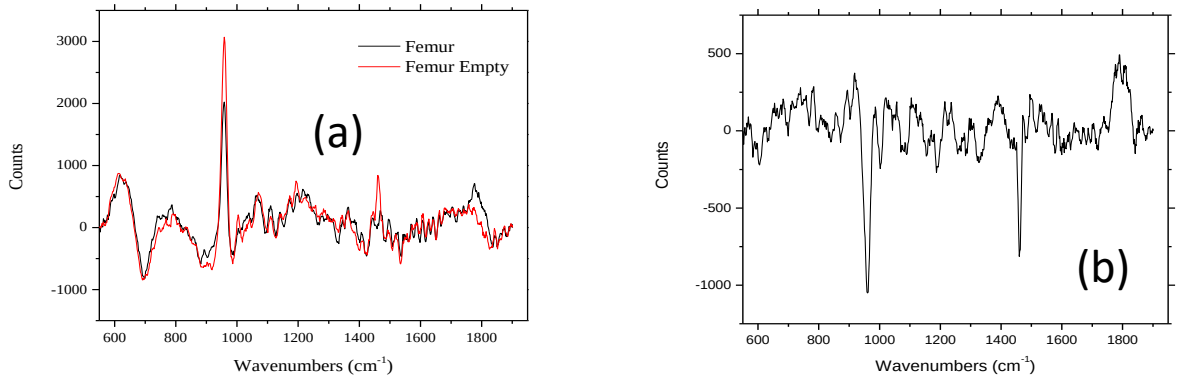

Figure 5.9. Overlap of Femur and empty femur (a) and difference spectra of a (b).

To reaffirm that we were in fact sampling the inside of the bone and not just the surface, 1M glucose was deposited into the cavity and spectra were taken. As can be seen below in Figure 5.10, there is a noticeable difference in the bone spectrum when the glucose is added at roughly 1100 cm^{-1}. Referring back to Figure 4.5 (from Chapter 4) we can say that these new peaks are conclusively glucose.

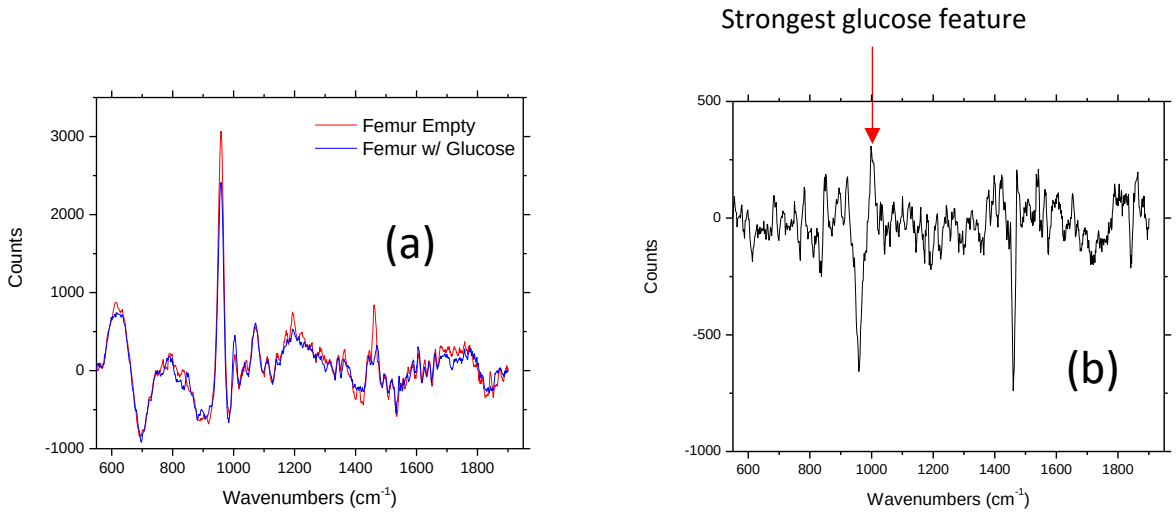

Figure 5.10. Overlap of empty femur with femur filled with glucose spectra (a) and difference spectra (b)

This issue of propagation effects on the amount and type of e.g. Raman emission detected with variable local turbidity is the reason why attempts to quantify Raman signals from turbid media that might yield chemically/clinically useful information began by considered ratios. To understand this better, consider that the basic detected Raman signal e.g. Raman scattered intensity or power can be expressed simply in terms of constant applied laser power (I), the concentrations [C_n] and Raman scattering coefficients (RS_n) of scatterers in the probed volume, and the value of the *effective* probed volume itself (V). This volume is the locus of the paths of the incident and scattered photons to/from the laser, through the probed volume, and to the signal detector. This locus of paths is determined by the turbidity of the medium, a bulk optical property expressed in the Radiation Transfer Equation (RTE)[97] as the scattering coefficients of the materials present in the medium. In addition to using the RTE to determine the effective probed volume[98], Monte Carlo simulations can also be used, particularly in highly multiple scattering media[99].

Combining factors, *within a single spectrum*, the signal strength at 2 arbitrary Raman features, ν1 and ν2, can be expressed formally as:

$$R_{V1} = I \times [C_1] \times RS_1 \times V$$

$$R_{V2} = I \times [C_2] \times RS_2 \times V$$

Both signals come from the same spectrum and so, the same volume, such that the ratio would be:

$$\frac{R_{V1}}{R_{V2}} = \frac{(I \times [C_1] \times RS_1 \times V)}{(I \times [C_2] \times RS_2 \times V)} = \frac{([C_1] \times RS_1)}{([C_2] \times RS_2)}$$

This result is independent of the volume and so also the turbidity.

Since the Raman cross sections are molecular properties that are constant (assuming constant local dielectric environment as is the case here), stimuli that cause *relative* concentration changes can be observed quantitatively with some rigor. The problem here is that changes in a ratio could occur simultaneously in both the denominator and numerator and without one actual measurement of the change in at least one analyte by itself, the ratios can be misleading. We will return to this issue below and propose another approach to making quantitative comparisons in the context of MCE experiments.

Having confirmed empirically that some observed Raman features contain contributions from the inside of the bone i.e. from the medullary cavity and knowing that bones contain a greater volume fraction of fatty materials in the medullary cavity yellow marrow when stressed[100], we examined the behavior of the 1450 cm^{-1} peak with MCE to determine its relationship with the hydroxyapatite and amide I peaks. To do this, following the lead of the Morris Group (which we discuss more fully later) we compared two ratios, 1450/958 and 1450/1650 (Table 5.3).

Table 5.3: New parameters involving fat peak

Raman Parameter	Femur normal	Femur Cleaned out*
1450/958	0.584 ± 0.397	0.554
1450/1660	4.647± 0.073	8.026

*Only 1 Femur was cleaned out to test, giving no ± value.
± refers to Standard Error (Standard deviation divided by square root of n)

The table suggests that when the femur is cleaned out, the 1450 cm^{-1} feature may change slightly more than the hydroxyapatite and if it does change, it *tends to* decrease relative to change in the 958 cm^{-1} peak. As the hydroxyapatite peak is predominantly in the walls i.e. the compact bone matrix, this could make sense then if 1450 cm^{-1} feature is found both in the compact bone matrix and in the marrow. This is a strong case for the argument that we are probing deep the inside of the bone but that the signals from outside the marrow cavity are much stronger or easily detected than those from inside.

The relationship between the 1660 cm^{-1} and 1450 cm^{-1} peak would also appear to make some sense. Nonstructural proteins, and cells that must contain protein, which have a broad amide I feature near 1660 cm^{-1}, are known to exist in the marrow cavity with the fat. Water is also present in the marrow cavity and it can affect the 1660 cm^{-1} region because water produces a relatively broad and very weak spectral feature in that region. Given the results we can accept that removal of the marrow contents decreases the 1660 cm^{-1} feature twice as much as the 1450 cm^{-1} feature.

This being said it would be expected that both values would change and the behavior of the ratio may be tougher to predict. It was definitive that more studies and a better methodology was needed for cleaning bones out and studying the materials removed. This preliminary study showed that the 1450 cm^{-1} peak might be very useful in probing what occurs physiologically inside the bone after radiotherapy. Furthermore, these observations show even more definitively that our set-up is probing deeper into the bone than the Morris Group did, as shown schematically below in Figure 5.11.

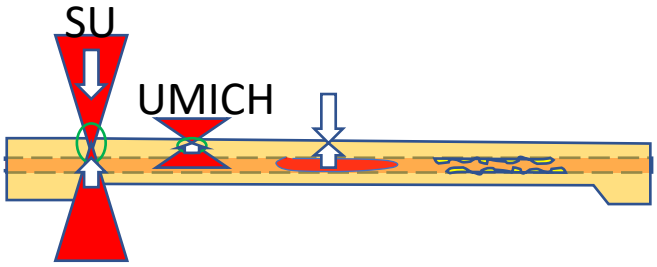

Figure 5.11. Schematic of believed focal points and collection cones of both our laser set up as well as the Morris Group at UMICH.

To fully appreciate the effect of propagation of light in turbid media on both the strength of signals and the numerical value of depolarization ratios we note that we have examined this effect in isotropic media with controllable turbidity[11,101]. Figures 5.11 and 5.12 accurately depict the effect turbidity has on scattered light. Turbidity is observable when photons experience direction and polarization changing collisions i.e. scattering events between the location where they are created and the location where they are observed/detected. In general, the polarization and direction of light is changed to some extent with each scattering event, elastic or inelastic. Figures 5.12 and 5.13 below depict the effect of turbidity on light and scattering. Scattering off objects and index of refraction boundaries tend to be in the forward direction when the object/boundary is nearly the same size as the incident light wavelength and this applies to both the propagation of

the Raman scattered light and fluorescence to where it is detected as well as the propagation of incident laser light to the locations where Raman and fluorescence are produced.

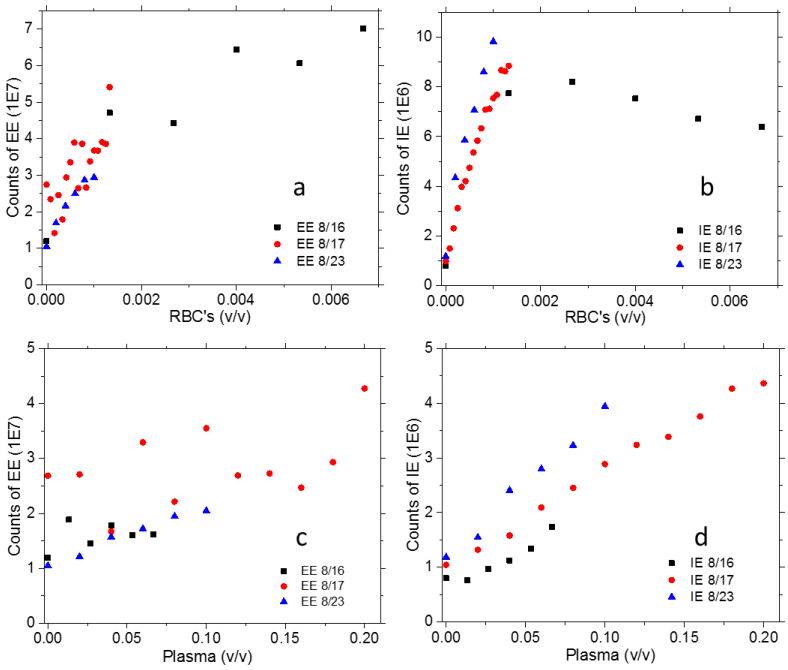

Figure 5.12. IE and EE of both RBCs (a and b) and plasma (c and d) volume fractions analyzed over several days. A clear depiction that at a certain volume of RBCs (higher turbidity) the IE tends to level and even decrease again.[101]

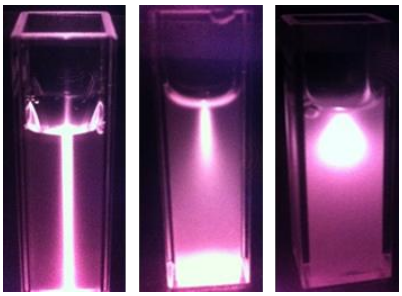

Figure 5.13. Images of 785 nm irradiated diluted plasma, RBCs, and concentrated RBCs (from left to right). A visual showing the propagation and eventual trapping of light as the solutions become more turbid and multiple scattering increases from left to right.[101]

When no more than 1 collision i.e. scattering occurs on average in that spatial interval, the net effect is to decrease the amount of light observed/detected in accordance with a Beer's Law type dependence[102]. But when multiple scattering is the predominant process, as must be the case in optically dense materials like bone marrow and oil/water or water/oil emulsions, 1) the total amount of remitted light can actually *decrease* with increasing scattering material i.e. path length and/or density and 2) any polarization of the light is randomized. Thus any chance of observing meaningful polarization ratios is lost if the incoming light experiences multiple scattering events and/or when the Raman/Rayleigh/Mie scattered light experiences multiple scattering events before being remitted and eventually detected. We use these ideas to note the differences between these results and Gong results.

The differences between the Chaiken Group and the Michigan 785 nm data can be attributed to the fact that the Morris Group is using a Raman microscope having a very shallow depth of focus with 100% backscattering geometry and thus are sampling only the surface of the bone and our laser is going deeper into the cavity of it. As the incoming and remitted light is more multiply scattered as signal is obtained from deeper in the bone, we expect less meaningful polarization ratios and even less signal itself when the density and path lengths are too large. Since we sample farther into the bone, and photons are interacting with marrow and to some extent red blood cells (RBCs), we know that less photons will be remitted.

RBCs have a very large scattering coefficient[97] and multiple scattering is the rule for all but the most dilute materials/tissues containing RBCs, as shown above in Figures 5.11 and 5.12. Moreover, when lipids and aqueous media fill the marrow cavity, we expect *at least* two phase behavior i.e. lipid globules in contact with aqueous media and these interfaces are powerful scattering centers. Thus, as observed in Figure 5.8 when we probe a bone with an empty marrow

cavity we expect more remitted Raman from the hydroxyapatite than if *anything* is in the marrow cavity, particularly RBCs and lipids. Organized protein containing regions would be expected to also contribute scattering centers as well. The exact same reasoning also explains the differences between our measurements and the Gong measures of crystallinity.

5.3.2 Preliminary Work with Bones (830 nm laser)

Having replicated the Gong work using 785 nm excitation, and explained to our satisfaction the differences and similarities we proceeded to see the effect(s) of using 1) a different excitation wavelength i.e. 830 nm, with 2) a fiber coupled probe with a somewhat wider collection cone ≈f3.We knew from the start we would not be able to utilize depolarization ratios with the commercial 830 nm instrument because its design does not accommodate the necessary polarization optical elements. Figure 5.14 below shows again the Raw and 101-7 data of bone done on the 830 nm instrument.

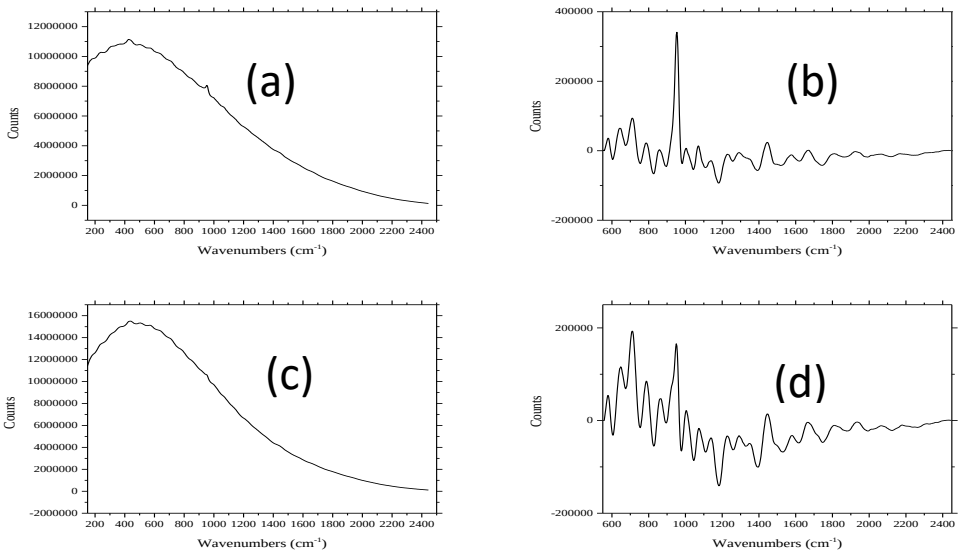

Figure 5.14. (a) Raw Spectrum of a Femur on 830 nm instrument. (b) 101-7 Baseline corrected spectrum of (a). (c) Raw spectrum of a tibia on 830 nm instrument. (d). 101-7 baseline corrected spectrum of (c).

As can be seen the spectra look similar to those using the 785 nm laser. There were benefits as well as disadvantages to using the 830 nm instrument though. The benefits of the 830 nm instrument include that 830 nm wavelength is much more weakly absorbed by blood and so produces much less fluorescence. Also, one of the reasons we used the lower power on the 785 nm instrument is that with especially femurs, the blood remaining in the bone marrow following excision was causing the bones to burn before a good spectrum could be taken. This was not an issue with the 830 nm instrument.

One major disadvantage is clearly the inability to use depolarization ratios. Another large disadvantage, though it works in our favor in the lower end of the spectrum, is the resolution. The improved resolution causes more distance in between data points and causes for certain peaks, for example, the 1660 cm^{-1} and 1685 cm^{-1} peak to mix together into one. This makes calculating a collagen cross-linking ratio, a parameter that may be paramount in identification of damaged bone, difficult to identify.

As shown in Table 5.4 we were able to obtain some of the same parameters as for the 785 nm instrument.

Table 5.4. Raman Parameter Calculations on the 830 nm laser for comparison with Gong et. Al[39].

Raman Parameter	Femur Measurement	Tibia Measurement	Gong Paper(Tibias)
Mineral/Matrix	4.276	2.314	14.67 ± 3.11
Crystallinity	0.037	0.037	0.0572 ± 0.06
Carbonate/Mineral	0.179	0.266	0.246 ± 0.022
Collagen Cross-Linking Ratio	N/A	N/A	2.29 ± 0.44
Depolarization Ratio of Mineral	N/A	N/A	0.218 ±0.047
Depolarization Ratio of Collagen	N/A	N/A	0.556 ± 0.041

*Note that there is no uncertainty as each test was only run one time (n=1).

It can be seen above that these numbers, though close to the literature, lack a large sample set, as well as the combination of the 1685 cm^{-1} peak and the ability to get depolarization ratios which would allow for a full data set. The 830 instrument does give a better spectral resolution which could be useful but to utilize it fully, other issues would need to be worked out. In following with the 785 nm protocol, the Femur was then cleaned out, and filled again with glucose. These spectra can be seen below in Figure 5.15.

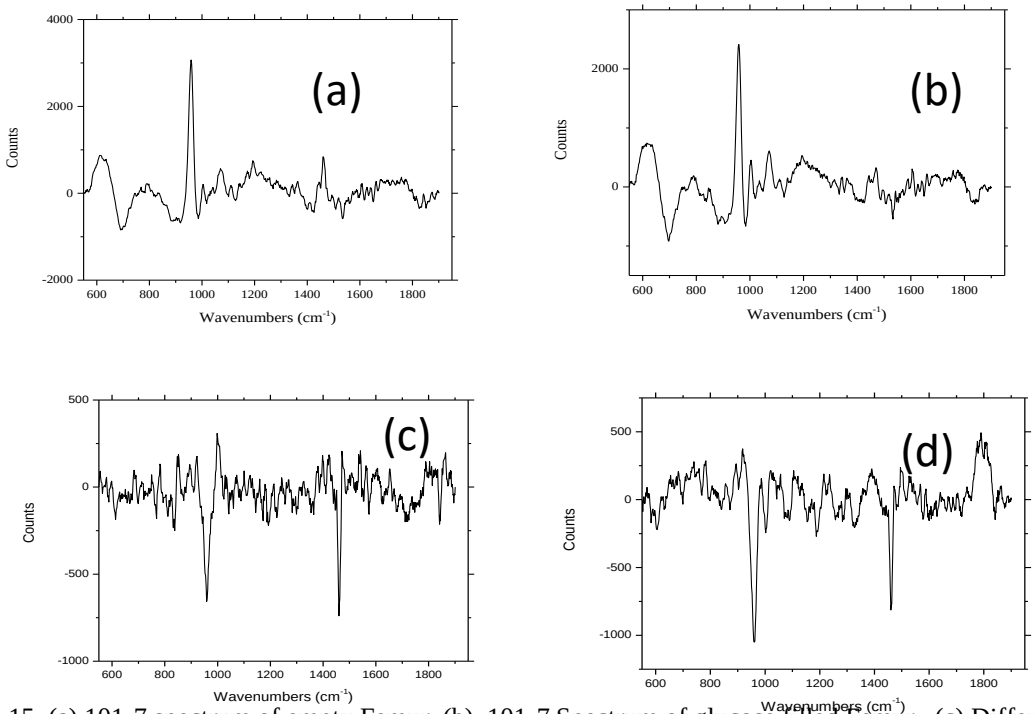

Figure 5.15. (a) 101-7 spectrum of empty Femur. (b) 101-7 Spectrum of glucose filled Femur. (c) Difference spectrum of Femur-Empty Femur. (d) Difference Spectrum of glucose filled femur-empty femur.

Again we decided to evaluate the ratio of 1450 cm^{-1} to both 958 and 1660 cm^{-1} to see how the fat related to both the hydroxyapatite and the protein. The results can be seen below in table 5.5.

Table 5.5: Parameters involving fat peak

Raman Parameter	Femur normal	Femur Cleaned out
1450/958	0.367	0.348
1450/1660	1.424	2.017

*Note that no uncertainties were found as sample size (n) was only 1.

As in the same experiment using 785 nm excitation we observe the 1450 to 958 cm^{-1} peak ratio barely decrease after the marrow is completely sucked out of the bone. The change in fat while the protein peak relative change is significant, indicating that we are probing deep into the bone even in this somewhat different probing geometry. The evidence is clear that more studies and more samples, both control and irradiated needed to be done.

5.3.3 Blind Study Test

A larger data set needed to be analyzed with control (sham), irradiated, and contralateral limbs to test our numbers against the literature. Furthermore, although we would compare ratios involving only femurs, we obtained data as well for tibias. Over the course of 3 weeks, samples were blindly tested and analyzed in the above procedure. Once each bone had the parameters, including the 1450 cm^{-1} peak, the identity key was presented and the bones could be separated into their respective categories. Below in Table 5.6 can be see the average of each parameter for the study for full femurs.

Table 5.6: Blind study results for Femur after separation into groups. (S(n=8), C(n=4), Irr (n=3))

Raman Parameter	Sham	Gong*	Irradiated	Gong	Contralateral
Mineral/Matrix	19.686 ± 1.420	15.21 ± 3.16	27.535 ± 4.026	16.99 ±2.71	19.451 ± 1.953
Crystallinity	0.047 ± 0.001	0.0571 ± .0005	0.0450 ± 0.001	0.0574 ± .0007	0.0461 ± 0.0001
Carbonate/ Mineral	0.179 ± 0.011	0.252 ± 0.024	0.190 ± 0.005	0.230 ± 0.025	0.1776 ± 0.011
Collagen Cross-Linking Ratio	2.660± 0.212	2.35 ± 0.18	2.846 ± 0.373	3.76 ± 0.41	2.2612 ± 0.4576
Depolarization Ratio of Mineral	0.606 ± 0.008	0.220 ± 0.067	0.584 ± 0.026	0.166 ± 0.029	0.5891 ± 0.01428
Depolarization Ratio of Collagen	0.477 ± 0.021	0.543 ± 0.054	0.459 ± 0.044	0.449 ± 0.039	0.3894 ± 0.02435
1450/958	0.565 ± 0.042	N/A	0.383 ± 0.006	N/A	0.4853 ± 0.03846
1450/1660	4.729 ± 0.292	N/A	5.2669 ± 0.405	N/A	4.5985 ± 0.4071

± is Standard Error (Standard deviation divided by the square root of N) for our data and standard deviation for Gong data.

It should be noted that data was also gathered for tibias from the same animals and this may be included in a later study but since we could not execute Marrow Cavity Evacuation (MCE) for tibias, the remainder of the thesis will focus on the femur data. For the most part the measurement results comprising this larger data set coincides with our original values from the preliminary data. Moreover, with the exception of the depolarization ratio of the mineral, these results are in agreement with the tibia results of the Morris group within statistical uncertainty.

As discussed above all disagreement is consistent with the fact that we obtain signal from deeper in the bones than that of the Morris Group. This is true partly because of the optics of our apparatus and simply because tibias are different in many ways than femurs e.g. thickness. Since we established that we went deeper, we executed MCE on the entire data set. Following the MCE study of the preliminary data, the 1450 cm^{-1} peak was included in the analysis of the full and empty bones as shown in Table 5.7.

Table 5.7. Average values for each Raman parameter after separation into groups. (S(n=8), C(n=4), Irr (n=3))

Raman Parameter	Sham	Irradiated	Contralateral
1450/958 FULL	0.5645 ± 0.04248	0.3827 ± 0.005636	0.4853 ± 0.03846
1450/958 EMPTY	0.2931 ± 0.01815	0.2167 ± 0.02422	0.19267 ± 0.01932
Change	0.2714	0.1659	0.2926
1450/1665 FULL	4.7290 ± 0.2918	5.2669 ± 0.4047	4.5985 ± 0.4071
1450/1665 EMPTY	5.7267 ± 0.5470	4.8567 ± 0.3935	5.2021 ± 0.8989
Change	-0.9978	0.4102	-0.6036

± is Standard Error (Standard deviation divided by the square root of N)

Removing material from a turbid object as in MCE reduces the source of associated Raman features. And if the propagation loss and/or trapping propensity of the object are modified due to the removed material, other Raman features associated with a different material may increase. The chances of observing an increase in a Raman signal because of removing a different material are increased when the material is removed, a void is created, because the scattering cross section of vacuum presents the minimum propagation loss. The shape of the object, the spatial distributions of the various component materials, and the geometry of the incident light and detection system must be specified to model the effect of a process like MCE on the ratios that have been used in characterizing bone. Future work could involve detailed models and properly account for propagation effects in comparing the same ratios as in “anatomically correct tissue phantoms”.

Presently to explore the relationship of full to empty, simple calculations were done to show the fractional change between the full bone and the empty bone. For a particular Raman feature we define fractional change using the equation below.

$$fractional\ change = \frac{full - empty}{full + empty}$$

This index varies from 0 to 1 depending on how much material is removed and it helps us to estimate what percentage of a material was removed using MCE with a careful analysis of the process. Based on the fractional amount of material removed and referring back to the above definitions and equations, we have:

$$fractional\ change = \frac{(R_{v1F} - R_{v1E})}{(R_{v1F} + R_{v1E})}$$

$$fractional\ change = \frac{(I \times [C_{1F}] \times RS_1 \times V_F) - (I \times [C_{1E}] \times RS_1 \times V_E)}{(I \times [C_{1F}] \times RS_1 \times V_F) + (I \times [C_{1E}] \times RS_1 \times V_E)}$$

Canceling out:

$$fractional\ change = \frac{([C_{1F}] \times RS_1 \times V_F) - ([C_{1E}] \times RS_1 \times V_E)}{([C_{1F}] \times RS_1 \times V_F) + ([C_{1E}] \times RS_1 \times V_E)}$$

And since we are comparing one Raman feature of a full bone to the *same* feature after MCE.

$$fractional\ change = \frac{([C_{1F}] \times V_F) - ([C_{1E}] \times V_E)}{([C_{1F}] \times V_F) + ([C_{1E}] \times V_E)}$$

Here the term $[C_{1F}]$ indicates the "concentration" or "volume fraction" of component 1 that gives Raman feature at ν_1 when the bone is "Full". So if a bone had been completely emptied of component 1, $[C_{1E}] = 0$ and this would give a fractional change of 1.0 as required to be a sensible index. Note that because of propagation effects, V_E may be greater than V_F, as exemplified in Figure 5.8, and this could allow the fractional change to be *less* than zero if V_E encompasses materials not included in V_F. But also, if $V_E \approx V_F$ then we would have:

$$fractional\ change\ in\ Raman\ signal = \frac{C_{1F} - C_{1E}}{C_{1F} + C_{1E}}$$

To see how this index behaves consider the first row of Table 3.8 in which no materials were removed that is:

$$F - E = 0$$

Table 5.8: Breakdown of Fractional Change in MCE

full [C_{1F}]	**empty [C_{1E}]**	**%Evacuation**	**(F-E)/F+E) = fractional change**
1	1	0	0
1	0.9	0.1	0.053
1	0.8	0.2	0.111
1	0.7	0.3	0.176
1	0.6	0.4	0.250
1	0.5	0.5	0.333
1	0.4	0.6	0.429
1	0.3	0.7	0.538
1	0.2	0.8	0.667
1	0.1	0.9	0.818
1	0	1	1

This can be expressed graphically (Figure 5.16) to show that there is a slight nonlinearity to this index but it does allow quantitative comparison of the effect of MCE on a basis normalized to the amount of material that was present before MCE while giving some idea of the effect of variable turbidity on propagation of the light during the measurement process.

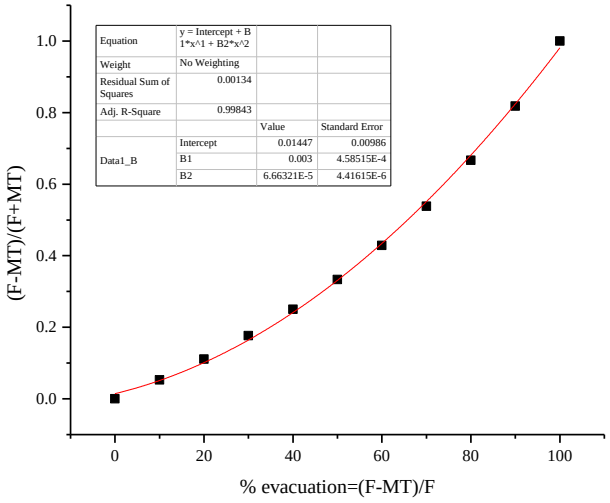

Figure 5.16. Graph of Fractional change in a Raman signal versus amount of contributing material removed during MCE assuming no change in the probed volume.

This was first done for each individual bone at each peak of interest, 958, 1070, 1450, 1660, and 1665 cm^{-1}. This was then plotted up as a function of the sample number to see any relationships. (Figure 5.17.).

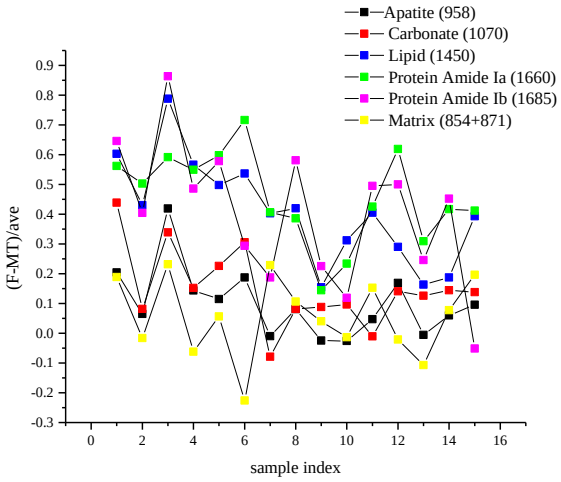

Figure 5.17. Fractional change of each Raman spectral feature across treatment groups (S, C, IRR) Note that there are only 15 samples due to the "empty" data from one of the irradiated bones being lost.

The Figure above shows that the fractional change after MCE for Raman features associated with compact bone ranges from 0 to 0.3 and is only less than 0 for some of the apatite, carbonate and matrix measurements. Moreover, it's much higher, ranging from 0.4 to 0.6, for the peaks associated to the lipid (1450 cm^{-1}) and amide I (1665 and 1680 cm^{-1}) than for the carbonate (1070 cm^{-1}) and apatite (958 cm^{-1}) peak. The matrix peaks (854 cm^{-1} and 871 cm^{-1}) are even lower. The change in the signal between the full and empty bone, in general is higher in the lipid and amide I peaks than in the carbonate, matrix and apatite. This leads us to believe that those signals are coming from the inside of the bone since cleaning out the bone has a much larger effect on those then on the carbonate and apatite which are contributing to the compact bone much more. There is some question as to why there is variation from bone to bone in terms of fractional change. We believe this is due to the size change in the bones. In our next study we will quantify the size of the bones and see if that can be used to normalize these curves.

Another potential question is whether the fractional changes were biased by the magnitude of the peak intensities themselves. Below however in Figure 5.18 it can be seen that carbonate, which has some of the lowest raw intensities of interest, and apatite, which has by far the highest intensities, still share roughly the same fractional change, thus proving that raw intensity does not sway the change patterns.

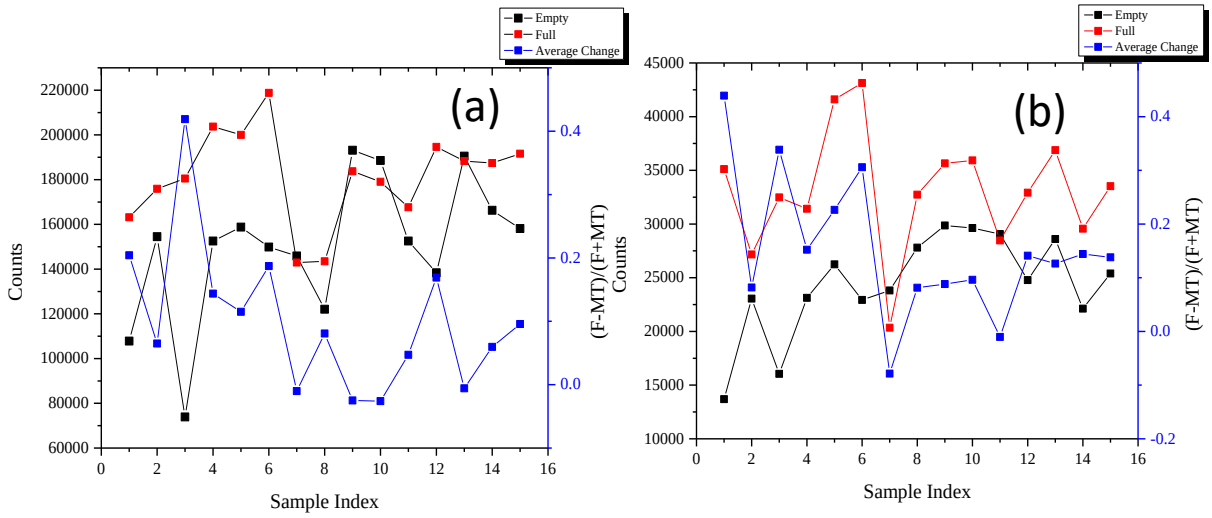

Figure 5.18. (a) Raw count of 958 cm^{-1} peak of both full (red) and empty (black) as well as average change (blue). (b) Raw count of 1070 cm^{-1} peak of both full (red) and empty (black) as well as average change (blue). This depicts that with a range of 80000 to 22000 counts for 958 cm^{-1} peak and only 15000 to 45000 counts for the 1070 cm^{-1} peak, the average change is unaffected by raw counts.

We then calculated the average fractional change for each peak across all treatment groups i.e. sham, contra etc., as well as the standard deviation, and the standard error. This was done to see if there was a statistically significant difference between the average fractional changes and zero. The closer a mean fractional change is to zero, the more likely nothing relevant to that Raman feature was removed during MCE, regardless of the treatment group. Table 5.9 depicts the calculated results. Using the standard deviations as a guideline, it is shown that the apatite and matrix values are not statistically different from zero, and that carbonate is very close to zero, that is, within one standard deviation they are equal to zero, but that the lipid, amide Ia, and Ib values are greater than zero.

Table 5.9. Fractional change in specific Raman features with Marrow Cavity Evacuation (MCE) of mouse femurs averaged across 3 groups (N=15) for Sham, Contra-lateral, and Irradiated.

Peak	Mean	Standard Deviation	Standard Error
Matrix	0.056	0.133	0.034
Apatite	0.102	0.120	0.032
Carbonate	0.152	0.137	0.037
Lipid	0.411	0.181	0.049
Protein Amide Ia	0.462	0.160	0.043
Protein Amide Ib	0.434	0.204	0.055

Finally, we group these values by treatment category i.e. sham, contra-lateral, and irradiated to see if any differences can be seen within the groups themselves. Below in table 3.10 we see the same Raman parameters, this time separated by treatment types.

Table 5.10. Mean fractional change separated by bone type (S(n=8), C(n=4), Irr (n=3))

	Matrix	Apatite	Carbonate	Lipid	Protein Amide Ia	Protein Amide Ib
Sham						
Mean	0.071	0.086	0.124	0.380	0.459	0.449
Standard Error	0.043	0.028	0.054	0.057	0.037	0.055
Contra-lateral						
Mean	0.012	0.196	0.238	0.563	0.602	0.535
Standard Error	0.095	0.078	0.057	0.078	0.043	0.124
Irradiated						
Mean	0.075	0.015	0.107	0.287	0.263	0.098
Standard Error	0.063	0.040	0.015	0.070	0.079	0.081

This data shows the data from the above table (table 3.8) broken down into type of bone i.e. sham, contra-lateral, irradiated and depicts a better image of exactly how much change occurs in each femur with MCE. Notice that all values are positive depicting a definitive decrease from full to empty. Notice also that the changes are much smaller for apatite and carbonate, across the board, than for lipid and the protein peaks. This suggests that roughly 50 percent of the contribution of the 3 peaks comes from the marrow in the cavity.

The other main point that can be seen from the data is the comparison of each peak between the three types of bones, to see if the change is actually significant. Below in Table 5.11 each comparison as well as the p- value can be seen, keeping in mind that a p-value of 0.05 or less means that that the difference is significant at 95% confidence.

Table 5.11. Statistical significance (p values) for relationship between mean fractional changes of each type (S, C, Irr,) relative to each other.

	Matrix	**Apatite**	**Carbonate**	**Lipid**	**Protein Amide Ia**	**Protein Amide Ib**
Sham Vs. Contra-lateral						
P Value	0.159	0.128	0.219	0.088	0.043	0.476
Significance	Not	Not	Not	Almost	Significant	Not
Sham Vs. Irradiated						
P Value	0.904	0.208	0.857	0.390	0.030	0.008
Significance	Not	Not	Not	Not	Significant	Significant
Contra-lateral Vs. Irradiated						
P Value	0.368	0.125	0.116	0.053	0.010	0.043
Significance	Not	Not	Not	Almost	Significant	Significant

This shows that the difference in the mean fractional changes for the matrix, apatite and carbonate are all insignificant between the three treatment types. Due to the process used, the lipid is “almost” significant at 95% confidence but it is significant at 91% confidence. The change in the protein however is significant across the board for the types, with the exception of protein amide Ib for sham vs. contra-lateral, with a much larger data set though, this could very well change.

The conclusion that can be drawn from this last table is that the change in apatite, carbonate, and matrix peaks between the three groups is roughly the same. The pattern that the mean fractional change follows in the lipid and protein peaks however, is that the irradiated change is smaller than the sham change which is smaller than the contra-lateral change.

One possible theory behind this behavior is known as the abscopal effect. An abscopal effect is the well-known phenomenon in radiotherapy cancer treatment where localized treatment is applied to a specific tumor and it not only affects the treated tumor but also, tumors distal to the treated region respond in a systemic effect. We believe that the reason the changes in the protein are so high in contra-lateral limbs is because when the bone is irradiated, the limb attempts to heal the damage by overloading the bone with fat. These cells have died however during the irradiation, so no fat is produced (hence the smaller change in the irradiated). This same response however also occurs in the non-irradiated contra-lateral limb though and because those cells in the marrow have not been killed, the untreated limb bone also fills with fat. Thus, when MCE occurs, more lipid material is present and sucked out during MCE.

5.3.4 Depolarization Modeling in a Turbid Sample

To show the effect of turbidity on depolarization ratios, the depolarization ratio for the totally symmetric band (461 cm^{-1}) of carbon tetrachloride was measured while intentionally changing the turbidity by adding quartz spheres. This depolarization ratio[94] is roughly 0.005 for gas phase CCl_4 and using our instrument with laser excitation having an intrinsic polarization ratio of 50:1 i.e. a depolarization ratio of 0.02, the lowest ratio we obtain for neat CCl_4 is in fact 0.02. Figure 5.19 below depicts the effect of a 100-fold variation of the volume fraction of quartz spheres added to a CCl_4:CBr_4 mixture. As expected, this caused an increase in the depolarization ratio ultimately leading to an effective "leveling off" of the depolarization ratio around 0.04. Initial addition of quartz spheres appears to show a jump in depolarization ratio, i.e. less signal from the parallel polarization. This initial jump quickly stops though effectively limiting the upper limit of the depolarization ratio. If we assume that to be a *factor* of 2.5 scale up from the original and translate that ratio to our measurement of the depolarization ratio of the mineral, the ratio we

measured, roughly 0.6, becomes much closer to the ratio Gong obtained, 0.21, which scales up to 0.53. Dr. Goodisman modeled the same experiment through a radiation transfer equation calculation and it follows our trend nicely with an effective "leveling off".

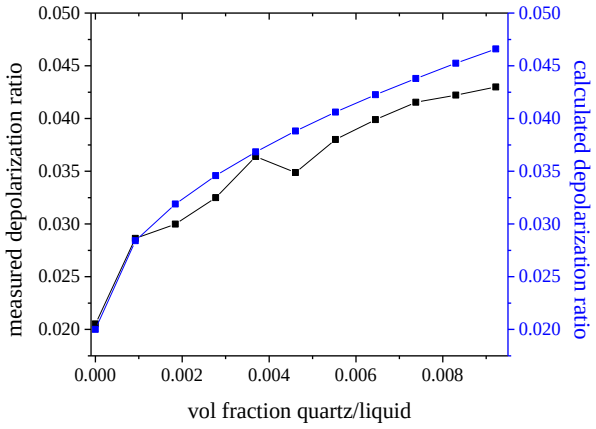

Figure 5.19: depiction of increasing the turbidity of CCl_4:CBr_4 by addition of quartz spheres(black). The depolarization ratio effectively "levels off" at roughly 0.4. Dr. Goodisman modeled the same experiment (blue) There was no optimization of parameters in this simulation and the only adjustable parameter was the average polarization shift per scattering event of 0.0008.

5.4 Discussion& Future Work

Preliminary studies were done on mouse tibias and femurs to test for replication of previous work done by Gong et. al. Results show that for most of the data, the values are consistent. This is corroborated by a blind study done later with different categories of femurs. Major areas of disagreement include values corresponding to the carbonate and apatite polarization ratios. Through studies of a new lipid peak at 1450 cm^{-1} it was determined that our optical probe penetrates the bone deeper than that of the Gong group. Such penetration causes the skewed values due to elastic scattering randomizing the polarization of the incoming and outgoing laser and Raman scattered light respectively.

A new technique was established to further study the effects of the inside of the bone known as Marrow Cavity Evacuation (MCE). MCE showed multiple effects. In original studies it confirmed the thought that our laser probed deeper in the bone than the Gong group. It also aided in determining which peaks from the spectrum are from the marrow and which are from the compact bone between the marrow cavity and the outside surface.

A second study was done with three types of bones, sham, contra-lateral and irradiated. The bones were tested and then separated into respective groups. The mean fractional changes were only different from zero with respect to the standard deviation calculations for materials that could be reasonably assumed to be localized in the marrow cavity i.e. lipid and protein. Mean fractional changes after MCE validated the Raman feature assignments originally proposed by the Morris Group long ago. MCE also showed that there was significant ($P<0.05$) differences between the three treatment groups, especially in the marrow of the bone.

This change also showed a possible abscopal effect i.e. after treating a localized part of the body with e.g. chemotherapy or radiation therapy, there is a systemic reaction in the body and other locations can be affected as well. The amount of fat and protein in the contra-lateral limb was much larger than that of the sham and even more than the irradiated. We believe this is due to the contra-lateral limb responding to this reaction to the radiation, but unlike the irradiated bone, where cell death causes an inability to react to these responses, the cells in the contra limb marrow cavity still have the capacity to react accordingly.

Lastly, the turbidity of the system was modulating by varying the amount of quartz spheres in a CCl_4 solution and a computer calculated simulation was compared. It would appear that both the solution and simulation show that there is a limit to the depolarization ratio that can be achieved by any system, as symbolized by a "leveling off" of the ratio as the system becomes more and more turbid.

Much work still needs to be done on bone. Larger data sets will need to be produced to further the significance testing of each MCE group. The first set of MCE that was done did not include polarization ratios. We suspect that MCE would aid in putting our value for depolarization of mineral closer to that of the Gong paper.

Once we have an established protocol for what we are looking for in the Raman of these bones, further investigation of both the structural aspects as well as the physiological responses of the bones to stress and manipulation must be done. Fracture toughness tests could be done to determine the stress required to fracture the bones at specific time points post-radiation. Long range we hope that Raman spectra can be used clinically to assess the vulnerability of bones post radiation treatment.

We also aim to better quantify the contents of the bone. There are many ways this can be done, one of which is to find things in which only the fat would dissolve and the protein would stay in the bone or vice versa. This would allow us to better associate the observed Raman features with specific lipid and protein materials. We could also find a way to use the marrow that is sucked out of the bone cavity. If we could scale up the marrow, through some form of dilution possibly, we could attempt to quantify certain parts of it. We could also attempt methods such as UPLC to try and detect and quantify certain components of the marrow, as other groups have already successfully done with collagen.[103]

Also, this idea of the abscopal effect needs to be further explored. Work is currently being done in Sweden where a group is using a photoplethysmographic technique to shine light into a patella and assess blood flow in the bone tissue.[104] We aim to replicate this study and test it, potentially on a human, where a location, distal to the patella, has been treated with radiotherapy. If we could see a change in the blood flow inside the knee from a person receiving radiation treatment distal to the knee that isn't seen in a person not receiving treatment, it would be very significant in establishing the existence of an abscopal effect in a particular situation.

Lastly, we have shown that there is a sort of "non-linearity" in the relationship between the turbidity of a sample and the depolarization ratio, both in experimental and simulation studies. This phenomenon needs further studying, possibly with a change in the concentration of quartz spheres or even possible extending the current calibration as well as more simulations run to see if the behavior appears to remain.

5.5 Conclusion

We extended the work of the Morris group at UMICH by creating a Raman system similar but not identical to theirs. This system could perform the measurements they did with results that are either identical to theirs or consistent with theirs based on the known differences between the Raman systems used. We furthered studies of radiation damage to bone by comparing three separate treatment types of femurs, sham, irradiated, and contra-lateral. MCE was established as a viable technique for differentiating Raman features for different locations in bone. Using this approach, we may have observed an abscopal effect. Future work will involve more work with both femurs and tibias as well as correlating Raman measurements to toughness tests to assess bone strength as well as gaining a better grasp on the behavior of depolarization ratios in relation to both probing depth and turbidity.

6. Conclusions

There were four hypotheses studied in this thesis:

2. **Mapping Spinal Cord Injury:** This study will also introduce the idea of using spectroscopy as a tool for doing label-free, chemically sensitive optical profilometry of cords, and what that can tell us chemically and physiologically about injuries. It will also use new calculations and assignment of peaks to observe pH changes and differences as a way of explaining physiological response.
3. **Spinal Cord Injury inflammation in the immediate stage:** We aim to continue the work previously done in lab though instead of long time point *ex vivo* examination of cords we will be looking at immediate (30 mins- roughly 5 hours) time points of a cord *in vivo,* still intact in a living rat.
4. **Mammalian cell cultures:** We aim to measure metabolic activity, nutrient consumption and production of waste, non-invasively. This multi-step approach will first include medium studies and conclude with a study of a culture, through a closed culture flask.
5. **Irradiated vs control bone composition and physiology:** We aim to continue the work of the Morris lab by investigating the physiological response of bones after radiation while also looking at their contra-lateral counterparts to see any of the same behavior.

First, we studied the early reaction of the body to a spinal cord *in vivo* in rats. We used line scans to show this process could be used as a method of optical profilometry of cords. These studies showed a difference in the apparent Hct, or fluorescence change between control and injured cords that could aid in earlier determination and location of injury. More mapping studies need to be done though to attain statistical significance.

We also used PV[O]H as a potential clinical tool for assessing and understanding the chemical processes of spinal cord injury. While conducting line scans of the cords we were able to attain Raman spectra indicative of chemical responses to the injury as well as phosphorylation that were significantly different statistically between injured cords and control cords. We were able to identify peaks corresponding to phosphate in these spectra and measured early pH change calculations from this data.

As it pertains to mammalian cell culture, it appears possible to non-invasively track the metabolic activity of cultured cells without disruption of the cells themselves, through means of Raman Spectroscopy as a test of viability. Preliminary results showed success in the ability to monitor glucose uptake and polysaccharide production using only medium where cells had previously been cultured. Studying different cases, we successfully showed that glucose concentration can be measured, with 95% confidence, down to 10 mM concentrations and likely below without physically sampling the culture. An attempt at data collection through the flask *in vivo* was attempted and with more precision of our apparatus and approach data on glucose consumption could be achieved.

In the last hypothesis we hoped to probe the physiological response to irradiated bones. We successfully extended the work of the Morris group at UMICH by creating a Raman system similar, but not identical, to theirs. This system could perform the measurements they did with results that are either identical to theirs or consistent with their results based on the known differences between the Raman systems used. We did further studies of radiation damage to bone however by comparing three separate treatment types of femurs, sham, irradiated, and contra-lateral. The MCE technique was established as a viable technique for differentiating

Raman features for different locations in bone. Using this approach, we may have observed an abscopal effect.

We set out to use spectroscopy to probe living systems non-invasively. These four separate, non-traditional, sample sets and conditions show that spectroscopy can in fact be used and give valuable chemical and physiological data on systems that are not easily measured without disrupting the system.

7. Appendix A: Approved Live animal IACUC Approval

A signed copy is available on record in the Syracuse University LAR.

SYRACUSE UNIVERSITY ANIMAL CARE AND USE COMMITTEE LIVE VERTEBRATE ANIMAL USE PROTOCOL REVIEW FORM

The mandate of the IACUC is to provide for the proper and humane treatment of vertebrates in research and teaching and, consistent with good practice, to minimize the numbers used. Questions on this form are designed to provide information that will help the committee meet these goals.

Please refer to the IACUC Protocol Submission Procedures for deadlines. IACUC approval is for a maximum of 3 years, renewable annually.

1.TITLE OF THIS PROTOCOL: In vivo Raman spectroscopy of acute spinal cord injury in female rats
2.PRINCIPAL INVESTIGATOR: Julie M. Hasenwinkel

(This person must be faculty staff, or a student with a faculty member as a Co-PI)

Home phone (for emergencies) :315-450-3825	**Work phone**:443-9410
Department: Biomedical and Chemical Engineering **E-mail**: jmhasenw@syr.edu	
Co-Principal Investigator: Joseph Chaiken	

Home phone (for emergencies): 315-415-4784	**Work phone**:443-4285

Training Certificates submitted with this application? Yes: No: **X**

3.OTHER PERSONNEL INVOLVED:

Name	Contact in emergencies work	Contact in emergencies home	TrainingCertificates submitted? Yes/No
Kyle Bishop	845-514-0326	845-514-0326	No
Alex Janini	856-469-1094	856-469-1094	No
Sandra Hewett	860-212-1378	315-314-7860	

4.PROPOSED USE OF LIVE ANIMALS: Note: this protocol form is for use of live vertebrate animals. If you plan to use cadavers, body parts or blood obtained from other sources, do not use this form. Call 443-3013 or visit the web site h ://sumweb.syr.edu/os /iacuc.html for the Animal Products Protocol form.

Research: **Yes**	Classroom Teaching:
Present or Potential Source of Funding: Present	

Agency and Title of Grant Proposal: New York State Department of Health, Institutional Support for Spinal Cord Injury

Course Number and Title: N/A

5.PROPOSED ANIMAL USE PERIOD:

Note that IACUC approval is for a maximum of 3 years, renewable annually. Include the proposed project period below (be aware that the project period will begin on the date the protocol receives final approval).
From:**3/10/16** To:**3/9/19**

6.APPENDICES CHECKLIST

YES	**X** NO	Does the proposed use of animals involve collection from natural habitat? If YES, please attach copies of permits from federal, state and any other authorities.
X YES	NO	Does the proposed use of animals go beyond simple observation? If YES, complete Appendix 1. If NO, do not complete the remainder of this checklist or any of the Appendices (go directly to 7. Lay Description and complete the application to section 13, Faculty /PI Assurance Statement.
X YES	NO	Does the proposed use of animals involve surgery or blood collection? If YES, complete Appendix 2.
YES	**X** NO	Does the proposed use of animals involve radioactive materials? If YES, complete Appendix 3a and attach a copy of the Approval Letter from the Radiation Committee.
YES	**X** NO	Does the proposed use of animals involve infectious agents? If YES, complete Appendix 3b and attach a copy of the Approval Letter from Biological Health and Safe
YES	**X** NO	Does the proposed use of animals involve known carcinogens or toxic chemicals? If YES, complete Appendix 3c and attach a copy of the Approval Letter from Biological Health and Safe

7.LAY DESCRIPTION

Please provide a succinct description of the proposed research or teaching which can be read separately from the remainder of the protocol by a non-scientist. Use of highly technical terms will cause delay. The description should include all proposed use of animals.

Injury to the spinal cord usually results in the formation of a glial scar, composed primarily of star-shaped cells called astrocytes. This scar is a barrier to nerve regeneration and functional recover after injury, largely due to the presence of inhibitory molecules like chondroitin sulfate proteoglycans (CSPGs) produced by astrocytes. Cell death and the loss of the insulating myelin sheath from surviving neurons also contribute to the loss of sensory and motor function. These changes in the cellular and biochemical composition of the spinal cord tissue begin immediately following injury.

Raman spectroscopy is a powerful non-destructive method for monitoring biochemical changes in tissue in the native state, without the need for fixation and staining. Raman spectroscopy has been successfully used to detect cancerous tissues non-invasively, plaques in cases of myocardial infarction, and various other biochemical markers specific to particular tissues, cells, and extracellular matrix molecules. It has been used to study a variety of tissue types, including skin, brain, spinal cord, lungs, liver, and cartilage, and identify the life cycles of single cells. We have used Raman spectroscopy to study temporal biochemical changes in rat spinal cord tissue following in vivo injury and ex vivo injury of tissue slices. In both cases, the tissue was extracted from the animals and tested outside of the body. In this prior work, we have been able to detect and quantify changes in CSPG concentration and other markers for demylenation and cell death.

We hypothesize that Raman spectra can be acquired from living animals, both before and after spinal cord injury (SCI), allowing us to monitor concentrations of physiologically relevant molecules in real time, as they are synthesized and degraded following injury. We propose to study these changes in the acute period immediately following SCI (first 5 hours). Biochemical changes in live tissue during this time periods following SCI have never been reported. Results from these experiments can be correlated with post-mortem histological data to confirm the presence and spatial distribution of relevant biological molecules and cells. Currently, there are no methods in the literature or clinical practice that demonstrate in vivo monitoring of SCI with Raman spectroscopy or are able to detect the types of changes we believe we can measure in a non-destructive manner. Raman spectroscopy has significant potential as an in vivo, non-invasive diagnostic technique for monitoring both the progression of SCI and the effect of treatmens in real time. This would be an extremely beneficial tool in laboratory research and could potentially be developed as a clinical tool.

In addition, the animals used in this study will also serve as a source of spinal cord tissue for additional ex vivo experiments to study the cellular, biochemical, and micromechanical properties of spinal cord tissue before and after injury. The glial scar has also been hypothesized to be a mechanical barrier to regeneration, presumably by increasing the stiffness or the viscosity of the spinal cord tissue; although, to date, scant published data exists on the mechanical properties of the glial scar. One reason for a lack of data in this area lies in the difficulties associated with measuring mechanical properties of such soft biological materials. Additionally, in order to measure the mechanical properties of the glial scar specifically, such measurements need to be made with a very fine spatial resolution. We have established a culture method in our laboratory that allows us to maintain viability in 400 micron thick slices of spinal cord tissue ex vivo for two weeks. We have also establised a method in our laboratory for producing an injury in slice cultures of spinal cord tissue. We will use the slices to measure mechanical properties of the tissue on a micron scale and to observe the behavior of astrocytes within the spinal cord tissue over time. Indentation testing will be performed with an indenter tip that is 500

microns in diameter. Live cell imaging will be performed with fluorescence microscopy. Raman spectroscopy will also be performed on tissue slices ex vivo to compare with data obtained in vivo, where the injury environment is more complex. These experiments should allow us to elucidate mechanisms that regulate glial scar formation following spinal cord injury and determine the feasibility of our slice culture model as a surrogate for in vivo studies.

In order to create a reproducible and consistent spinal cord injury in rats, we will be purchasing a MASCIS impactor from the W.M. Keck Center for Collaborative Neuroscience at Rutgers University. PI Hasenwinkel and other lab personnel will attend a three-day training workshop to learn the surgical procedure and how to operate the device. The first step in this project will be to perform a pilot study to demonstrate that we are able to produce mild and moderate injury in rats. Once these procedures are well established in the Hasenwinkel lab, the rest of the studies can proceed.

The specific aims of this research are:

1. To determine the biochemical changes in spinal cord tissue in real-time, immediately following injury by acquiring Raman spectra for five hours.
2. To determine the micromechanical properties of spinal cord tissue in the injured and uninjured state.
3. To track live cell behavior and biochemical changes in injured and uninjured spinal cord tissue using Raman spectroscopy and fluorescence imaging.

8. RATIONALE: Please answer each of the following separately

8.1) What value or potential contribution to science or human welfare may result from this work?

The in vivo, real-time, spectroscopic characterization of healthy and injured spinal cord tissue has not yet been reported in the literature, nor have studies of biochemical changes in spinal cord tissue immediately following SCI using non-destructive techniques. If successful, this technique could be extremely useful in future animal studies of SCI as a method to monitor tissue changes after injury and upon treatment. The ability to collect spectra repeatedly over time from a single animal could significantly reduce the number of animals needed in future studies. Additionally, the data collected from ex vivo micromechanical, cellular, and biochemical analysis of spinal cord tissue is expected to provide a new perspective on the microenvironment of the glial scar.

Federal policies require you to address **replacement**, **reduction**, and **refinement** as alternatives for animal use.

8.2) (**Replacement**) Please give detailed reasons why vertebrate animals are necessary.

The study of spinal cord injury can only be undertaken in vertebrate animals.

8.3) (**Replacement**) Please give detailed reasons why this vertebrate is the most appropriate species.

The rat is the animal most frequently used in models of SCI because of size and accessibility, and also since the morphological, biochemical, and functional changes that occur after SCI have been found similar to those seen in humans (Metz et al., 2000; Norenberg et al., 2004; Onifer et al., 2007).

8.4) (**Reduction**) Please give detailed scientific (research) or pedagogic (teaching) reasons why the number of animals is the fewest possible.

A power analysis was performed to determine the number of animals for the studies outlined in this protocol. It was determined that 5 animals per experimental group is the minimum number necessary for statistical power, given the expected variability in the Raman spectra and using an alpha value of 0.05 and a beta value of 0.01. We are also using tissue from animals that are part of the in vivo Raman spectroscopy study to generate organotypic slice cultures, so no new animals are necessary for the ex vivo portion of the proposed work. A total of 40 animals are necessary to complete all experiments.

8.5) (**Refinement**) Indicate which category(s) your protocol comes under per USDA definitions:

_____Category C: No pain, distress or use of pain-relieving drugs.

__X__Category D: Pain or distress for which appropriate anesthetic, analgesic, or tranquilizing drugs are used.

_____Category E* : Pain or distress for which use of anesthetic, analgesic, or tranquilizing drugs would adversely affect the procedures, results, or interpretations.

Key words for Medline/Pubmed/Scopus search: spinal cord Raman spectroscopy, in vivo Raman spectroscopy, microindentation spinal cord, live cell tracking spinal cord, glial scar mechanical properties, organotypic slice cultures spinal cord (2006-2010). Date searched: 2/1/16

Category D Justification

l) Survival Surgery:

The data cannot be obtained using a non-animal alternative since the basic objective of the study is to characterize rat spinal cord tissue. We have proposed a pilot study which will establish this injury model in our hands. The numbers proposed here are the maximum numbers of animals that will be used and all efforts will be focused on reducing the total number of animals used. The procedure used to produce a spinal cord injury is a contusion injury model. This model is a common one in the spinal cord injury literature and is relevant for the research trajectory of the Hasenwinkel laboratory.

2) Non-Survival Surgery:

Raman spectroscopy in the acute stage of injury: The data cannot be obtained using a non-animal alternative since the basic objective of the study is to characterize rat spinal cord tissue. The numbers proposed here are the maximum numbers of animals that will be used and all efforts will be focused on reducing the total number of animals used. Additionally, tissue from animals used in this study will be used for all ex vivo studies, thus maximizing the use of each animal in the research plan.

For protocols in either Category D or E the narrative for refinement must provide the methods and sources used to determine that alternatives were not available. The minimal written narrative as stated in USDA Policy #12 should include: (a) the databases searched or other sources consulted, (b) the date of the search, (c) the years covered by the search, and (d) the key words and/or search strategy used by the Principal Investigator when considering alternatives. Include descriptions of other methods and sources used to determine that no alternatives were available to painful or distressful procedures.

Possible databases include, but are not limited to: MEDLINE, TOXNET, AIDSLINE, CANCERLIT, CURRENT RESEARCH INFORMATION SERVICE (e.g., Current Contents, Index Medicus) and ANIMAL WELFARE INFORMATION CENTER (National Agricultural Library, 301-504-5755 or 5756).

* Please note: The Principal Investigator may be requested to attend the IACUC meeting to discuss the proposed research when a) Protocol falls into Category E

9. THE PROPOSED PROTOCOL: This is the place to describe the specifics of your use and care of animals in detail. Address all of the issues listed below.

9.a) Experimental design. What is the hypothesis to be tested or the question to be addressed (include citations)? Describe analysis methods and refer to the details for data analysis designed to minimize number of animals provided in section 8.4) (Reduction). For teaching protocols, describe how students will analyze data and append course materials detailing teaching goals and instructions for students.

The work outlined in this protocol relies on our ability to create consistent and reproducible spinal contusion injury using the MASCIS impactor. Therefore, Study 1 will be a pilot study (see attached flow chart), performed to establish this technique in the Hasenwinkel laboratory following training of key personnel (Hasenwinkel, Bishop, and Janini) at the W.M. Keck Center for Collaborative Neuroscience at Rutgers University. In the pilot study we will have three groups: 1) mild contusion injury, 2) moderate contusion injury, and 3) sham control. The contusion injury is created by dropping a weight of 10 grams from a specified height, using the impactor system. The magnitude of the height determines the severity of the injury, with 12.5 mm corresponding to a mild SCI, 25.0 mm corresponding to a moderate SCI, and 50.0 mm corresponding to a severe SCI. Moderate injury is the most commonly used model and in the pilot study we will test whether we can distinguish between mild and moderate injury using a combination of locomotor behavior scoring (BBB score, see next paragraph) and histological analysis. Due to a naturally recovering reflex in rats, even spinal cord injured rats regain their ability to walk within the weeks following injury. For this reason, data collected from SCI rats generally improves for the first few weeks, then plateaus at some value, which is indicative of the extent of permenant damage. Therefore, the survival time for the pilot study will be 4 weeks to ensure that we can accurately assess the repeatability of this injury model in our hands prior to any experimental work.

Post-injury locomotor behavior will be assessed via the Basso, Beattie and Bresnahan (BBB) locomotor scale method (Basso et al., 1995). The scale (0 - 21) represents sequential recovery stages and categorizes combinations of rat joint movement, hindlimb movements, stepping, forelimb and hindlimb coordination, trunk position and stability, paw placement and tail position. A score of 0-7 corresponds to isolated joint movements with little or no hindlimb movement; 8-13 corresponds to intervals of uncoordinated stepping; and 14-21 corresponds to forelimbe and hindlimb coordination. BBB scores will be assessed every four days post-operatively by trained lab personnel.

We will use 5 animals in each of the three groups in the pilot study. Severe injury will not be used in the pilot study because typically animal care is quite difficult to manage following severe injury due to neurological deficits. Female rats will be used in all experiments because they have fewer bladder issues with this type of neurological deficit compared to male rats.

In order to accomplish the specific aims outlined in Part 7 of this protocol, we will answer the following research questions in Study 2 (see attached flow chart):
1. Are there any observable changes in spinal cord tissue due to long term exposure (5 hr), with or without acquisition of Raman spectra?

Two control groups will be used in Study 2 to determine the effect of long term exposure of the spinal cord to the ambient environment and to Raman spectroscopy (n=5 per group). Histological analysis will be performed on the tissue samples from these groups and compared with the histological analysis of tissue sections from the sham control in Study 1 (no exposure to the ambient environment or Raman). A comparison of these three groups will allow us to see if there are any deleterious effects on

the spinal cord tissue due to the experimental procedure we have developed for in vivo Raman spectroscopy.

2. What biochemical changes occur in spinal cord tissue during the acute period following contusion injury and do they vary as a function of the severity of injury?

We will have three injury groups (n=5 per group): mild, moderate, and severe. Each group will receive a contusion injury by compression of the spinal cord using the MASCIS impactor. Immediately following the delivery of the injury, biochemical changes in the tissue will be monitored using Raman spectroscopy, as described in Part 9b.

For the analysis of the Raman data, average spectra from control group 2 (no injury + 5 hr Raman spectroscopy) will be subtracted from spectra obtained from injured animals in order to account for any changes in the tissue simply due to Raman spectroscopy or exposure to ambient conditions. Spectra from the three injury groups will be compared and analyzed to determine changes in specific peaks that correspond to expected changes in spinal cord tissue, based on previous work in our lab. We will also identify any additional peaks that are changing in the sample spectra and determine the molecular origin of these changes. We will also perform histological analysis of the injury site following euthansia and compare across groups and agains the controls.

3. Do ex vivo biochemical properties, as measured by Raman spectroscopy, correlate with the biochemical properties measured in vivo?

At the conclusion of the in vivo work, spinal cord tissue will be harvested from the animals in the study and used to generate organotypic slice cultures. Tissue from the in vivo injury site will be used for histological analysis, but tissue from thoracic segments adjacent to the injury site (T8 and T10) and from control animals will be used to study biochemical changes induced after an ex vivo injury is created, using an established weight-drop model in the Hasenwinkel lab. Raman spectra will be acquired from the slices over the course of two weeks in culture and these spectra will be compared to those obtained in vivo following contusion injury. Spectra from uninjured controls will be compared with the spectra from in vivo controls. The potential advantage of this approach is that a large number of sections can be obtained from a single animal. If results from this study correlate well with changes measured in vivo, an ex vivo platform might be suitable for early testing of therapeutic molecules designed to treat SCI, thus reducing the number of animals needed in future work.

4. Do ex vivo micromechanical properties correlate with cellular events (migration and/or proliferation of astrocytes at the injury site) and histological changes in the tissue upon injury?

Additional tissue slices from the harvested tissue will be used to study the micromechanical properties of injured spinal cord tissue and the behavior of astrocytes in the sections following injury using Raman spectroscopy and live cell tracking, respectively. Tissue will be injured using a custom-designed slice impactor in the Hasenwinkel lab. Raman spectroscopy and live cell imaging will be performed over the course of two weeks on injured slices and uninjured controls. Sections will be fixed in 4% paraformaldehyde following testing and histological analysis will be performed. These experiments will be the foundation for exploring mechanobiological regulation of glial scar formation.

9.b) Provide a step-by-step description of what will happen to the animals. Include where the animals will come from and their past history (including age and prior treatment), where the work will take place, and who will be directly working with the animals. For teaching

protocols, include how the students will be involved in working with the animals. Describe what will happen to the animals after the project is finished. How and where will the animals be euthanized and by whom?

Study 1-Pilot: Female Sprague-Dawley rats will be ordered from Charles River Laboratories Inc. and housed in the animal facility for rats in the LSC vivarium. Female rats at an approximate age of 77 days will be used to be consistent with other experiments previously performed in our laboratory using a spinal cord injury model. The animals will be housed in shoebox cages (3 per cage) for a minimum of seven days to allow for acclimation. At the time of an experiment, a single animal will be transported live from the vivarium in LSC to room 0-021 CST in an appropriate carrier or alternatively, the MACSIS impactor will be moved to the LAR surgery suite and the procedure will be perforomed there. The rat will be initially anesthetized with Ketamine and Xylazine (80 mg/kg and 10 mg/kg, respectively, prepared by the Hasenwinkel lab) and the body temperature will be maintained using a temperature controlled heating pad. Surgery will use aseptic technique. Surgical mask, sterile gloves, and autoclaved instruments will be used during surgery. The skin over the upper thoracic area will be shaved and cleaned with a Betadyne solution. The skin will be incised, and then the connective and muscle tissue will be bluntly dissected to expose T9. A T9 laminectomy will be completed, taking care not to damage the spinal cord during the dorsal lamina removal. The rat will be positioned on the MASCIS impactor and either a mild or moderate injury will be created by dropping a 10 gram rod onto the exposed cord from a height of 12.5 or 25.0 mm, respectively. The MASCIS impactor also measures movement of the spinal column at the impact site, displays the trajectory of the falling rod, and measures the impact velocity (ImpV), cord compression distance (Cd), cord compression time (Ct), and cord compression rate (Cr). These impact parameters correlate with each other and spinal cord lesion volumes (estimated from tissue Na and K concentrations) and locomotor recovery (BBB scores). Homeostasis will be achieved by apposing Gelfoam pellets soaked in a dilute thrombin solution at the lesion site, which will then be removed before closing the lesion in layers with individual sutures. All control animals will receive a laminectomy but no contusion will be performed on control animals.

After surgery, the rats will be kept warm with the aid of a heating bulb and checked every 15 minutes until muscle tone and righting reflexes have recovered. After recovering from the anesthetic, rats will be returned to the LSC vivarium and housed separately until sutures are removed (1 week) and then 3 per cage. Post-operative buprenorphine (0.5 mg/kg, subcutaneous) will be administered twice daily for two days. Animals will be monitored by the lab daily for 3 days post-operatively to determine whether or not there is return to normal behavior (i.e. eating, drinking, activity). Surgical incision sites will also be observed during this time frame for clinical signs of infection or suture breakdown, including abnormal swelling, redness, and exudate from the wound. In case of any infection, animal care staff will be notified immediately. With this type of injury, bowel and/or bladder shock is uncommon but a low roughage diet will be fed to these animals for the week prior to and post surgery as an additional precaution as well as urine will be expressed twice daily if necessary. Autophagia may also occur infrequently. If this is a problem, animals will be coned to decrease access to the caudal part of the body.
After the first 3 days, lab personnel will perform exams every 2 days for the remainder of the survival time. Animals will be monitored for behavioral signs of pain or distress including weight loss, absence of movement, and guarding of the injury site. Animals exhibiting these signs will be attended to and given pain relief or euthanized with the guidance of animal care staff or consultation with the attending veterinarian.

Locomotor behavior of rats will be observed and quantified using the well-established BBB scoring system every 4 days. At 4 wks the rat will be euthanized with an intraperitonial overdose of sodium pentobarbital (Fatal Plus, 390 mg/ml; 0.5 cc) and sacrificed when deeply anesthetized by vascular

perfusion of saline (550-600 ml) followed by 4% paraformaldehyde for histology. Deep and terminal anesthesia will be indicated by the lack of reflexes at the top inch of the tail or hindlimb and slow or arrested respiration. Paraformaldehyde waste will be collected and stored in a laboratory SSA in compliance with the SU Hazardous Waste Program. Other waste from the perfusion process will be disposed of in the sink with appropriate dilution through rinsing. Tissue segments will be immediately frozen for immunohistochemistry. All animal carcasses will be collected, bagged, and frozen in 0-021 CST until materials are removed by EHO for disposal. PhD student Kyle Bishop will be primarily responsible for all procedures in the pilot study. He will be assisted by Dr. Chaiken, Dr. Hasenwinkel and PhD student Alex Janini.

Study 2 - In vivo Raman spectroscopy and ex vivo characterization of harvested tissue: Female Sprague-Dawley rats will be ordered from Charles River Laboratories Inc. and housed in the animal facility for rats in the LSC vivarium. Female rats at an approximate age of 77 days will be used to be consistent with other experiments previously performed in our laboratory using a spinal cord injury model. The animals will be housed in shoebox cages (3 per cage) for a minimum of seven days to allow for acclimation. At the time of an experiment, a single animal will be transported live from the vivarium in LSC to room 0-021 CST in an appropriate carrier. The rat will be anesthetized with Urethane (1000 mg/kg IP) which is an appropriate anesthetic for long term (5 hr) non-survival procedures. Body temperature will be maintained using a heating pad and blood pressure will be monitored over the course of the procedure using a pressure monitor developed by co-PI Chaiken. Surgery will use aseptic technique. The skin over the upper thoracic area will be shaved and cleaned with a Betadyne solution. The skin will be incised, and then the connective and muscle tissue will be bluntly dissected to expose T9. A T9 laminectomy will be completed, taking care not to damage the spinal cord during the dorsal lamina removal. Initial Raman spectra of uninjured spinal cord will be acquired for each animal immediately following laminectomy as described below. For the SCI groups, the rat will be positioned on the MASCIS impactor and either a mild or moderate injury will be created by dropping a 10 gram rod onto the exposed cord from a height of 12.5, 25.0 mm, or 50 mm, respectively.

Raman spectra will be acquired using a special proprietary fiber coupled optical probe for the Lambda Solutions RS1 Raman spectrograph, that was designed (a collaboration between Lambda Solutions and LighTouch Medical, Inc.) for transcutaneous use with rats to obtain RS with 830 nm excitation. This probe has been demonstrated to produce spectra from within 1-5 mm of the tissue surface. The probe does not require contact with the tissue surface and has a microscope based system for precise and accurate placement and repeatability. We can acquire spectra by placing a probe on the back of the anesthetized animal or in close proximity without actual contact. Spectra will be acquired for all animals in the injury groups periodically for 5 hrs to measure biochemical changes in the spinal cord tissue in the acute phase of the injury. Tissues will be rehydrated with saline during testing if necessary. Two control groups will be used and both will receive a laminectomy but no contusion injury. One control group will receive exposure of the spinal cord for 5 hr following laminectomy with no Raman spectroscopy. The other control group will be tested with Raman spectroscopy periodically for 5 hrs.

All animals in this study will undergo non-survival procedures. At the conclusion of the 5 hr period of data collection, animals will be euthanized with an intraperitoneal overdose of sodium pentoparbital (Fatal Plus, 390 mg/ml; 0.5 cc) and sacrificed while deeply anesthetized by vascular perfusion of saline (550-600 ml). Deep and terminal anesthesia will be indicated by the lack of reflexes at the top inch of the tail or hindlimb and slow or arrested respiration. Waste from the perfusion process will be disposed of in the sink with appropriate dilution through rinsing. Un-fixed tissue will be extracted and sliced in the transverse plane into 400 micron thick slices for organotypic culture using a tissue chopper.

Cultures will be transferred to 422 Bowne Hall in sealed containers and maintained in an incubator. Specimens will be transported in the same manner to 403 Bowne Hall and to 0-021 CST periodically for microindentation and Raman spectroscopy, respectively. Live cell imaging of the slice cultures will be done in 422 Bowne Hall. Some tissue samples will be fixed with 4% paraformaldehyde immediately following saline perfusion and used for histological analysis. All animal carcasses will be collected, bagged, and frozen in 0-021 CST until materials are removed by EHO for disposal. Extracted tissue samples will be frozen after use and kept in 422 Bowne Hall until materials are removed by EHO for disposal. PhD student Kyle Bishop will be primarily responsible for all procedure in study 2. He will be assisted by Dr. Hasenwinkel, Dr. Chaiken, and PhD student Alex Janini.

9.c) If you have indicated Category D in section 8. 5) (Refinement), describe how and when you will monitor the animals' condition. Describe how and when analgesics will be given (with dosages) and how analgesic effectiveness will be monitored. If you have indicated Category E in section 8. 5) (Refinement), provide a scientific explanation for why the use of anesthetic, analgesic, or tranquilizing drugs to relieve pain or distress would adversely affect the procedures, results, or interpretations.

Study 1 - Post-operative buprenorphine (0.5 mg/kg, subcutaneous) will be administered twice daily for two days. Animals will be monitored by the lab daily for 3 days post-operatively to determine whether or not there is return to normal behavior (i.e. eating, drinking, activity). Surgical incision sites will also be observed during this time frame for clinical signs of infection or suture breakdown, including abnormal swelling, redness, and exudate from the wound. In case of any infection, animal care staff will be notified immediately. With this type of injury, bowel and/or bladder shock is uncommon but a low roughage diet will be fed to these animals for the week prior to and post surgery as an additional precaution as well as urine will be expressed twice daily if necessary. Autophagia may also occur infrequently. If this is a problem, animals will be coned to decrease access to the caudal part of the body.
After the first 3 days, lab personnel will perform exams every 2 days for the remainder of the survival time. Animals will be monitored for behavioral signs of pain or distress including weight loss, absence of movement, and guarding of the injury site. Animals exhibiting these signs will be attended to and given pain relief or euthanized with the guidance of animal care staff or consultation with the attending veterinarian.

Study 2 solely involves non-survival procedures, therefore, no post-operative monitoring or administration of analgesics is necessary.

The data cannot be obtained using a non-animal alternative since the basic objective of the study is to characterize rat spinal cord tissue. We have proposed a pilot study to confirm the reproducibility of our injury model, which will limit the number of animals needed for other experimental groups to 5.

Methods and sources used to determine that alternatives were not available:

a) Database searched: Pubmed
b) Date of search: February 1, 2016
c) Years covered by search: 2006-2016
d) Key words used: spinal cord raman spectroscopy, in vivo raman spectroscopy, microindentation spinal cord, live cell tracking spinal cord, glial scar mechanical properties, organotypic slice cultures spinal cord

10.CONSIDERATION OF DUPLICATION

Federal law requires a written narrative describing the steps taken to determine that the proposed work does not unnecessarily duplicate previous experiments. If what is proposed does attempt to duplicate previous research, explain why (such as for teaching, to provide more normative data to better test an hypothesis, to train others in new methods, etc.). If what is proposed does not duplicate previous research, specifically cite the databases searched, the dates covered, the key words and/or search strategy used, the colleagues consulted, and any other documentation as proof.

The pilot study proposed in this protocol does attempt to duplicate previous research for training purposes. PI Hasenwinkel and other personnel Bishop and Janini will be trained on the research methods associated with using the MASCIS impactor to create spinal contusion injury at a three-day workshop at Rutgers University March 7-9, 2016. This is a well established method that is used in over 100 laboratories in the U.S. After this training, the pilot study will be conducted to ensure that we are able to produce consistent and reliable spinal contusion injuries (mild and moderate) with the MASCIS impactor in our hands. No other animal work will proceed until the completion of the pilot study and none of the other proposed work is duplicative, based on the database searches described in part 9.

11.RISKS TO PERSONNEL

What are the potential animal-related hazards to people entering or working in your laboratory or teaching facility? What efforts will be made to minimize or eliminate the risk to these people? Examples of issues to be dealt with include containment/removal of allergens and pathogens, and use of temporary/permanent areas.

Care will be taken in order to minimize contact between biological materials generated from this research and people working in the laboratory. Animals will be handled in a portion 0-021 CST which has restricted access and minimal traffic. All personnel will wear lab coats while handling animals. Gloves and masks will be worn during surgery, reducing risks to those with allergies. Asceptic procedures will be in place during surgery. All sharps (needles, scalpel blades, etc.) will be handled carefully and disposed of properly in sharps containers. All laboratory equipment used for testing will be throroughly disinfected with bleach solution following contact with animal tissue.

12. ADMINISTRATIVE AND REGULATORY INFORMATION: This information is needed either for IACUC review or for LAR planning.

A.Number of animals: Please complete the following table giving the numbers of animals that are proposed for use by year of anticipated use and b species.

	Species 1	Species 2	Species 3
Common name of species	Rat		
Number for Year 1	40		
Number for Year 2			
Number for Year 3			
Total for this Project	40		
Number for Year 4			
Number for Year 5			
Total for completion	40		

B. Animal use and care.

Breed or strain	Sprague-Dawley		
Name of supplier	Charles River Laboratories Inc.		
Special purchase Requirements	N/A		
Weight range (at time of acquisition or use with units	225-250 g		
Age range (at time of acquisition or use with units	70-84 days		
Sex	Female		
Estimated maximum number to be housed at one time	10		
Estimate of average time to be kept	Study 1- 5 weeks Study 2- 1 week		

C. Animal use and care: SU policy requires that all mammals and birds be housed in LAR facilities unless a special exemption is granted by the IACUC. Amphibians, reptiles and fish may be housed in laboratories. Use 'NA' when a question is not applicable.

Species	Rat		
Where housed? (ISR, BRL, Other)	LSC Vivarium		
Mammalian - normal LAR care, food and water?	Low roughage diet for the week prior to and post surgery		
Non-mammalian - Who will be in charge of normal care, food and water?			
Non-mammalian - Who will be in charge of emergency and holiday care?			
Surgery - where? (ISR, BRL, other: include room number)	0-012 CST, LAR		
Other procedures? (ISR, BRL, other: include room number)	422C Bowne, 403 Bowne		
Place of euthanasia	0-012 CST		
Method of euthanasia	IP overdose of sodium pentobarbitol plus vascular perfusion with saline		
AVMA approved?	Yes		

D. Special maintenance:

Do any of the following housing/maintenance conditions apply **during normal care or during an experiment**? If "yes", explain conditions and indicate for which species.

a) Nonstandard animal room conditions (lighting, temperature, humidity)? Yes/No **NO**

b) Nonstandard animal cages? Yes/No **NO**

c) Nonstandard animal care routines (methods or schedules of cage cleaning, feeding or watering, unusual bedding)? Yes/No **NO**

d) Special breeding? Yes/No **NO** If yes, on what scale, for what purposes and by whom?

13. Faculty/PI Assurance Statement:

I acknowledge responsibility for this project.

I agree to comply with federal and state laws and regulations and with Syracuse University policies applicable to this project. I have read and have a copy of the current Syracuse University Animal Care and Use Policy (Revision issued May 1994).

I have read and have a copy of the Syracuse University Handbook "The Role and Responsibilities of those using Animals in Research and Teaching". I have read the LAR Manual with the included Standard Operating Procedures (SOPs), which is readily available to all persons working on the project.

As Project Director, I will assume responsibility for assuring that all personnel working on the project at any time have participated in the LAR-IACUC mandatory Introductory Training Session and will ensure that all personnel are trained by myself or LAR staff in all procedures needed for the project, or have had equivalent training elsewhere. I will further ensure that all personnel are fully apprised of the SU SOP's in the Manual and all procedures needed to ensure their safety and those of the animals, including procedures to be followed in emergencies.

I am aware that this protocol:
a) if approved, has to be renewed annually.
b) has a time limit of three (3) years and thereafter cannot be renewed without full resubmission though I might have research funding for a longer period of time.
c) covers only personnel for whom training documentation has been submitted. Additional personnel joining the project at any time must have training documentation submitted before they can work with animals.
d) covers only procedures described in this document. Changes in any aspect of the care and use of animals may be made by submitting a "Request for an Amendment" form to the IACUC, and approval must be obtained.

I certify that the statements made on this form are true and complete to the best of my knowledge.

Signature of Project Director

Date:

Signature of Co-PI

(if above person is not a faculty member)
Date:

In order to expedite the processing of this application, it might be helpful to you and the committee if the Principle Investigator attends the IACUC meeting at which this protocol is discussed. Would you like us to contact you with the date and location of the meeting so you can attend while your protocol is being discussed? Yes/No Yes

APPENDIX 1: Special procedures: Given the importance attached to the humane care and treatment of animals, all the following questions must be answered Yes/No.

Species:	1	2	3
a) Prolonged restraint of conscious animals (more than three hours?)	No		
b) Prolonged deprivation of food and/or water (more than 12 hours other than for preoperative fasting?)	No		
c) Potentially painful or stressful procedures performed without anesthetic?	No		
d) More than one survival surgical procedure on the same animal multi le surgeries ?	No		
e) Administration of paralytic agents or muscle relaxants?	No		
f) Unalleviated post-procedural pain, distress or functional deficit?	Yes		
g) Administration of complete Freund's adjuvant? (SU policy requires that other adjuvants be used rather than Freund's. (Explain below why an exemption should be granted.)	No		
h) Injection into footpad or tail base?	No		
i) Repeated bleeding for antibodies? (Explain regime below.)	No		
j) Mammals to be kept in the laboratory (outside LAR facilities) for more than 12 hours?	No		

For any items marked "yes" above, provide a clear justification on scientific grounds.
Study 1 (Pilot) - Animals are expected to have a functional deficit (locomotor) following spinal contusion injury. This study is designed to verify the reliability of the injury model in our hands. Some spontaneous recovery of locomotor defecits is expected during the postoperative period. This procedure is necessary in order to study changes in spinal cord tissue following injury.

APPENDIX 2: Surgery or blood collection.

Species	Sprague-Dawley rats		
List all pre anesthetics with dosages	None		
List all anesthetics with dosages	Pilot study: Ketamine (80 mg/kg) and Xylazine (10 mg/kg) Other studies Urethane, 1000 mg/kg, IP		
List all tranquilizers with dosages	None		
List all postoperative analgesic to be administers with dosages.	Pilot study: Buprenorphine, 0.5 mg/ kg, SC, twice daily for 2 days		

Surgical methods: Describe the step-by-step methods for surgery. For blood collection, give the volume and frequency.

Study 1-Pilot: Female Sprague-Dawley rats will be ordered from Charles River Laboratories Inc. and housed in the animal facility for rats in the LSC vivarium. Female rats at an approximate age of 77 days will be used to be consistent with other experiments previously performed in our laboratory using a spinal cord injury model. The animals will be housed in shoebox cages (3 per cage) for a minimum of seven days to allow for acclimation. At the time of an experiment, a single animal will be transported live from the vivarium in LSC to room 0-021 CST in an appropriate carrier or alternatively, the MACSIS impactor will be moved to the LAR surgery suite and the procedure will be perforomed there. The rat will be initially anesthetized with Ketamine and Xylazine (80 mg/kg and 10 mg/kg, respectively, prepared by the Hasenwinkel lab) and the body temperature will be maintained using a temperature controlled heating pad. Surgery will use aseptic technique. Surgical mask, sterile gloves, and autoclaved instruments will be used during surgery. The skin over the upper thoracic area will be shaved and cleaned with a Betadyne solution. The skin will be incised, and then the connective and muscle tissue will be bluntly dissected to expose T9. A T9 laminectomy will be completed, taking care not to damage the spinal cord during the dorsal lamina removal. The rat will be positioned on the MASCIS impactor and either a mild or moderate injury will be created by dropping a 10 gram rod onto the exposed cord from a height of 12.5 or 25.0 mm, respectively. The MASCIS impactor also measures movement of the spinal column at the impact site, displays the trajectory of the falling rod, and measures the impact velocity (ImpV), cord compression distance (Cd), cord compression time (Ct), and cord compression rate (Cr). These impact parameters correlate with each other and spinal cord lesion volumes (estimated from tissue Na and K concentrations) and locomotor recovery (BBB scores). Homeostasis will be achieved by apposing Gelfoam pellets soaked in a dilute thrombin solution at the lesion site, which will then be removed before closing the lesion in layers with individual sutures. All control animals will receive a laminectomy but no contusion will be performed on control animals.

After surgery, the rats will be kept warm with the aid of a heating bulb and checked every 15 minutes until muscle tone and righting reflexes have recovered. After recovering from the anesthetic, rats will be returned to the LSC vivarium and housed separately until sutures are removed (1 week) and then 3 per

cage. Post-operative buprenorphine (0.5 mg/kg, subcutaneous) will be administered twice daily for two days. Animals will be monitored by the lab daily for 3 days post-operatively to determine whether or not there is return to normal behavior (i.e. eating, drinking, activity). Surgical incision sites will also be observed during this time frame for clinical signs of infection or suture breakdown, including abnormal swelling, redness, and exudate from the wound. In case of any infection, animal care staff will be notified immediately. With this type of injury, bowel and/or bladder shock is uncommon but a low roughage diet will be fed to these animals for the week prior to and post surgery as an additional precaution as well as urine will be expressed twice daily if necessary. Autophagia may also occur infrequently. If this is a problem, animals will be coned to decrease access to the caudal part of the body.

After the first 3 days, lab personnel will perform exams every 2 days for the remainder of the survival time. Animals will be monitored for behavioral signs of pain or distress including weight loss, absence of movement, and guarding of the injury site. Animals exhibiting these signs will be attended to and given pain relief or euthanized with the guidance of animal care staff or consultation with the attending veterinarian.

Locomotor behavior of rats will be observed and quantified using the well-established BBB scoring system every 4 days. Four weeks after surgery, the rat will be euthanized with an intraperitonial overdose of sodium pentobarbital (Fatal Plus, 390 mg/ml; 0.5 cc) and sacrificed when deeply anesthetized by vascular perfusion of saline (550-600 ml) followed by 4% paraformaldehyde for histology. Deep and terminal anesthesia will be indicated by the lack of reflexes at the top inch of the tail or hindlimb and slow or arrested respiration. Paraformaldehyde waste will be collected and stored in a laboratory SSA in compliance with the SU Hazardous Waste Program. Other waste from the perfusion process will be disposed of in the sink with appropriate dilution through rinsing. Tissue segments will be immediately frozen for immunohistochemistry. All animal carcasses will be collected, bagged, and frozen in 0-021 CST until materials are removed by EHO for disposal. PhD student Kyle Bishop will be primarily responsible for all procedures in the pilot study. He will be assisted by Dr. Chaiken, Dr. Hasenwinkel and PhD student Alex Janini.

Study 2 - In vivo Raman spectroscopy and ex vivo characterization of harvested tissue: Female Sprague-Dawley rats will be ordered from Charles River Laboratories Inc. and housed in the animal facility for rats in the LSC vivarium. Female rats at an approximate age of 77 days will be used to be consistent with other experiments previously performed in our laboratory using a spinal cord injury model. The animals will be housed in shoebox cages for a minimum of seven days to allow for acclimation. At the time of an experiment, a single animal will be transported live from the vivarium in LSC to room 0-021 CST in an appropriate carrier. The rat will be anesthetized with Urethane (1000 mg/kg IP) which is an appropriate anesthetic for long term (5 hr) non-survival procedures. Body temperature will be maintained using a heating pad and blood pressure will be monitored over the course of the procedure using a pressure monitor developed by co-PI Chaiken. Surgery will use aseptic technique. The skin over the upper thoracic area will be shaved and cleaned with a Betadyne solution. The skin will be incised, and then the connective and muscle tissue will be bluntly dissected to expose T9. A T9 laminectomy will be completed, taking care not to damage the spinal cord during the dorsal lamina removal. For the SCI groups, the rat will be positioned on the MASCIS impactor and either a mild or moderate injury will be created by dropping a 10 gram rod onto the exposed cord from a height of 12.5, 25.0 mm, or 50 mm, respectively. Raman spectra will be acquired for all animals in the injury groups periodically for 5 hrs to measure biochemical changes in the spinal cord tissue in the acute phase of the injury. Two control

groups will be used and both will receive a laminectomy but no contusion injury. One control group will receive exposure of the spinal cord for 5 hr following laminectomy with no Raman spectroscopy. The other control group will be tested with Raman spectroscopy periodically for 5 hrs . All animals in this study will undergo non-survival procedures. At the conclusion of the 5 hr period of data collection, animals will be euthanized with an intraperitoneal overdose of sodium pentoparbital (Fatal Plus, 390 mg/ml; 0.5 cc) and sacrificed while deeply anesthetized by vascular perfusion of saline (550-600 ml). Deep and terminal anesthesia will be indicated by the lack of reflexes at the top inch of the tail or hindlimb and slow or arrested respiration. Waste from the perfusion process will be disposed of in the sink with appropriate dilution through rinsing. Un-fixed tissue will be extracted and sliced in the transverse plane into 400 micron thick slices for organotypic culture using a tissue chopper. Cultures will be transferred to 422 Bowne Hall in sealed containers and maintained in an incubator. Specimens will be transported in the same manner to 403 Bowne Hall and to 0-021 CST periodically for microindentation and Raman spectroscopy, respectively. Live cell imaging of the slice cultures will be done in 422 Bowne Hall. Some tissue samples will be fixed with 4% paraformaldehyde immediately following saline perfusion and used for histological analysis. All animal carcasses will be collected, bagged, and frozen in 0-021 CST until materials are removed by EHO for disposal. Extracted tissue samples will be frozen after use and kept in 422 Bowne Hall until materials are removed by EHO for disposal.

Postoperative care: Describe arrangements for after-hours, weekend and holiday postoperative care of animals (care above and beyond basic services such as feeding and watering). Will it be by LAR staff, PI, or other personnel? Include information on:

1) Who will observe the animals? LAR and lab personnel (PI, CO-PI, graduate students)
2) How will body temperature be regulated and vital signs monitored? see above
3) Where will the animals be kept until returned to their cages? 0-021 CST
4) Who will be responsible for making sure the animals are returned to their cages? Lab personnel

APPENDIX 3: Hazardous agents:

a)	Radioactive materials. What materials? N/A

b)	Infectious agents. What agents? N/A

c)	Known carcinogens or toxic chemicals. What chemicals? N/A

References

1. Lamotte. Turbidity. http://www.lamotte.com/en/blog/test-factors/91-what-is-turbidity. Web accessed 6/1/18.
2. Harris, D. C. Quantitative Chemical Analysis. New York: W. H. Freeman and Company, 2007. 7th ed. Figure 0-3 pp.4.
3. Barman, I., Sing, G.P., Dasara, R., Feld, M. "Turbidity-Corrected Raman Spectroscopy for Blood Analyte Detection". Anal. Chem. 2009. 81(11): 4233-4240.
4. Steponavicius, R., Thennadil, S.N. ''Extraction of Chemical Information of Suspensions Using Radiative Transfer Theory to Remove Multiple Scattering Effects: Application to a Model Multicomponent System''. Anal. Chem. 2011. 83(6): 1931-1937.
5. Richards-Kortum, R., Sevick-Muraca. E., ''Quantitative Optical Spectroscopy for Tissue Diagnosis''. Annu. Rev. Phys. Chem. 1996. 47: 555-606.
6. Matousek, P., Morris, M.D., Everall, N., Clark, I.P., Towrie, M., Draper, E., Goodship, A., Parker. A.W. ''Numerical Simulations of Subsurface Probing in Diffusely Scattering Media Using Spatially Offset Raman Spectroscopy''. Appl. Spectrosc. 2005. 59(12): 1485-1492.
7. Chaiken, J. Finney, W. F., Peterson, C.M., Peterson, K.P., Knudson, P.E., Weinstock, R. S., Lein, P. "Noninvasive in vivo, tissue modulated near infrared vibration spectroscopy study of mobile and static tissues: blood chemistry". Proc. SPIE 3918 (2000) doi: 1605-7422/00 pp. 135-143.
8. Chaiken, J., Deng, B., Bussjager, R.J., Shaheen, G., Rice, D., Stehlik, D., Fayos. J. "Instrument for Near-Infrared Emission Spectroscopic Probing of Human Fingertips In Vivo". Rev. Sci. Instrum. 2010. 81(3): 034301.
9. Chaiken, J., Goodisman. J. ''On Probing Human Fingertips In Vivo Using Near-Infrared Light: Model Calculations''. J. Biomed. Opt. 2010. 15(3): 037007.
10. Deng, B. , Kastner, E., Narsipur, S.S. , Goodisman, J. , Chaiken J., "Continuous Noninvasive In Vivo Monitoring of Intravascular Plasma Volume and Hematocrit Changes During Hemodialysis in Humans: Direct Comparison with the CRIT-LINE," Proc. SPIE.. 8935: 89351N (2014)
11. Dent, P., Deng, B., Goodisman, J., Chaiken. J. "Coupled turbidity and spectroscopy problems: a simple algorithm for volumetric analysis of optically thin or dilute 2-phase
12. Soubeyrand, Marc, Badner. Anna, Vawda, Reaz, Chung, Yun Sung, Fehlings, Michael G., "Very High Resolution Ultrasound Imaging for Real-Time Quantitative Visualization of Vascular Disruption after Spinal Cord Injury," J. Neurotrauma, 31,1767–1775 (2014)
13. Lynne P. Heighton, Merle Zimmerman, Clifford P. Rice, Eton E. Codling, John A. Tossell, Walter F. Schmidt, "Quantification of Inositol Hexa-Kis Phosphate in Environmental Samples", Open Journal of Soil Science, 2012, 2, 55-63 doi:10.4236/ojss.2012.21009
14. Pegg, D. E., "Viability assays for preserved cells, tissues, and organs". 1989, Cryobio. 26(3). 212-231
15. Daley, M. E., Spyracopoulos, L., Jia, Z., Davies, P. L., Sykes, B. D. "Structure and Dynamics of a β-Helical Anitfreeze Protein" Biochemistry, 2002, 41(17). 5515-5525.
16. "Overview of Probes for Cell Viability, Cell Proliferation and Live-Cell Function—Section 15.1". Invitrogen. Life Technologies. 2010

17. U.S. Department of Health and Human Services. “Biologics License Applications for Minimally Manipulated, Unrealted Allogeneic Placental/Umbilical Cord Blood Intended for Hematopoietic and Immunologic Reconstitution in Patients with Disorders Affecting the Hematopoietic System”. *Guidance for Industry*. Food and Drug Administration. Center for Biologics Evaluation and Research. 2014.
18. U. S. Department of Health and Human Services. “Minimally Manipulated, Unrelated Allogeneic Placental/Umbilical Cord Blood Intended for Hematopoietic Reconstitution for Specified Indication” *Guidance for Industry.* Food and Drug Administration. Center for Biologics Evaluation and Research. 2009.
19. De Pablo, F., Ferrus, A., Stern, C. D., Ed. *Cellular and Molecular Procedures in Developmental Biology.* Academic Press. San Diego. 1998.
20. Chaiken, J., Dracker, R., Hagrman, P., Hagrman, D., “Process For Determination of Cell Viability”. European Patent EP 699 351 B1. IssuedAugust 13, 2006.
21. R. T. McDonough, Steven Ortiz, Paul Dent, Jerry Goodisman, J. Chaiken, “Coupled Turbidity and Spectroscopy Problems: A Simple Algorithm for Volumetric Analysis of Optically Thin or Dilute in vitro Bacterial Cultures in Various Media" Submitted Appl. Spectroscopy, Peer reviewed “acceptable”, pending Editorial revision 4-22-2019.
22. Song, Y,. Wang, S., Chan, M., Chandra, B., Dhawan,. Song, Y., “Femoral fracture risk assessment after intensity modulated radiation therapy (IMRT) for the treatment of soft tissue sarcoma using a novel mathematical model. Conf Proc IEEE Eng Med BiolSoc 2006. 1. 95-98
23. Small Jr, W., Kachnic, L,. “Postradiotherapypelic fractures: cause for concern or opportunity for future research?” JAMA 2005. 294. 2635-2637
24. Park, S. H., Kim, J. C., Lee, J. E., Park, I. K., “Pelvic insufficiency fracture after radiotherapy in patients with cervical cancer in the era of PET/CT. RadiatOncol J 2011. 29. 269-276j.
25. Kelly, J., Damron, T., Grant, W., Anker, C., Holdridge, S., Shaw, S. et al. “Cross-sectional study of bone mineral density in adult survivors of solid pediatric cancers”. J. Pediatr. Hematol. Oncol. 2005. 27. 248-253.
26. Dieckmann, K. P., Pichlmeier, U., “Is risk of testicular cancer related to body size?” Eur. Urol. 2002. 42. 564-569.
27. Helmstedter, C. S., Goebel, M., Zlotecki, R., Scarborough, M. T. “Pathologic fractures after surgery and radiation for soft tissue tumors.” Clin. Orthop. Relat. Res. 2001. 165-172.
28. Lin, P. P. Schupak, K. D., Boland, P. J., Brennan, M. F., Healey, J. H., “Pathologic femoral fracture after periosteal excision and radiation for the treatment of soft tissue sarchoma.” Cancer. 1998. 82. 2356-2365.
29. Bandstra, E. R., Thompson, R. W., Nelson, G. A., Willey, J. S., Judex, S., Cairns, M. A., et al. “Musculoskeletal changes in mice from 20-50 cGy of simulated galactic cosmic rays.” Radiat. Res. 2009. 172. 21-29.
30. Kondo, H., Searby, N. D., Mojarrab, R., Phillips, J., Alwood, J., Yumoto, K., et al. “Total-body irradiation of postpubertal mice with (137)Cs acutely compromises the microarchitecture of cancellous bone and increase osteoclasts.” Radiat. Res. 2009. 171. 283-289.

31. Wernle, J. D., Damron, T. A., Allen, M. J., Mann, K. A., “Local irradiation alters bone morphology and increases bone fragility in a mouse model”. J. Biomech. 2010. 43, 2738-2746.
32. Dhakal, S., Chen, J., McCance, S., Rosier, R., O’Keefe, R., Constine, L. S., “Bone density changes after radiation for extremity sarcomas: exploring the etiology of pathologic fractures.” Int. J. Radiat. Oncol. Biol. Phys. 2011. 80. 1158-2263.
33. Morris, M., Mandair, G. S., “Raman Assessment of Bone Quality”. Clin Ortho Relat Res. (2011) 469:2160-2169.
34. Raghavan, M., Sahar, N. D., Wilson, R. H., Mycek, M., Pleshko, N., Kohn, D. H., Morris, M. D., “Quantitative polarized Raman spectroscopy in highly turbid bone tissue”. J. Bio Optics. 2010. 15(3) 037001.
35. Kazanci, M., Roschger, P., Paschalis, E. P., Klaushofer, K., Fratzl, P., “Bone osteonal tissues by Raman specral mapping: Orientation-composition”. J. Struc. Bio. 2006, 156. 489-496.
36. Kazanci, M., Wagner, H. D., Manjubala, N. I., Gupta, H. S., Paschalis, E., Roschger, P., Fratzl, P., “Raman imaging of two orthogonal planes with cortical bone”. Bone, 2007, 41. 456-461.
37. Okagbare, P. I., Esmonde-White, F. W. L., Goldstein, S. A., Morris, M. D., “Development of non-invasive Raman spectroscopy for *in vivo* evaluation of bone graft osseointegration in a rat model”, Analyst, 2010, 135, 3142-3146.
38. Schulmerich, M. V., Cole, J. H., Dooley, K. A., Morris, M. D., Kreider, J. M., Goldstein, S. A., Srinivasan, S., Pogue, B.W., ‘Noninvasive Raman tomographic imaging of canine bone tissue”, JBO Letters. 2008. 13(2) 020506.
39. Gong, B., Oest, M. E., Mann, K. A., Damron, T. A., Morris, M. D., “Raman spectroscopy demonstrates prolonged alteration of bone chemical composition following extremity localized irradiation”. Bone. 2013 57, 252-258.
40. Penel, G., Delfosse, C., Descamps, M., Leroy, G., “Composition of bone and apatitic biomaterials as revealed by intravital Raman microscopy”. *Bone.* 2005. 36. 893-901.
41. Chaiken, J., Deng, B., Goodisman, J., Shaheen, G., Bussjager, R. J. “Analyzing near infrared scattering from human skin to monitor changes in hematocrit”. Proc. SPIE. 2012 821908.
42. National Spinal Cord Injury Statistical Center, “Spinal cord injury facts and figures at a glance” (Birmingham, Alabama,2010), https://www.nscisc.uab.edu/public_content/pdf/Facts%20and%20Figures%20at%20a%20Glance%202010.pdf.
43. T. Saxena, B. Deng, D. Stelzner, J. Hasenwinkel, J. Chaiken. “Raman spectroscopic investigation of spinal cord injury in a rat model”. J. Biol. Opt., 2011. 16(2), 027003
44. Mautes, Angelika, Weinzierl, Martin R., Donovan, Frances, Noble, Linda J. “Vascular Events After Spinal Cord Injury: Contribution to Secondary Pathogenesis.” Physical Therapy, 80(7), 573(2000)
45. Paul Dent, Sai Han Tun, Seth Fillioe, Bin Deng, Josh Satalin, Gary Nieman, Kailyn Wilcox, Quinn Searles, Sri Narsipur, Charles M. Peterson, Jerry Goodisman, James Mostrom, Richard Steinmann, J. Chaiken, "Simultaneous, noninvasive, in vivo, continuous monitoring of hematocrit, vascular volume, hemoglobin oxygen saturation, pulse rate and breathing rate in humans and other animal models using a single light

source," Proc. SPIE **10484**, Advanced Biomedical and Clinical Diagnostic and Surgical Guidance Systems XVI, 1048410 (12 February 2018); doi: 10.1117/12.2290231
46. Hugang Ren, "Cystoscopic Optical Coherence Tomography and Ultrahigh Resolution Optical Doppler Tomography for Quantitative Structural and Functional Imaging," Thesis, Doctor of Philosophy, Biomedical Engineering, Stony Brook University, August 2012
47. Ali Shuaib, Ali K. Bourisly, "Photobiomodulation Optimization for Spinal Cord Injury Rat Phantom Model", Translational Neuroscience **9**, pp 67-71(2018) DOI: 10.1515/tnsci-2018-0012
48. Ji-Wei He , Hanli Liu, and Yuan Bo Peng, "Hemodynamic and Light-Scattering Changes of Rat Spinal Cord and Primary Somatosensory Cortex in Response to Innocuous and Noxious Stimuli," *Brain Sci.* **5**, 400-418(2015); doi:10.3390/brainsci5040400
49. Deng, B. Wright, C. Lewis-Clark, E. Shaheen, G. Geier, R. Chaiken, J. "Direct noninvasive observation of near-infrared photobleaching of autofluorescence in human volar side fingertips *in vivo*," *Proc. SPIE* **7560**, 75600P (2010)
50. Deng, B., Simental, Anabel, Lutz, Patrick, Shaheen, George, and Chaiken, Joseph, "Singlet Oxygen Induced Advanced Glycation End-product Photobleaching of In Vivo Human Fingertip Autofluorescence", Proc. SPIE **8219**, 82190D (2012)
51. Public Domain, https://en.wikipedia.org/w/index.php?curid=8138748
52. Hellwig S, Heinrich A, Biber K. The brain's best friend: microglial neurotoxicity revisited. Front Cell Neurosci. 2013;7(May):1-11. doi:10.3389/fncel.2013.00071.
53. Ellingson BM, Salamon N, Holly LT. Imaging techniques in spinal cord injury. World Neurosurg. 2014;82(6):1351-1358. doi:10.1016/j.wneu.2012.12.004.
54. Ducker TB, Salcman M, Perot PL, Ballantine D. Experimental spinal cord trauma, I: Correlation of blood flow, tissue oxygen and neurologic status in the dog. Surg Neurol. 1978;10(1):60-63. http://www.ncbi.nlm.nih.gov/pubmed/684608.
55. Rivlin AS. Regional spinal cord blood flow in rats after severe cord trauma. J Neurosurg. 1978;49(6):844-853. doi:10.3171/jns.1978.49.6.0844.
56. Ito T, Oyanagi K, Wakabayashi K, Ikuta F. Traumatic spinal cord injury: a neuropathological study on the longitudinal spreading of the lesions. Acta Neuropathol. 1997;93(1):13-18.
57. Dvorak MF, Noonan VK, Fallah N, et al. The Influence of Time from Injury to Surgery on Motor Recovery and Length of Hospital Stay in Acute Traumatic Spinal Cord Injury: An Observational Canadian Cohort Study. J Neurotrauma. 2015;32(9):645-654. doi:10.1089/neu.2014.3632.
58. Mautes, Angelika, Weinzierl, Martin R., Donovan, Frances, Noble, Linda J. "Vascular Events After Spinal Cord Injury: Contribution to Secondary Pathogenesis." Physical Therapy, 80(7), 573(2000)
59. Young W. Spinal cord contusion models. ProgBrain Res. 2002;137(0079-6123 (Print)):231-255.
60. Ruberto, S. Master Thesis, Syracuse University, 2013, 56.
61. Frantz JD. Raman spectra of potassium carbonate and bicarbonate aqueous fluids at elevated temperatures and pressures: Comparison with theoretical simulations. Chem Geol. 1998;152(3-4):211-225. doi:10.1016/S0009-2541(98)00058-8.

62. Di Terlizzi R, Platt S. The function, composition and analysis of cerebrospinal fluid in companion animals: Part I - Function and composition. Vet J. 2006;172(3):422-431. doi:10.1016/j.tvjl.2005.07.021.
63. Bo K. Siesjö, "The regulation of cerebrospinal fluid pH", Kidney International, 1, 360-374(1972).
64. Barry G. Oliver, Anthony E. Davis, "Vibrational Spectroscopic Studies of Aqueous Alkali Metal Bicarbonate and Carbonate Solution" Can. J. Chem. 51, 698-702(1973)
65. Chaiken, et al "Effect of hemoglobin concentration variation on the accuracy and precision of glucose analysis using tissue modulated, noninvasive, in vivo Raman spectroscopy of human blood: a small clinical study" Journal of Biomedical Optics 10(3), 031111 (May/June 2005)
66. Harris, D. C. Quantitative Chemical Analysis. New York: W. H. Freeman and Company, 2007. 7th ed. Appendix G Acid Dissociation Table. Pp AP18.
67. UltraScan LIMS Portal "pH table for Potassium and Sodium Phosphate Buffers" http://www.uslims.aucsolutions.com/po4buffers.php
68. D.B. Rorabacher, "Statistical Treatment for Rejection of Deviant Values: Critical Values of Dixon's "Q" Parameter and Related Subrange Ratios at the 95% Confidence Level"Anal. Chem. 63 (1991) 139
69. Kaiser, Gernot, M and Frühauf, Nils R. "Method of intracranial pressure monitoring and cerebrospinal fluid sampling in swine." Laboratory Animals. (2007) **41**, 80-85
70. Park Y, Luo T, Zhang F, et al. Downregulation of Src-kinase and glutamate-receptor phosphorylation after traumatic brain injury. J Cereb Blood Flow Metab. 2013;33(10):1642-1649. doi:10.1038/jcbfm.2013.121.
71. Tu, A. T., Raman Spectroscopy In Biology: Principles and applications, John Wiley & Sons: New York, 1982.
72. Brewster, V. L., Ashton, L., Goodacre, R. "Monitoring the Glocsylation Status of Proteins Using Raman Spectroscopy." Anal. Chem., 2011. 83(15) 6074-6081.
73. Siamwiza, M. N., Lord, R. C., Chen, M. C., "Interpretation of the Doublet at 850 and 830 cm-1 in the Raman Spectra of Tyrosyl Residues in Proteins and Certain Model Compounds" Biochemistry. 1975. 14(22). 4870-4876.
74. Riedel, H., Massoglia, S., Schlessinger, J., Ullrich, A., "Ligand activation of overexpressed epidermal growth factor receptors transforms NIH 3T3 mouse fibroblasts" Proc. Natl. Acad. Sci. USA. 1988. 85 1477-1481.
75. Abdi, H., Williams, L.J. "Principal Component Analysis". Wiley Interdisciplinary Reviews: Computational Statistics. 2010. 2(4). 433-459.
76. Romano, P., Manniello, A., et. al. "The Cell Line Database" http://bioinformatics.hsanmartino.it/cldb/cl3711.html Date Accessed: 11/23/16.
77. Chaiken, J., Finney, W. F., Knudson P.E., Peterson, K., Peterson, C. M., Bussjager, R. J., Zhao, Y., Weinstock, R. S., Khan, M, Hagrman D., Hagrman, P., "The effect of hemoglobin concentration variation on the accuracy and precision of glucose analysis using tissue modulated, noninvasive, in vivo Raman spectroscopy of human blood: a small clinical study", J. Biomed. Opt.10, 031111 (2005))

78. Munyon, W., Merchant, D.J., “The relation between glucose utilization, lactic acid production and utilization and the growth cycle of L strain fibroblasts.” Experimental Cell Research 1959. 17, 490-498
79. Virginia PHYS 304. “The Properties of Water” http://galileo.phys.virginia.edu/classes/304/h2o.pdf Date Accessed:12/20/16
80. Tharmalingam, T., Wu, C., Callahan, S., Goudar, C. “A Framework for Real-Time Glycosylation monitoring (RT-GM) in Mammalian Cell Culture”. Biotechnology and Bioengineering. 2015. 112. 1146-1154
81. Thermo Fischer Scientific. “Extra-Cellular Matrices.” https://www.thermofisher.com/us/en/home/life-science/cell-culture/3d-cell-culture.html Date Accessed: 11/20/16
82. Sigma Aldrich. “Pyruvate” https://www.sigmaaldrich.com/catalog/product/sial/p2256?lang=en&region=US
83. DeLucca, A.J., Carter-Wientjes, C., Williams, K.A., Bhatnagar, D., “Blue light (470 nm) effectively inhibits bacterial and fungal growth”. Appl. Micro. 2012. 0266-8254.
84. Lipovsky, A., Nitzan, Y., Gedanken, A., Lubart, R. “Visible Light-Induced Killing of Bacteria as a Function of Wavelength: Implication of Wound Healing.” Lasers in Surgery and Medicine. 2010. 42. 467-472
85. Lubart, R., Lipovski, A., Friedmann, H., “A Possible Mechanism for the Bactericidal Effect of Visible Light”. Laser Therapy. 2010. 20.1 17-22
86. B. Deng, E.Kastner, P. Dent, J. Goodisman, J. Chaiken. “Continuous noninvasive in vivo monitoring of intravascular plasma volume and hematocrit changes in response to blood removal and fluid replacement in a rat model”. Proc. SPIE.2014.8935: 893526
87. Greco, N.J., Seetharaman, S., Kurtz, J., Lee, W. R., Moroff, G., Evaluation of the Reactivity of Apoptosis Markers Before and After Cryopereservation in Cord Blood CD34+ Cells”. Stem Cells and Development. 2006, 15. 124-135
88. Cui, Y., Turner, G., Roy, U. N., Guo, M., Pan, Z., Morgan, S., Burger, A., Yeh, Y., “Raman spectroscopy shows antifreeze glycoproteins interact with highly oriented pyrolytic graphite”. J. Raman Spectroscop., 2005 36, 1113-1117
89. Cannon, C. P., Lin, P. P. Lewis, V. O., Yasko, A. W., Management of radiation-associated fractures. J. Am. Acad. Orthop. Surg. 2008. 16. 541-549.
90. Taremi, M., Hope, A., Lindsay, P., Dahele, M., Fung, S., Purdie, T. G., et al. “Predictors of radiotherapy induced bone injury (RIBI) after stereotactic lung radiotherapy.” Radiat. Oncol. 2012. 7. 159.
91. Gortzak, Y., Lockwood, G. A., Mahendra, A., Wany, Y., Chung, P. W., Catton, C. N., et al. “Prediction of pathologic fracture risk of the femur after combined modality treatment of soft tissue sarcoma of the thigh.” Cancer. 2010. 116. 1553-1559.
92. Coe, B., Kukkapalli, P., Nam, A., “Profiling a Gaussian Laser Beam.” http://laser.physics.sunysb.edu/~annie/miniproject/ Date Accessed: 11/25/16
93. “Structure of a Long Bone” https://en.wikipedia.org/wiki/Metaphysis#/media/File:Structure_of_a_Long_Bone.png Date Accessed: 11/25/16

94. Sathyanarayana, D. N. Vibrational Spectroscopy: Theory and Applications. 1st ed.; New Age International Publishers: New Delhi, 2004; pp 312-313
95. Penel, G., Delfosse, C., Descamps, M., Leroy, G., "Composition of bone and apatitic biomaterials as revealed by intravital Raman microscopy". Bone. 2005. 36. 893-901.
96. Meinke, M., Muller, G., Helfmann, J., Friebel, M. "Optical properties of platelets and blood plasma and their influence of the optical behavior of whole blood in the visible and near infrared wavelength range". J. Biomed. Opt. 2007. 12: 014024.
97. Rozanov, V., Vountas, M. "Radiative transfer equation accounting for rotational Raman scattering and its solution by the discrete-ordinates method." J. Quant. Spec. & Rad. Trans. 133. 2014. 603-618
98. Weston, K., Reynolds, A.C., Alikhan, A., Drago, D.W., "Radiative transfer in highly scattering materials—numerical solution and evaluation of approximate analytic solutions." NASA Technical Reports Server (NTRS). 1974. 01-01.
99. Matousek, P., Morris, M.D., Everall, N., Clark, I. P., Towrie, C. M., Draper, E., Goodship/ A., Parker, A. W., "Numerical Simulation of Subsurface Probing in Diffusely Scattering Media Using Spatially Offset Raman Spectroscopy". Appl. Spec. 2005. 59(12), 1486-1492.
100. Carmona, R., Pritz, J., Bydder, M., Gulaya, S., Zhu, H., Williamson, C.W., Welch, C.S., Vaida, F., Bydder, G., Mell, L.K., "Fat composition changes in bone marrow during chemotherapy and radiotherapy." Int. J. Radiat. Oncol. Biol. Phys. 90(1). 2014. 155-163.
101. Dent, P. PhD. Dissertation, Syracuse University. 2016
102. Tuchin, V. [Tissue Optics], 2nd Edition, SPIE Press, Bellingham, Washington, USA. 2007.
103. Sroga, G., Vashishth, D., "UPLC methodology for identification and quantitation of naturally fluorescent crosslinks in proteins: A study of bone collagen". J Chromatogr B Analyt Technol Biomed Life Sci. 2011. 879 (5-6) 379-385.
104. Naslund, J., Pettersson, J., Lundeberg, T., Linnarsson, D., Lindberg, L., "Non-invasive continuous estimation of blood flow changes in human patellar bone." Med. Bio. Eng. Comput. 2016. 44, 501-509.

VITA

Seth Fillioe
Chaiken Research Group,
Department of Chemistry, Syracuse University,
0-012 Center for Science and Technology
Syracuse, New York 13244
(802)282-2647

Work Experience:

-Research Assistant — August 2018-Present
Syracuse University/Critical Link

-Teaching Assistant
Syracuse University — August 2014-May 2018

-Teaching Assistant
St. John's University — August 2012-May 2014

Research Experience:

-Graduate Research Assistant
Syracuse University — August 2014-Present

-Graduate Research Assistant
St. John's University — August 2012-May 2014

-Undergraduate Research Assistant
Hofstra University — August 2011-May 2012

Teaching Experience:

-As a Teaching Assistant at Syracuse University:
General Chemistry Lab I and II
General Chemistry Recitation I
Honors General Chemistry Recitation II
Chemical and Biochemical Analysis Lab
Forensic Chemical Analysis Lab

-As a Teaching Assistant at St. John's University:
General Chemistry Lab I
Pharmacy General Chemistry Lab I and III
Instrumental Analysis Lab
Analytical Chemistry Lab

Peer reviewed publications:

Seth Fillioe, Kyle K. Bishop, Alexander V. S. Jannini, John J. I. Kim, Ricky McDonough, Steve Ortiz, Jerry Goodisman, Julie Hasenwinkel, Charles M. Peterson, Joseph Chaiken, "In vivo, noncontact, real-time, PV[O]H imaging of the immediate local physiological response to spinal cord injury in a rat model," J. Biomed. Opt. 25(3), 032007 (2019), doi: 10.1117/1.JBO.25.3.032007

Proceedings papers:

Fillioe, S., Bishop, K. K., Jannini, A. V. S., Kim, J., McDonough, R., Ortiz, S., Goodisman, J., Hasenwinkel, J., Chaiken, J. "In vivo, non-contact, real-time, optical and spectroscopic assessment of the immediate local physiological response to spinal cord injury in a rat model" SPIE 10489-10 Feb. 2018.

Dent, P., Tun, S. H., Fillioe, S., Deng, B., Satalin, J., Nieman, G., Wilcox, K., Searles, Q., Narsipur, S., Peterson, C. M., Goodisman, J., Mostrom, J., Steinmann, R., Chaiken, J. "Simultaneous, noninvasive, in, vivo, continuous monitoring of hematocrit, vascular volume, hemoglobin oxygen saturation, pulse rate and breathing rate in humans and other animal models using a single light source". SPIE 10489-34 Feb. 2018.

Seth Fillioe, Kyle Kelly Bishop, Sai Han Tun, Paul Dent, Bin Deng, Charles M. Peterson, Jerry Goodisman, Julie Hasenwinkel, J. Chaiken. "A chemist's view of inflammation in contusion injured spinal cord in a rat model: noninvasive, noncontact, in vivo Raman spectroscopy minutes to hours after injury" SPIE Proc. 10863-16. Feb. 2019,.

Seth Fillioe, Paul Dent, Bin Deng, Sri Narsipur, Charles M. Peterson, Jerry Goodisman, Richard Steinmann, James Mostrom, J. Chaiken. "Direct noninvasive, real-time observation of thermoregulation physiology: periodic fluctuations in hematocrit and vascular volume in the peripheral circulation." SPIE Proc. 10868-2 Feb. 2019.,

Poster Presentations:

Fillioe, S., Ng, C., Huang, L., Wachter-Jurcsak, N. "Examination of Nitroxide Release from Dibenzoyl Furoxans Using a Fluorescent Assay". Poster Presentation at PITTCON 2012.

Deng, B., Fillioe, S., Dent, P., Peterson, C.M., Mostrom, J., Steinmann, R., Satalin, J., Goodisman, J., Nieman, G. F., Narsipur, S., Chaiken, J., "PV[O]H Signals Intravascular Blood Loss in the Rat" OSA April 2018. Poster Presented by J. Chaiken at meeting.

Seth Fillioe, Kyle Kelly Bishop, Alexander Vincent Struck Jannini, Jon Kim, Ricky McDonough, Steve Ortiz, Jerry Goodisman, Julie Hasenwinkel, J. Chaiken,. "Use of PV[O]H algorithm as a noninvasive imaging modality for spinal cord injury in vivo in a rat model" OSA April 2019 poster presented by J. Chaiken at OSA Biomed meeting

Education:

Bachelors of the Arts in Chemistry
Hofstra University August 2008-May 2012

Master of Science in Chemistry
Thesis entitled: "The use of radiative transfer theory, quantitative spectroscopy and physical optics to advance noninvasive monitoring of living systems"
Syracuse University August 2014-May 2017

Doctor of Philosophy in Chemistry
Thesis entitled: Spectroscopy versus turbidity: non-invasive *in vivo* monitoring of living systems"
Syracuse University August 2014-August 2020